

博士論文

Dual Polarization Travelling-Wave Antenna with Centralized
Radio-Frequency Transmitting/Receiving System for Synthetic
Aperture Radar in Small Satellites

(小型衛星搭載の合成開口レーダー用の集中型送受信システムを有する2偏波対応進行波型アンテナ)

ラビンドラ ビネー

Acknowledgements

It has been a great pleasure of mine to work on this dissertation. I thank my Sensei, Prof. Hirobumi Saito for allowing me to be a part of his laboratory and his constant support through my study period. I especially enjoyed numerous, seemingly never-ending discussions we used to have, which made my research more fun. I was also privileged to have support from Prof. Jiro Hirokawa of Tokyo Institute of Technology who lent his vast knowledge and experience in the field of antenna development. I thank Prof. Akira Oyama for introducing me to multi-objective optimization using NSGA-II.

I also had support from many colleagues at my laboratory (Saito Lab) and also from Ando and Hirokawa Lab at Tokyo Institute of Technology. I especially thank Dr. Prilando Akbar, Dr. Miao Zhang, Dr. Makato Sano and Kimio Sakurai for their help in electromagnetic simulations and antenna pattern measurements. Special thanks to Dr. Tomiki Atsushi and Takahiko Tomoda for their support in assembling of microwave cavity power combiner prototype unit. I thank Tomoko Kusadome, Hiromi Watanabe, Taufik Sulaiman and Tomaya Fukami for their support in managing my daily life in Japan. Besides the above people, I have had the opportunity to interact with many other people from whom I obtained new ideas and understanding of my research.

Special thanks to the University of Tokyo, Institute of Space and Astronautical Science/ Japan Aerospace Exploration Agency (ISAS/JAXA), KDDI Foundation and Ministry of Education, Culture, Sports, Science and Technology (MEXT) for providing financial support for my studies. I am also indebted to the Office of International Students (OIS) at University of Tokyo for helping me search for scholarships.

I also thank my family and friends for always encouraging me to pursue my dreams. This dissertation will not be complete without saying thank you to my mother, grandfather and my late grandmother, the most important people, for constant their love and care.

Contents

1	Introduction	9
1.1	Background	9
1.1.1	The MicroXSAR mission	12
1.2	SAR Imaging	12
1.3	Research Objectives and Approach	16
1.4	Outline of Remaining Chapters	17
2	Antenna Systems for Space-Based SAR	20
2.1	Survey of Previous SAR Antenna Systems	21
2.1.1	Antenna Array Architectures	25
2.2	A Passive-Array Centralized RF Feed SAR Antenna System for Small Satellites	28
2.2.1	Selection of Antenna Panel Technology	29
2.2.2	System Architecture	33
2.3	Relationship between Antenna Characteristics and SAR Performance	34
2.3.1	Signal to Noise Ratio of Image (SNR_{image})	34
2.3.2	Artifacts due to Range Ambiguity and Azimuthal Ambiguity .	35
2.4	Summary	39
3	A Traveling Wave Dual Polarimetric Antenna for SAR	40
3.1	A Discrete Linear Array Model for Traveling Wave Antenna	41
3.2	Multi-objective Genetic Algorithm Optimization of Travelling Wave Linear Arrays	47

3.2.1	Discussion on Classical Optimization Techniques used for Design of Antenna Pattern	47
3.2.2	Examples of Metaheuristic Optimization applied to case of Antennas	49
3.2.3	From Single-Objective to Multi-Objective Optimization	50
3.3	Synthesis of Optimal Aperture Field Distribution over an Antenna Panel	54
3.3.1	Mathematical Model of Antenna Panel	54
3.3.2	Optimization Objectives	55
3.3.3	Optimization Constraint and Variables	56
3.3.4	Optimization Parameters	57
3.3.5	Optimization Results	57
3.4	Computer Model and Simulation	61
3.5	Test Results of Fabricated Antenna Panel Prototype	63
3.5.1	Near Field Measurements	64
3.5.2	Far-Field Measurements	70
3.5.3	Voltage Network Analyzer (VNA) Tests	73
3.6	Synthesis of Optimal Excitations of an Array of Antenna Panels	74
3.7	Summary	78
4	Design of Cylindrical Cavity Power Combiner	79
4.1	Background	80
4.1.1	Power requirements	80
4.1.2	High Radio Frequency (RF) Power Sources for Space Applications	81
4.2	Power Combiners Overview	83
4.2.1	General Characteristics of Power Combiners	84
4.2.2	Power Combining Techniques	87
4.2.3	Survey of Microwave Power Combiners	91
4.3	Description of Proposed Structure	96
4.3.1	Selection of Power Combining Technique	96
4.3.2	Cylindrical Cavity	97

4.3.3	Micrsotrip Line Interface to Cavity	100
4.3.4	Substrate Selection	100
4.3.5	Rectangular Waveguide Interface to Cylindrical Cavity	102
4.4	Implementation of the Design	103
4.4.1	Reduced Model Driven Mode Simulation	103
4.4.2	Full Model Driven Mode Simulation	104
4.4.3	Prototype Assembly	106
4.4.4	Simulation versus Measurement Results	108
4.5	Summary	110
5	Conclusion	111
5.1	Summary and Discussion	111
5.2	Suggestions for Future Work	118

List of Figures

1-1	Illustration of RapidEye constellation	10
1-2	Photograph of TerraSAR-X	11
1-3	Imaging geometry of a side-looking radar system	13
1-4	Polarimetric imaging	13
1-5	Crossrange resolution synthesis in SAR.	14
2-1	A passive antenna array.	25
2-2	Architecture of electronically scanned (phased-array) antennas.	27
2-3	Configuration of receiving DBF	28
2-4	Waveguide-fed parallel plate slot array antenna configuration	30
2-5	Radial line slot antenna with honeycomb structure	31
2-6	Structure of parallel plate slot-pair array antenna.	32
2-7	Antenna system architecture	34
2-8	Range-pattern and Cross-range pattern	35
2-9	Example of effect of range ambiguity in Synthetic Aperture Radar (SAR) image.	36
2-10	Geometry of SAR imaging in range direction	37
2-11	Geometry of SAR imaging in cross-range direction	38
3-1	Model of traveling wave antenna with couplers	42
3-2	Linear array of radiators along z-axis	43
3-3	HFSS model of slot-pair	46
3-4	Relative power Pattern of single radiator.	47
3-5	Illustration of Pareto-curve	53

3-6	Array model of antenna	55
3-7	Pareto curves and comparison of results from NSGA-II and Sakakibara	59
3-8	Implemented Pareto solution	61
3-9	HFSS modeling	62
3-10	Photographs of the antenna panel and its components.	63
3-11	Coordinate system of antenna panel tests.	64
3-12	Near field test setup in Tokyo Institute of Technology (TIT)	65
3-13	Near field electric field amplitude and phase distribution at 9.65 GHz	65
3-14	RHCP and LHCP electric field amplitude and phase distribution at 9.65 GHz.	66
3-15	Frequency dependence of antenna directivity (RHCP and LHCP). . .	68
3-16	RHCP and LHCP far-field patterns.	69
3-17	Range ambiguity performance of the antenna.	70
3-18	Far-field antenna test setup	71
3-19	RHCP, LHCP directivity, gain and axial ratio.	72
3-20	VNA test setup	74
3-21	Reflection and Isolation between RHCP port and LHCP port	74
3-22	Linear array model of antenna panels.	75
3-23	Results of NSGA-II optimization of the antenna cross-range pattern .	77
4-1	Running trend of On-Orbit Relative FIT Rate	83
4-2	Arbitrary N port microwave network.	85
4-3	Different combining techniques	88
4-4	Circuit level power combining architectures	90
4-5	Kurokawa rectangular cavity combiner	92
4-6	Structure of cylindrical cavity TM_{0m0} combiner	93
4-7	Structure of four-way cavity combiner	93
4-8	Block diagram of an X-band 400W solid-state amplifier	94
4-9	Suspended microstrip line corporate power combiner	94
4-10	Drawing of 8-way microstrip combiner with important parameters . .	95

4-11	Qualitative structure of proposed cylindrical cavity power combiner. . .	97
4-12	Illustration of TM_{010} mode in cylindrical cavity	97
4-13	Cylindrical cavity mode chart.	99
4-14	Microstrip line interface to cavity	100
4-15	Heat flow versus temperature change. $Dk = 3.5$ Laminates.	101
4-16	Rectangular waveguide interface to cylindrical cavity	102
4-17	Reduced model of the power combiner.	103
4-18	HFSS full model simulation	105
4-19	Illustration of power combiner assembly process	107
4-20	Power combiner simulation versus measurement results.	108
4-21	Power combiner measured degradation characteristics.	109
5-1	Reflection s_{11} versus active S_1 for the prototype power combiner. . . .	117
5-2	Feeder network configurations	119

List of Tables

2.1	Survey of antenna and RF power transmitter technologies used in previous SAR missions	22
2.2	Dimensions and Weight of Antenna Panel	33
3.1	Excitation of n^{th} radiator in terms of the coupling coefficient.	43
3.2	HFSS slot-pair model parameters	46
3.3	Optimization parameters	57
3.4	Sakakibara approach vs Our approach	58
3.5	Comparison of the dual-polarization antenna panel with single-polarization, uniform aperture excitation rectangular parallel-plate slot-pair array antenna.	73
3.6	Optimization parameters for crossrange pattern synthesis.	76
4.1	Summary of Power Combining Methods	91
4.2	Reduced model of the power combiner	103
4.3	Optimization variables for the reduced model.	104
4.4	Optimization variables for the full model.	106
4.5	Power Combiner: Simulated versus Measured Characteristics	109

Chapter 1

Introduction

1.1 Background

Miniaturization of technology in general is desired since it can lead to lower volume, mass and easy handling of the end product. With respect to satellite technology, it has the added benefit that it lowers the launch cost of the satellite to orbit. Additionally, it allows launch of multiple satellites to orbit using the same rocket launcher. This is critical in today's era, when the number of rocket launches yearly are relatively low. Another motivation for development of small satellite (<150 kg) is that it makes affordable, a constellation mission consisting of numerous distributed satellites. Such a constellation of satellites allows for ubiquitous monitoring of our planet, which makes possible different applications such as near real time imaging [1] of our planet.

Optical small satellite constellations have shown how, with some compromise in resolution; wide coverage and rapid re-visits can be achieved [2]. An example is the RapidEye Earth observation satellite constellation launched on a single Russian Dnepr rocket in the year 2008 [3]. Each satellite weighs 150 kg and size of 1 m x 1 m x 1 m. The RapidEye sensor images five optical bands in the 400-850 nm range and provides 6.5 m pixel size at nadir. The satellites follow each other in their orbital plane at about 19 min intervals (Fig.1-1). The RapidEye system can access any area on Earth within one day and cover the entire agricultural areas of North America and Europe within five days.

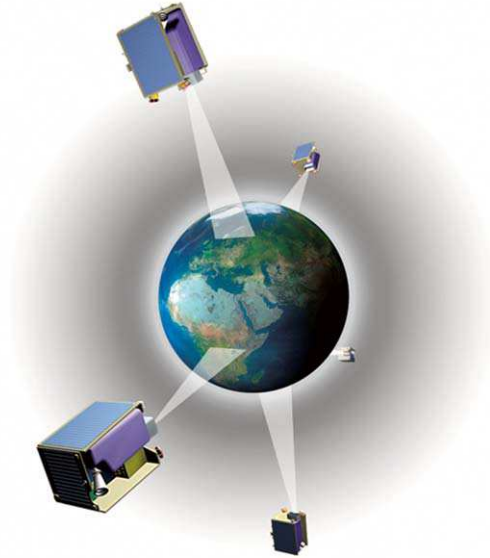


Figure 1-1: Illustration of RapidEye constellation [3]. A revisit time of one day can be obtained anywhere in the world ($\pm 70^\circ$ latitude) with body pointing techniques. The average coverage repeat period over mid-attitude regions (e.g. Europe and North America) is 5.5 days at nadir. The RapidEye system can access any area on Earth within one day and cover the entire agricultural areas of North America and Europe within five days.

In the present year, there are a number of small-satellite companies, which aspire to build a near real-time imaging system for the entire planet! An example is the GRUS mission of Axelspace, Japan, which plans to launch satellites of less than 80 kg, capable of obtaining images of 2.5m ground resolution [4]. Other notable efforts in the industry are by Planet Labs, USA [5] and Skybox Imaging, USA [6].

This dissertation focuses on another challenging Earth observation technique, namely active remote sensing of Earth by SAR. From an application point of view, SAR remote sensing has the advantage over optical imaging in mainly two criteria: (1) SAR is not dependent on illumination from Sun, and hence can take images at night, unlike passive optical sensors. (2) SAR imaging signals can penetrate clouds and aerosol cover over the atmosphere (penetration ability depends on the frequency of operation) unlike optical images. This is because electromagnetic waves at visible and near-visible spectrum is mostly either scattered or absorbed by clouds or dust particles. For these reasons, it is called an "all-weather instrument" [7][Chapter 1]. Furthermore, if the SAR can obtain polarimetric data of the target (i.e. if the SAR

could recognize the polarization of the scattered, incoming electromagnetic wave from the target), more information of target such as its geometric and electrical properties can be inferred [7].

Traditionally, SAR has been implemented on "large" and expensive satellite platforms. An example of which is the TerraSAR-X shown in Fig.1-2, which is an X-band Low Earth Orbit (LEO) Earth-observation SAR satellite launched 15 June 2007. It has a launch mass of 1230 kg, 4.88 m length and diameter of 2.4 m. The total cost of manufacturing and launching the satellite amounted to 130 million euro (about 174.5 Million USD) [8].

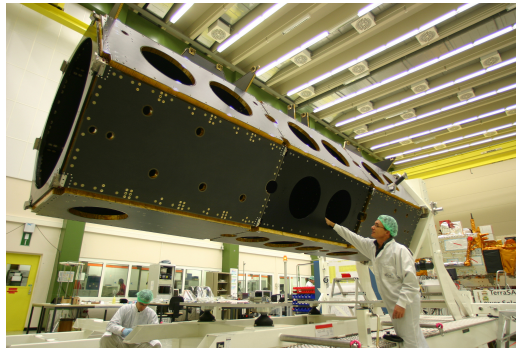


Figure 1-2: The German radar satellite TerraSAR-X is built by EADS Astrium, in Friedrichshafen, Germany. Credit: EADS Astrium

The revisit time (i.e. the time interval between visits over the same geographical place by the satellite) is dependent on the incidence angle, beam mode and geographic location of the swath [9]. It is typically large for a single satellite (e.g. TerraSARX with 11-day repeat cycle [10], ERS 1/2 and ENVISAT with 35-day repeat cycles, RADARSAT-1/2 with 24-day repeat cycles and ALOS with 46-day repeat cycle [2]). Similar to the case of optical remote-sensing satellites, the revisit time can be improved by having a constellation of satellites. For example, the Cosmo-SkyMed constellation (reconnaissance and civil applications) with four identical satellites and the SAR Lupe constellation (reconnaissance) with five identical satellites, have revisit time of 7 h and less than 10 h respectively [9].

However, even the SAR satellites used in Cosmo-SkyMode and SAR-Lupe constel-

lations are of large class (1700 kg and 700 kg respectively [9]). Including the launch costs, the overall constellation mission becomes expensive. On the other hand, if a single small satellite SAR was realized, it could drastically cut down the costs associated in achieving near-real time, all-weather Earth observation system.

1.1.1 The MicroXSAR mission

The motivation for developing a small satellite SAR system is abundant and discussed in the previous paragraphs. To realize this goal the Japan Aerospace Exploration Agency (JAXA) is actively working on a project, called MicroXSAR [11] [12][13] to realize a small satellite SAR. This dissertation is largely conducted a part of that project. The goal of the project is to realize an LEO X-band SAR satellite of mass less than 100 kg, and of a compact structure so it can be launched in piggy-back condition. The total mission cost is said to be less than 20M USD, therefore, paving the way to realize a constellation SAR mission consisting of many such small SAR satellites.

1.2 SAR Imaging

The word radar stands for 'radio detection and ranging'. The principle behind a simple radar instrument is to transmit an RF pulse and wait to receive its echo from a scatterer (if present). The time needed to wait is recorded, and the distance from the radar to target is calculated as $R = \frac{1}{2}ct$. Here c is speed of light, t is the waiting period and R is the distance to target called as range.

Fig.1-3 shows typical imaging geometry used by an airborne, space radar instrument. The direction along the motion of instrument is called along-track, azimuth or cross-range direction. The direction perpendicular to the motion path on the ground is called cross-track or range direction. The presence or absence of a scatterer, and level of signal echoed at a particular range, cross-range coordinate is determined and a 2-dimensional image of the area targeted in developed. In case of polarimetric imaging (see Fig.1-4), scattering coefficients $S_{xx}, S_{xy}, S_{yx}, S_{yy}$ (x, y stand for orthogonal

polarization states) are also measured.

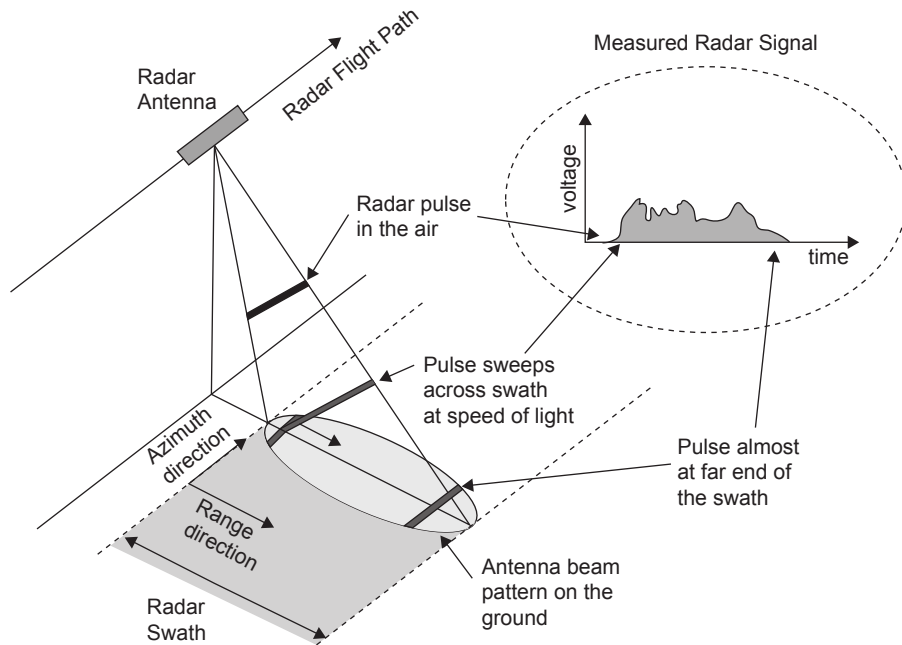


Figure 1-3: Imaging geometry of a side-looking radar system [7]

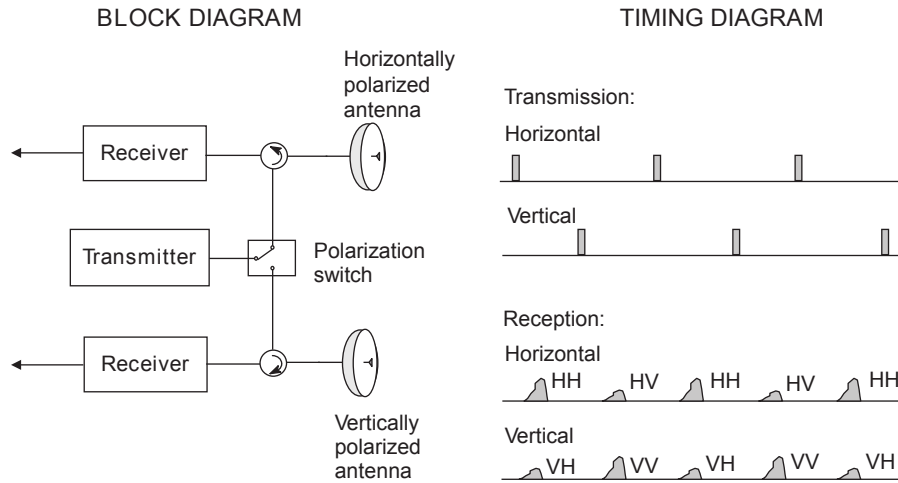
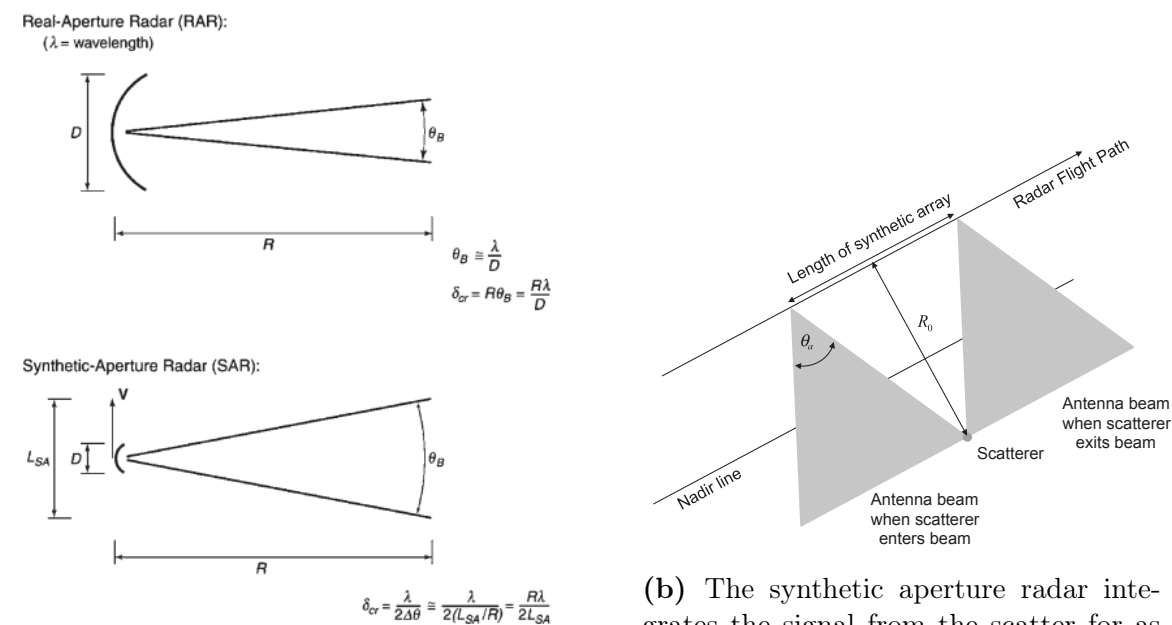


Figure 1-4: [7] A polarimetric radar is implemented by alternatively transmitting signals out orthogonal polarized antennas (figure shows linear H and V polarizations) and receiving at both polarizations simultaneously. Two pulses are needed to measure all the elements in the scattering matrix. Note: Notation XY means 'Y' polarization transmit and 'X' polarization receive.

Since radar-imaging measures position of scatterer in range, cross-range directions, there are two spatial resolutions associated with a radar image: range resolution and cross-range resolution. The resolution of an image is defined as that separation between the two closest features that can be resolved. 'Finer' the resolution implies we get more information about the imaged area. A Real Aperture Radar (RAR) (i.e. a radar not using synthetic aperture processing and is thus conceptually simpler) and the SAR can be shown to achieve range-resolution of $\delta_r = c/2B$ provided a suitable transmitting waveform of bandwidth B is used in the transmit pulse [14][Eqn(17.7)].



(a) Comparison of RAR and SAR: The crossrange resolution (peak-to-first-null of the antenna pattern) of an SAR is one-half that of a RAR of the same aperture diameter [14][Figure 17.2].

(b) The synthetic aperture radar integrates the signal from the scatterer for as long as the scatterer remains in the antenna beam [7].

Figure 1-5: Crossrange resolution synthesis in SAR.

The difference between RAR and SAR is in the way they achieve cross-range resolution (see Fig.1-5a). For RAR, the azimuth resolution δ_{cr} is simply the length of the footprint of the antenna beam in cross-range direction. $\delta_{cr} \approx R\lambda/D$ where D is the dimension of antenna in cross-range direction, R is the range and λ is the wavelength of operation [14][Eqn(17.1)]. Note that to get a finer resolution, we need

a larger antenna (larger D). For example, to achieve $\delta_{cr} = 10\text{m}$ from LEO satellite orbiting at $R = 600\text{km}$ at X-band frequency $\lambda = 3.1\text{cm}$ we would require the length of RAR to be 1.86 km!

For SAR, on the other hand, it can be shown that the cross-range resolution is $\delta_{cr} \approx R\lambda/2L_{SA}$ where L_{SA} is the length of the artificially synthesized aperture (see Fig.1-5b) due to the moving SAR platform [14][Eqn(17.2)]. $L_{SA} > D$ which implies a finer cross-range resolution can be achieved by SAR for the same antenna as compared to RAR. In a particular imaging mode of SAR called strip-map mode, it can be shown that $\delta_{cr} \approx D/2$ [14][Eqn(17.4)]. Thus to obtain 10 m cross-range resolution for LEO satellite imaging at X-band, we would need an antenna of length only 20 m using SAR against the 1.86 km using RAR. In fact, it implies smaller the antenna dimension, finer the cross-range resolution. However, the dimension of the antenna cannot be made arbitrarily small, since there are lower constraints on the antenna area depending on the swath-width being imaged [15] and required image Signal to Noise Ratio (SNR) [16][3.5.2].

One way to understand this phenomenon is to think of it as a discrete linear antenna array formed by the moving platform, as the platform passes the scatterer (Fig.1-5b). The elements of this discrete linear array are not all excited at once, but sequentially. The spacing between these individual radiators and the number of radiators depends on the velocity of platform and pulse repetition frequency. As long as the SAR operating parameters are such that these individual radiators are close together to prevent grating lobes in angular direction of interest, and the exciting pulses are properly phased, an artificially long antenna array equivalent of a real continuous antenna of dimension L_{SA} can be synthesized [17].

In this section, a glimpse of imaging using SAR is described and associated nomenclature introduced. For a more in-depth treatment, please refer to [17], [14], [18] and [7].

1.3 Research Objectives and Approach

Although the principles of SAR are fairly mature and investigated thoroughly, there are technological innovations required to realize it on a small satellite platform. The physical size, mass of the system and power budget are severely constrained for a small satellite platform. The way we attempt to overcome this problem is to take into advantage new developments in related science and technologies and use them in our application of small satellite SAR. For example, as we shall see later, we apply the recent developments in meta-heuristic multi-objective optimization algorithms to solve an optimization problem related to antenna pattern synthesis of dual-feed traveling wave antennas. Furthermore, the methods used in this dissertation are not specific to SAR and may be applied in other diverse fields as well.

This dissertation concentrates on the development of the antenna system consisting of the physical antenna and RF power source. The main objectives of this research are two-fold:

1. Propose a suitable antenna system for small satellite SAR.

The research approach to this problem, is to first make a survey of previous space-based antenna systems used for SAR imaging and other similar applications such as high bit-rate telecommunications. The overall antenna system architecture (passive-array, passive phased-array or active phased-array), fundamental radiator technology (microstrip patch, slot-antenna, reflector antenna, etc.) and technology of RF power generation (solid-state or vacuum tubes) is discussed. Based on these background studies, a suitable antenna system architecture, antenna panel technology and RF power source technology is proposed.

2. Identify and solve key challenges relating to the proposed antenna system design.

Key challenged in realizing this design is identified, namely:

- (a) Optimization a traveling-wave antenna for SAR imaging.

The research approach in this problem is to first make a mathematical formulation of the optimization problem. Following which a survey of pre-

vious antenna optimization techniques is made. Based on the survey and discussion we select a meta-heuristic based multi-objective optimization algorithm to solve the optimization problem. This is implemented for the design of the antenna system. A single antenna panel is fabricated and electrical characteristics are measured based on the implemented design.

- (b) Design of a compact, low-loss RF power combiner to meet needs of high RF power source for SAR imaging.

The research approach in this problem, is to first make a survey on power-combining architecture, examples of their implementation and evaluate their strengths and weakness. Resonant cavity N-way RF combining architecture is deemed suitable for application in small satellite SAR. Next step is to implement the same, using least number of adapters from Solid-State Power Amplifier (SSPA) microstrip line power amplifier signal input to low-loss waveguide output. A prototype unit is fabricated and electrical characteristics measured.

1.4 Outline of Remaining Chapters

The remainder of the thesis is as follows. Chapter 2 surveys the antenna systems implemented in previous space based SAR missions. A general discussion based on the survey follows. The merits and demerits of implementing an active-phased array versus passive-array antenna are compared. To accommodate inside a small satellite bus, we reason the choice of a passive-array antenna system. Among many available antenna panel technologies, we select to implement a dual-polarization parallel-plate slot-pair array antenna panel. The uniqueness of this panel technology is that it can radiate/ receive two orthogonal polarizations over the same aperture. The dual-polarization capability is made possible by having two-orthogonal slots as the fundamental radiating element. By exciting this slot-pair in two-different directions, we can radiate either orthogonal circular polarization. Towards the end of this chapter, relation between antenna pattern characteristics and SAR image characteristics is also

studied. Suitable mathematical functions in terms of antenna parameters are formulated, whose maximization (or minimization) corresponds to enhancing the quality of SAR image.

Chapter 3 explores the problem of design of the chosen antenna panel technology in detail. The slot array antenna falls under the class of traveling-wave antennas. A traveling wave is excited in a waveguide, and in direction of propagation of the wave, energy is leaked from slot cut on the top-surface of the waveguide. This is a series feed antenna in which the excitation profile over the aperture depends not only on the present slot geometry, but also on the previous slots. Since we intend to implement dual-polarization (and hence dual-feed), this imposes certain restrictions on the type of slot-geometries, which may be employed. Various antenna pattern synthesis algorithms are surveyed, and their merits and demerits are discussed. A meta-heuristic multi-objective optimization algorithm is chosen, and optimization carried out by simulating a mathematical model of a traveling-wave linear array of slot-pairs. The optimization results are applied to build a detailed electromagnetic (EM) simulation model in computer. The simulated EM model of the antenna panel is later fabricated. The prototype unit is tested, and the measurement results are presented. The next problem dealt in this chapter is the optimal excitation of an array of identical antenna panels representing the entire SAR antenna system. Using the measurement results of previously fabricated single panel and the same meta-heuristic optimization algorithm, we synthesize optimal excitation coefficients of an array of panels. It is shown the synthesized excitation profile performs better than a traditional uniform excitation profile in terms of enhancing the quality of SAR image.

Choosing a passive-array system architecture brings about the challenge to implement a high-power glsRF transmitting source at the center. This challenge is discussed in Chapter 4. Primarily there are two technologies favorable to achieve this purpose: SSPAs and vacuum-tube based amplifiers. A comparison is drawn between the two in terms of power output capability, efficiency, size, reliability, etc. We choose to implement SSPA based high RF power source and meet the high-power requirement by coherently combining output of several SSPAs. Characteristics of power

combiners are reviewed and different power combining architectures are surveyed in this chapter. Based on the survey, we choose a suitable power combining architecture and propose a cylindrical cavity power combiner with microstrip line inputs and waveguide output. The design process of this power combiner is presented along with comparison of measurement and simulation results.

Chapter 5 summarizes the entire dissertation and highlights the contributions of this work. Additionally, presented is a proposal for future work.

Chapter 2

Antenna Systems for Space-Based SAR

In this chapter, the antenna systems of previous space-based SAR satellites are surveyed (Section.2.1). Note that these missions were carried out with large satellites. Based on this survey, suitable antenna system architecture for small satellites is selected, namely a passive planar array antenna with deployable rectangular panels (Section.2.2) and a centralized high-power RF source. This antenna system architecture allows for low-cost development and compact size, which can be accommodated onto a small satellite bus. Further, a rectangular parallel plate slot-pair array antenna is chosen as technology for single panel due to its low loss characteristics at X-Band, smaller weight and deployment friendly structure. Two main challenges are identified to realize this antenna system architecture: (1) Antenna panel design optimized for SAR imaging. (2) High-power central RF source at X-Band.

In Section.2.3 the relation between antenna characteristics and SAR performance metrics such as image SNR and ambiguities is studied. This is later helpful in the Chapter.3 when we seek to optimize antenna design for SAR application. Finally, we summarize in Section.2.4.

2.1 Survey of Previous SAR Antenna Systems

Table.2.1 shows a survey of a number of antenna systems used in previous space-borne SAR missions. The SAR missions were selected to showcase the variety in technologies being used. From this survey, we can make some general observations. In terms of the structure, planar multi-panel and reflector antennas have been implemented. Planar multi-panel antennas are popular for their compact pre-launch packaging and deployment friendly mechanical structure. In terms of the fundamental radiator, microstrip patches, waveguide slot-arrays, parabolic reflectors have been used in C, L-Band SAR, while waveguide slot-array, parabolic reflectors are used in X-Band. The pioneer among space-based SAR, the Seasat-A implemented a passive-array architecture, while many of the subsequent planar array based antennas implemented active phased-array technology. Active phased-array technology was made possible using distributed Transmit-Receive Modules (TRMs) on the antenna panels. In satellites using multiple polarizations, separate feed network is provided for orthogonal polarizations. Reflector based antennas such as the one in TecSAR (reflector parabolic dish), use multiple feeders to provide beam-steering capability.

In terms of the RF power source, active phased-array antennas use a distributed transmit module network with 100s of low power SSPAs. The transmit module has separate calibration data for each of the amplifiers to allow for accurate pattern formation. Reflectors antennas on other hand need to have a centralized RF power source, ex: TecSAR using Travelling-Wave Tube Amplifiers (TWTAs). Passive planar antennas such as Seasat-A too used a centralized RF power source (Solid-state, L-band). Centralized RF power source requires high-power output from a single module, which is made possible using parallel combination of many drivers, such as in the case of Seasat-A, where power from three SSPAs are combined in parallel and in case of TecSAR where power from eight CWTAs (RF amplifier unit made of TWTA) is combined and directed to antenna feed.

Table 2.1: Survey of antenna and RF power transmitter technologies used in previous SAR missions

Name and launch date	Frequency	Polarization	Antenna Size	Antenna Technology	RF power	Power transmitter technology	Payload Mass	References
Seasat-A 28 June, 1978	L-Band, 1.275 GHz	HH	10.74 m x 2.16 m	Passive, Planar 8 microstrip array panels Each panel split into 8 x 16 rectangular patch elements which is then split into 4 x 4 element arrays.	Centralized Corporate power feeder employing air-filed coaxial cables.	Solid State Output of 3 parallel power am- plifiers is combined to produce peak output power of 1 kW.	223 kg	[19] [20, Pg 189][21] [22] [23]
Magellan 4 May, 1989	S-Band 2.385 GHz	HH	3.7m diam- eter	Passive Parabolic dish made of graphite-epoxy sheets mounted on aluminium honeycomb for rigidity. Shared with telecommunica- tions subsystem.	Centralized	TWTA Peak power: 400 W	sensor weight without antenna: 154 kg	[24] [25] [26]
ERS-1 17 July, 1991	C-Band 5.3 GHz	VV	10m x 1m	Passive Slotted waveguide array, made of metallised CFRP. 10 elec- trical subpanels of 1m x 1m. Each subpanels has 20 radi- ating broad-wall slot wave- guides and 4 dummy wave- guides. 10 coupling waveguide on the back of each subpanel distributes RF power through inclined slots.	Centralized A main waveguide feed network feeds power to the coupled waveguides on each panel via shunt-series slots	TWTT Peak output power: 4.7 KW Average output power: 300 W Bandwidth: 32 MHz	SAR weight: 512 kg	[27] [28] [29] [30] [19]

Name and launch date	Frequency	Polarization	Antenna Size	Antenna Technology	RF power	Power transmitter technology	Payload Mass	References
RADARSAT-1 4 Nov, 1995	C-Band 5.3 GHz	HH	15m x 1.5m	Phased-array with electronic beam-steering in elevation. Antenna system split into four panels. Set of 32 waveguide-slot radiator rows are placed in vertical dimension each preceded by ferrite phase shifter. Small azimuth taper is provided (for azimuth pattern sidelobe suppression) while in elevation it is uniform amplitude excitation.	Centralized 5000 W (peak), 300 W (avg)	TWWT	-	[31] [32] [33]
TerraSAR-X 15 June, 2007	X-band 9.65 GHz	HH, HV, VH, VV	4.8 m x 0.7 m	Active phased-array Planar 3 leaves, each leaf has 4 panels, 32 dual-polarized subarrays per panel. fundamental radiator is 40 cm long slotted waveguide.	Distributed Each subarray is driven by T/R module (amplitude and phase control) RF signal distribution via microstrip dividers in panel level, coaxial cables between panels.	Solid State 38 dBm per T/R module 2 kW peak radiated power	394 kg	[34][35]
RADARSAT-2 14 Dec, 2007	C-Band 5.405 GHz	HH, HV, VH, VV	15 m x 1.4 m	Active phased-array Planar 4 panels, each panel has 4 columns. Each column has 32 subarrays. The sub-array is made of 20 dual-polarization cavity backed patch antenna. All elements is sub-array are excited uniformly.	Distributed Each sub-array (512 in total) has a T/R module RF signal distribution is through a combination of stripline, suspended stripline and waveguide dividers.	Solid State T/R module is capable of 40.1 dBm output power.	784 kg antenna mass	[36] [37] [38]

Name and launch date	Frequency	Polarization	Antenna Size	Antenna Technology	RF power	Power transmitter technology	Payload Mass	References
TecSAR 21 Jan, 2008	X-Band 9.59 GHz	HH, HV, VH, VV	3-m diameter	Beam-steering with multiple feeders. Parabolic mesh reflector	Centralized	TWTA Multi-tube transmitter (MTT has 10 CWTAs (2 redundant). Each CWTA has a TWT, RF driver and HVPS. Power from these 8 CWTAs is combined and directed to antenna feed.	100 kg	[39] [40]
Cosmo Skymed constellation mission 8 June 2007, 9 December 2007, 25 October 2008, 6 November 2010	X-Band 9600 MHz	HH, VV, HV, VH	5.7m x 1.4m	Active phased-array Three mechanical panels made up of "Tiles". Each Tile has 4 radiating boards of 8 linear arrays. Entire antennas has 40 Tiles. Each linear array is dual polarized with 12 stacked patches. Two distribution networks, one for each linear polarization to feed the linear array.	Distributed 32 T/R modules per Tile	SSPA	-	[41] [42]
RISAT-1 26 April, 2012	C-Band 5.305 GHz	HH, HV, VH, VV, Hybrid: Circular Tx, V,H Rx	6 m x 2 m	Active phased-array Planar 3 deployable panels, each panel of size 2m x 2m. Each panel divided into 4 tiles of 1m x 1m size. Each tile has 24 dual-polarized linear arrays aligned in azimuth direction. Each linear array of length 1 m has 10 equispaced microstrip patches.	Distributed Each linear array is powered by 2 TR modules (one for each polarization). Weighting is applied in signal reception.	Solid-State During transmission TR modules operate in saturation condition. peak RF power fed by each TR module is 10 W at 7% duty cycle.	950 kg	[43]

2.1.1 Antenna Array Architectures

To form a high-gain antenna, a large aperture size is required. This can be made possible by simply enlarging the antenna physical dimensions as in the case of parabolic reflector antennas, where the diameter of dish can be increased to achieve a higher gain. Another way to enlarge the dimensions of the antenna, without necessarily increasing the size of individual elements, is to form an assembly of radiating elements in an electrical and geometrical configuration [44] (example make an array of parabolic reflector antennas). Further the phase and amplitude at each individual element can be varied to synthesize a variety of beams from the same antenna. The trade-off is the increased complexity and cost of the system.

The simplest array architecture is shown in Fig.2-1. It has a centralized High Power Amplifier (HPA) and RF feed network. The excitation amplitude and phase of the individual radiators are fixed and cannot be varied. This architecture has the least complexity and requires the least number of components. Example of this antenna architecture is the antenna systems of Seasat-A and ERS-1.

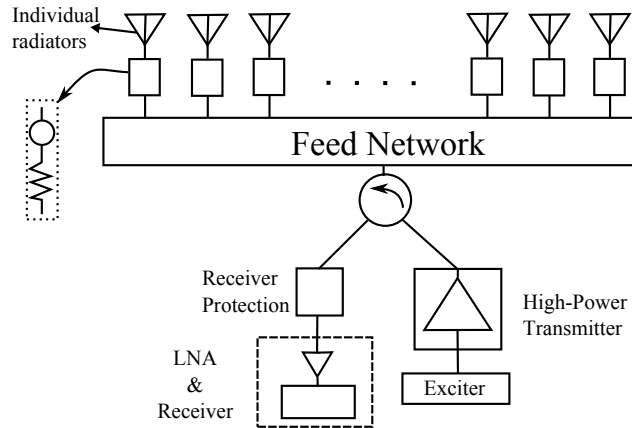


Figure 2-1: A passive antenna array.

The challenge in implementing this simple architecture is the need of a centralized high-power RF source along with a low-loss power-divider network. For example, Seasat-A uses a central RF source made of SSPAs with peak power capability of 1kW and a low-loss air-filled coaxial cable power divider network. The use of conventional

coaxial cables for the corporate feed network was ruled out due to high loss, and a corporate feed network using vacuum as the dielectric was developed. This corporate feed network used a solid center conductor in a rectangular structure suspended by solid supports [21].

Synthesizing beam by varying the amplitude and/ or phase at the individual elements is called as electronic scanning. This enhances the capability of SAR by allowing synthesizing of different antenna patterns depending upon the imaging conditions. For example, imaging at higher incidence angles requires lesser main-lobe beamwidth as compared to imaging at lower incidence angles (keeping the swath-width of the imaged area constant). Electronic beam-steering may also be used in spotlight mode SAR as used in ALOS-2 mission [45].

There are mainly two kinds of electronically scanning array (phased-array) antenna architectures [46] as shown in Fig.2-2.

1. Passive phased-array antenna

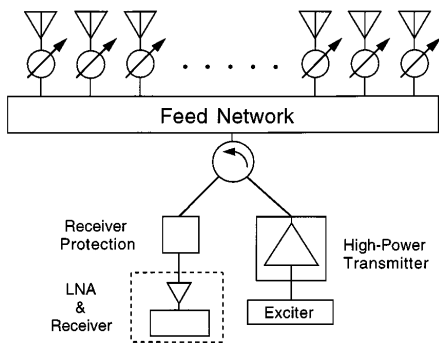
In passive phased-array, there is no element amplitude control; only bilateral phase shifters are used for each element to provide the required phase shift for scanning [46]. The RF power source is still centralized, and phase shifters are employed in the final carrier frequency stage. An example is the RADARSAT-1 antenna which provides ferrite-based phase shifters along one dimension of the rectangular array.

2. Active phased-array antenna

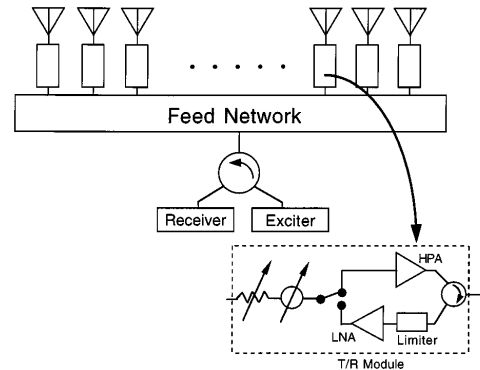
In an active phased-array, a TRM is used for each element to provide amplitude and phase control. The RF power source is distributed throughout the array which reduces the requirement of power output of each power amplifier. There are numerous examples of active phased-array space-based SAR implemented in large satellites such as TerraSAR-X, RADARSAT-2 and RISAT-1.

Besides providing flexibility in amplitude and phase control for the array elements (and hence transmit/receive beam control), other advantages of active array architecture are as follows [46]: (1)The system sensitivity is increased

because the system noise figure is set, and the RF power is generated at the aperture. (2) The feed networks need not be optimized for the lowest loss; thereby allowing design flexibility and the ability to minimize size (volume) and weight.



(a) Linear passive array with phase shifters for every element [46].



(b) An active array with transmit-receive modules at every element [46].

Figure 2-2: Architecture of electronically scanned (phased-array) antennas.

Another architecture receiving much interest in today's research is Digital Beam Forming (DBF) (Fig.2-3). Here the RF signal at each receiver element is digitized and stored. A transmit pattern with a large beam-width may be during transmission, and later received signal recorded digitally at each radiator. Multiple high-gain narrow receive beams can be synthesized in software. Nulls can be placed in the directions of strong interferers (such as the nadir echo), thus reducing ambiguous energy. In this architecture, interference emanating from undesired directions is not canceled out after signal processing, therefore, all the elements, including the RF mixer and Analog to Digital Converter (ADC) and the Digital Signal Processing (DSP) unit must have sufficient dynamic range capable of handling the interferers [47].

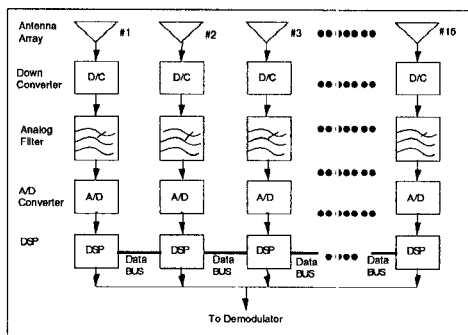


Figure 2-3: Configuration of receiving DBF [48].

Although phased-array systems provide flexibility and more capability to SAR systems, they come at an expensive price: (1) Increased cost. (2) Increased weight (3) Increased power consumption (4) High complexity. All these factors are a consequence of using a distributed architecture with multiple TRM modules. A good summary of challenges in conventional phased-arrays may be found in [47, Pg. 30]. Low cost phased-array architectures is another hot topic of research in present time.

Design of TRM modules is also challenging since it requires fitting all RF front-end components into a small package. The size requirement of the package is dictated by the inter-element spacing of array and hence wavelength of operation. Cooling solution has to be provided so that the amplifier efficiency is not degraded due to self-heating. Higher resolution of the digital phase shifter in TRM module implies larger size and cost. Summary of TRM design challenges can be found in [49, Pg. 5].

2.2 A Passive-Array Centralized RF Feed SAR Antenna System for Small Satellites

Considering the pros and cons of passive-array antennas, and phased-array antennas, a passive array antenna is deemed suitable for a low cost, small satellite SAR. Avoiding the use of distributed RF feed with TRM modules leads to cut down in costs, weight (tied to the launch cost), volume and complexity in the system. Furthermore, a completely passive system allows for relatively easy mass-manufacturing.

Compared to planar array antennas, reflector-based antennas can achieve higher efficiency with large apertures, and have a lower cost and wider bandwidth [50]. However rectangular multi-panel antenna is preferred over reflector antenna since rectangular multi-panel antenna can be packaged compactly before launch as compared to reflector antennas.

This leads to mainly two challenges in realizing this system, which is addressed in this thesis:

1. Realization of a passive-array antenna which shall be optimized for SAR application. Since the antenna is passive array, the antenna pattern is fixed, and it shall have to be optimal over a wide range of SAR operating range (look-angle, pulse-repetition-frequency).
2. Realization of a compact high-power RF power source (in X-Band), which can be accommodated in a small satellite bus.

2.2.1 Selection of Antenna Panel Technology

An important deciding factor in selection of antenna technology is its heritage of the technology of having flown in space. The survey in Section.2.1 shows numerous antenna technologies successfully used in space-based SAR systems. Microstrip patch antennas are favoured at lower frequencies (S, L, C Band) (ex: Seasat-A, RISAT-1, RADARSAT-2) because of their low profile and easy fabrication. At higher frequencies' slot-array waveguide antennas are favoured since they have lesser loss using only vacuum as the dielectric (ex: TerraSARX). The patch solution, though it shows larger bandwidth and lower cost as compared to waveguide solution, at higher frequencies suffers from ohmic losses and cross-polarization due to radiation from both patch and microstrip lines [50].

To further reduce the weight of the system and manufacturing complexity a rectangular parallel-plate slotted panel was chosen [51]. To the author's knowledge, the first work on waveguide-fed parallel plate slot array (parallel slot-pair) antenna is reported in [52]. It has a very simple structure with radiating part being a upper

conductor plate in which slot pattern is etched (see Fig.2-4). A plane transverse electromagnetic (TEM) wave is excited in the parallel plate guide by rectangular waveguide-fed feed slots cut in the back conductor [52]. The TEM wave then couples to the radiating slot pairs, radiating linearly polarized waves. An X-band antenna with uniform aperture illumination was demonstrated with 54% aperture efficiency, thus demonstrating feasibility of antennas of this type.

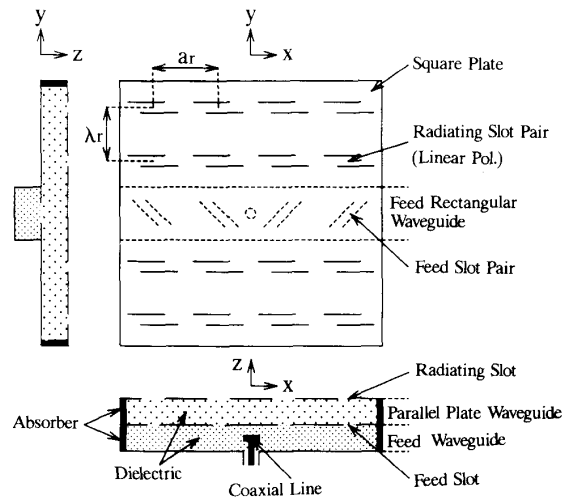


Figure 2-4: Waveguide-fed parallel plate slot array antenna configuration [52].

Structurally similar radial line slot antenna (RLSA) was flown on the Venus Climate Orbiter AKATSUKI mission [53] [54]. The RLSA consisted of a 5mm honeycomb core between two thin copper-coated skins [54]. Radiating slots are etched on the upper skin, and the bottom skin has a small hole in the center for coaxial probe feeding (see Fig.2-5). A directivity of 36.0dBi with aperture efficiency of 63.7%, 8.4 GHz design frequency was achieved for the flight model reported in [54].

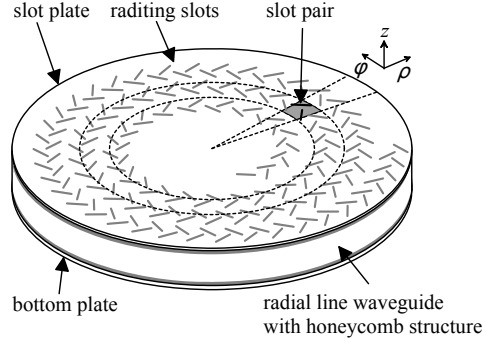
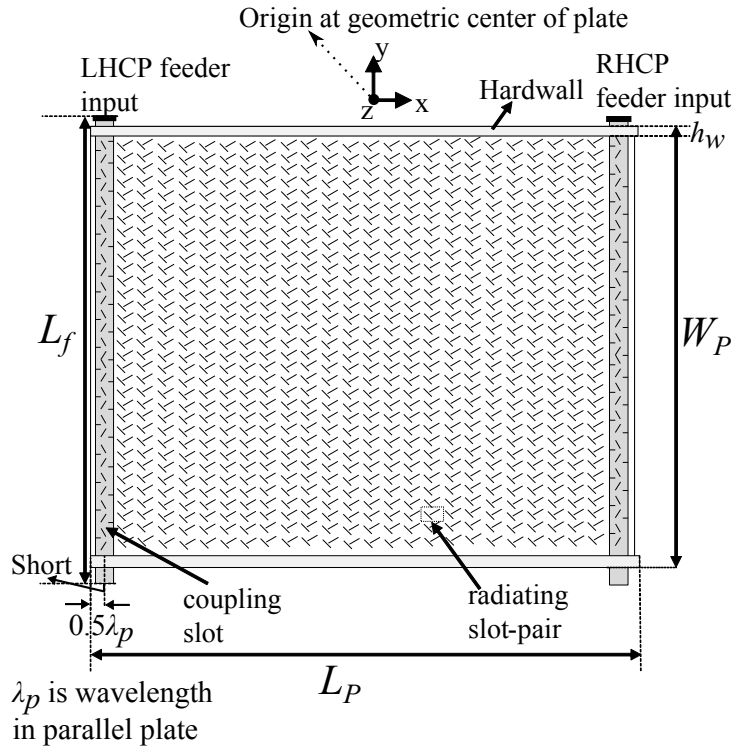


Figure 2-5: Radial line slot antenna with honeycomb structure [54].

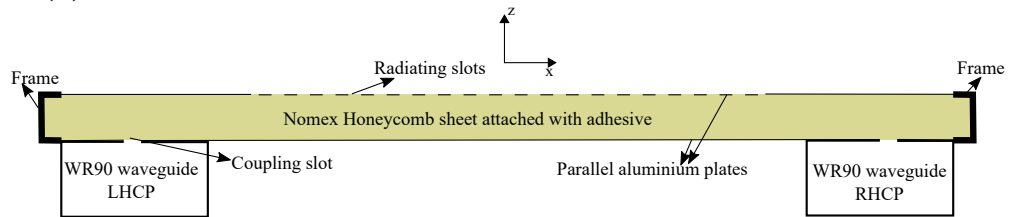
The space heritage of a structurally similar flat RLSA antenna used in AKATSUKI mission, and feasibility of parallel plate waveguide fed slot antenna demonstrated in [52], prompted the proposal of rectangular parallel plate slot-pair array antenna as our choice of antenna panel technology. The radiating slot-pair was, however, proposed to be a orthogonal pair against the parallel slots used in [52], to allow radiation of circular polarization. To demonstrate the feasibility of the proposed rectangular parallel plate slot-pair array antenna, a single-polarization (Right Hand Circular Polarization (RHCP)) parallel plate slot array antenna was designed using computer simulation software for uniform aperture excitation. Detail of this work is given in [51][55]. We use identical panel structure for the proposed SAR antenna, however, with dual-polarization. Introducing dual-polarization restrict the allowable aperture excitation over the antenna panel and use of uniform excitation is not allowed (see Section.3.3.3). An important objective of this thesis is to find an optimal aperture excitation over the panel which maximizes SAR image quality.

Fig.2-6 shows the antenna panel structure. It has rectangular aluminum parallel-plates, separated by a honeycomb core [56] attached to the aluminum plates by means of adhesive [57]. The top metal layer has slot-pairs through which energy is leaked. Two feeder waveguides (TE_{10} mode) with alternating slots couple power into the parallel plate. Dielectric hard-walls are placed at both sides perpendicular to the feeder waveguides to support quasi-TEM wave along x-axis [58]. If the Left Hand Circular Polarization (LHCP) feeder waveguide is excited, electromagnetic wave in

quasi-TEM mode is excited in the parallel plate travelling in the $+x$ direction. This excites the slot-pair to radiate LHCP waves. Similarly if the RHCP waveguide feeder (WR90) is excited, quasi-TEM wave travels in x direction and the panel radiates RHCP waves.



(a) Structure of parallel plate slot-pair array antenna.



(b)

Figure 2-6: Structure of parallel plate slot-pair array antenna.

Table 2.2: Dimensions and Weight of Antenna Panel

Parameter	Value
Parallel-plate ($W_p \times L_P$)	657.2 mm x 700 mm
Feeder Length (L_f)	678.4 mm
Hardwall width (h_w)	4.89 mm
Al sheet thickness	0.3 mm
Honeycomb core thickness	6 mm
Adhesive layer thickness	0.13 mm x 2 sheets
Total weight	1310 g

2.2.2 System Architecture

The preliminary antenna system configuration to be used for microXSAR small satellite mission is shown in Fig.2-7. It has seven rectangular antenna panels, which are excited by a rectangular waveguide feeder network. Each panel is a rectangular slot-pair array planar antenna (see Section.2.2.1) with two excitation ports. The excitation ports correspond to RHCP and LHCP radiation. The panel dimensions are approximately 70 cm x 70 cm. In the pre-deployment stage, the panels are folded onto the side-walls of the satellite bus. The RF power source is centralized at the satellite bus.

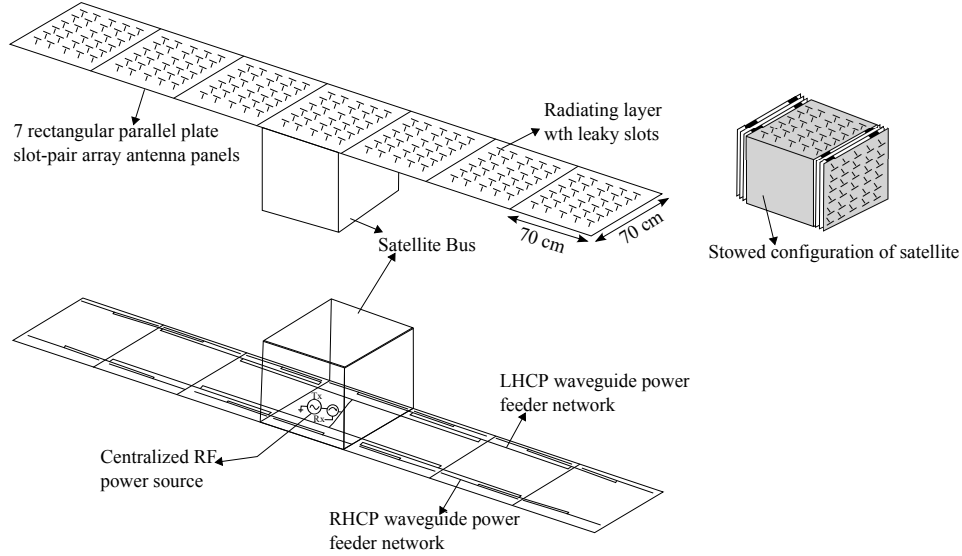


Figure 2-7: Antenna system architecture. It is a passive-array antenna system with seven rectangular parallel-plate slot-pair array antenna panels, excited by waveguide feeder. There are two waveguide feeder networks corresponding to each circular polarization. The RF power source is centralized at the satellite bus.

2.3 Relationship between Antenna Characteristics and SAR Performance

There are mainly two ways in which the antenna characteristics are related to SAR image.

2.3.1 Signal to Noise Ratio of Image (SNR_{image})

It can be seen that the SNR_{image} of a SAR image after processing is [16]:

$$SNR_{image} \propto G^2 \quad (2.1)$$

where G is the gain of the antenna illuminating the desired target region. Higher the SNR_{image} , "brighter" will be the image. Thus we desire high gain at the main-lobe of antenna pattern. The target region is illuminated over a finite beam-width of the main lobe. The gain of the main beam falls off from the peak direction. As a result

at directions away from the peak, the SNR_{image} degrades. Another requirement is that this degradation be small, which implies a flatter main-lobe.

2.3.2 Artifacts due to Range Ambiguity and Azimuthal Ambiguity

A detailed description of range and azimuthal ambiguities can be found in [18][17]. These ambiguities arise due to echo return from scatters outside imaging area of interest. Such returns result in so called "ghost images". An example of effect of range ambiguity on SAR images is shown in Fig.2-9.

Fig.2-8 illustrates the geometry of the side-looking SAR. The green area is the area to be imaged. However, the antenna pattern spreads out to other neighboring areas, and echo returns from these neighboring areas within the range and cross-range directions cause ambiguities. By suppressing the antenna gain pattern in the range, cross-range directions, we can suppress the ambiguous energy.

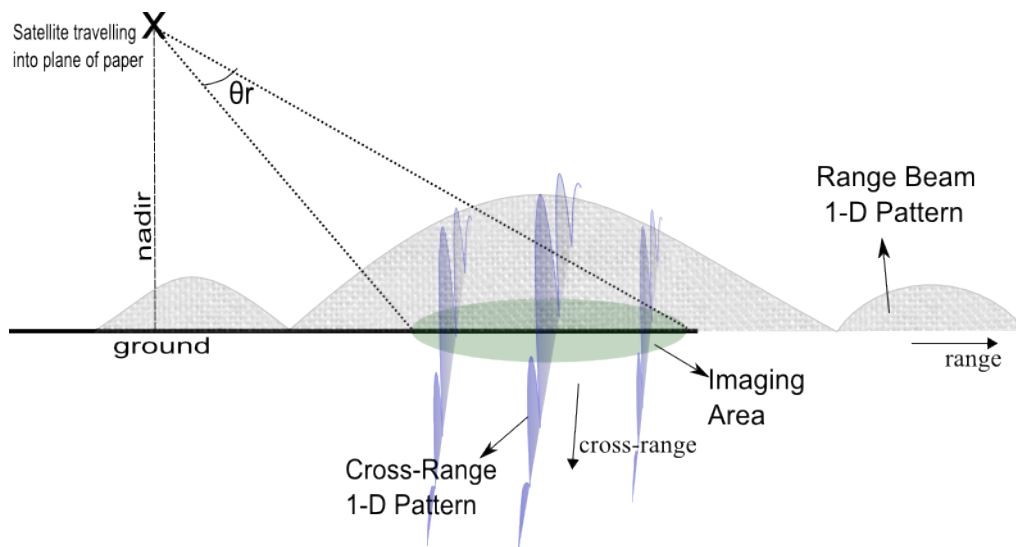


Figure 2-8: Range-pattern and Cross-range pattern

Note that the range, cross-range beam patterns are modulated by the distance factor ($1/R^4$ if we consider raw signal energy or $1/R^3$ if we consider processing gains [16]).

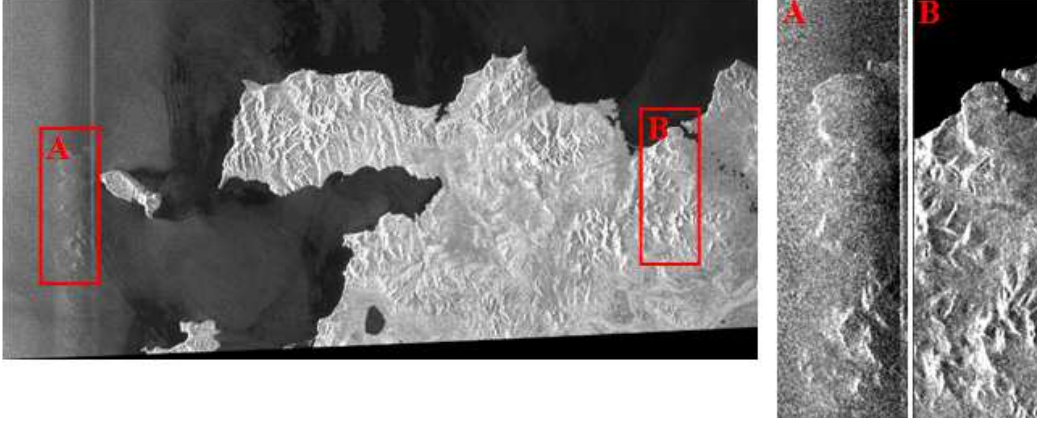


Figure 2-9: Example of effect of range ambiguity on SAR image. Above is an image of RADARSAT-1 in survey mode SWA (W1 + W2 + W3_S7). Range ambiguity signal (A) is seen on sea-surface due to echos from side-lobe in the region (B). Bright strip in left part of image is due to nadir ambiguity. Reproduced from presentation by Igo Elizavetin, "Radiometric artifacts on SAR images", Xth International Scientific and Technical Conference, September 2010, Italy.

The range-ambiguity is evaluated by a metric called Integrated Range Ambiguity to Signal Ratio (IRASR) as given by the following Eqn.2.2 [18, eqn. 6.5.20].

$$IRASR = \sum_{i=1}^N S_{a_i} / \sum_{i=1}^N S_i \quad (2.2)$$

where, S_{a_i} and S_i are respectively the range ambiguous and desired signal powers (at the receiver input) in the i th time interval of the data recording window, and N is the total number of intervals.

$$S_i = \sigma_{i0}^0 G_{i0}^2 / R_{i0}^3 \sin(\eta_{i0}) \quad (2.3)$$

$$S_{a_i} = \sum_{j=-n_h, j \neq 0}^{n_h} \sigma_{ij}^0 G_{ij}^2 / R_{ij}^3 \sin(\eta_{ij}) \quad (2.4)$$

where j corresponds to the pulse number ($j = 0$ is the desired pulse, j is positive for preceding interfering pulses and negative for successive interfering pulses), R_{ij} is the slant range at a given η_{ij} , G_{ij} the gain of antenna and σ_{ij}^0 is the normalized backscatter coefficient corresponding to look angle γ_{ij} , n_h is number of pulses to horizon.

The relation between γ and other SAR geometrical parameters for a flat Earth

model is shown in Fig.2-10. From this, we can write the following relation:

$$\eta = \cos^{-1}(h/R) \quad (2.5)$$

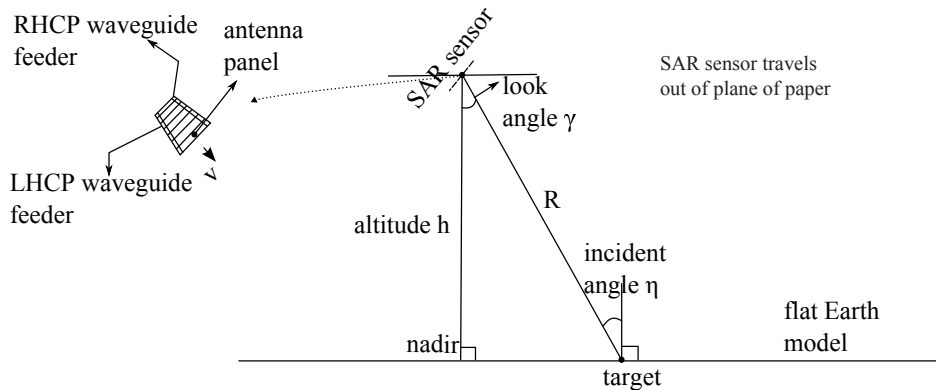


Figure 2-10: Geometry of SAR imaging in range direction

From Eqn2.2, we can see that the range ambiguity depends on imaging geometry, pulse repetition frequency f_p required swath-width and antenna gain pattern. At large incidence angles, the range ambiguity becomes severe because energy from the desired imaging region is attenuated greatly by the distance as compared to ambiguous signal energy at near incidence angles. It can also be seen that lower the f_p , lower will be the range ambiguity. Lower f_p means larger inter-pulse spacing, which means spacing between interfering echoes increases. However, the lowest f_p which can be implemented is bound due to azimuth ambiguity requirements. From a signal-processing perspective, [59] suggests the use of up-down chirp for successive transmit pulses. This technique reduces range ambiguity since effectively inter-pulse spacing is increased, while simultaneously achieving the requirement on azimuthal ambiguity.

A SAR satellite will have a wide range of operating parameters, which means a wide range of possible swath-width, η , γ and f_p . Echo returns from the nadir are strongest since it corresponds to shortest distance of SAR sensor from ground (see Fig.2-10). In case of active phased-array antennas, the returns from the ambiguous regions can be suppressed by placing nulls in the direction of the ambiguous returns [60]. In [61], author suggests an iterative technique to generate optimal "antenna

mask" depending upon the selection of f_p imaging geometry and a reflectivity profile (σ^0). The antenna mask template is selected to minimize antenna sidelobes, the noise-equivalent sigma zero (relating to SNR_{image}), and the radiometric accuracy (relating to antenna main lobe flatness).

However, these above methods rely upon knowing the imaging geometry and f_p . This is possible for an active phased-array system where an antenna beam pattern can be synthesized as required. In case of passive-array antennas, the antenna beam pattern is constrained to be the same irrespective of the operating parameters. For the case of passive-array SAR antenna, we can improve $IRASR$ by maximizing the ratio of total power radiated over the main beam to the power radiated over the entire pattern. This antenna beam characteristic is called beam-efficiency and is defined as follows:

$$B_E = \int_{\gamma=\langle ML \rangle} |F_R(\gamma)|^2 d\gamma / \int_{\gamma=\langle ALL \rangle} |F_R(\gamma)|^2 d\gamma \quad (2.6)$$

where B_E is the beam efficiency, F_R is the antenna 1-dimensional pattern in range direction, $\langle ML \rangle$ is angles over main-lobe, $\langle ALL \rangle$ means angles over entire pattern.

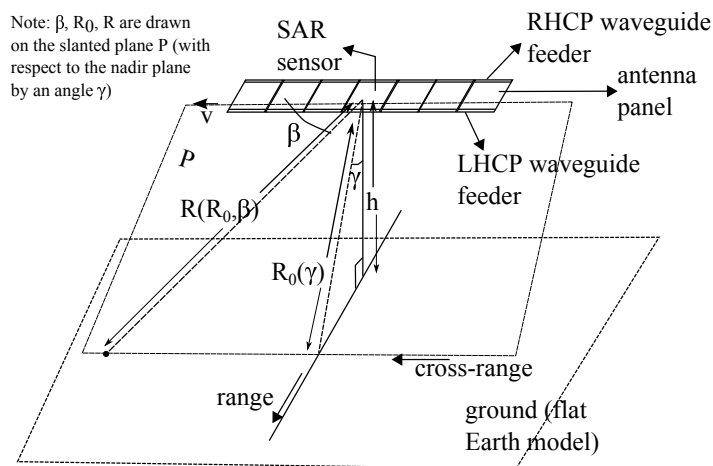


Figure 2-11: Geometry of SAR imaging in cross-range direction

The azimuth ambiguity arises due to echo returns from side lobes in the antenna pattern in cross-range plane (see Figs.2-8, 2-11). However, the imaging geometry is simplified for SAR radar systems with zero-squint angle (squinted refers to the case

when antenna boresight is not normal to the flight path [14]). We can include the effect of increasing signal power attenuation at far angles by defining the following antenna characteristic called modified beam efficiency B_E^M .

$$B_E^M = \int_{\beta=\langle ML \rangle} |F_{CR}(\beta)|^2 \sin^2 \beta d\beta / \int_{\beta=\langle ALL \rangle} |F_{CR}(\beta)|^2 \sin^2 \beta d\beta \quad (2.7)$$

where B_E^M is the modified beam efficiency, F_{CR} is the antenna 1-dimensional pattern in cross range direction, $\langle ML \rangle$ is angles over main-lobe, $\langle ALL \rangle$ means angles over entire pattern.

2.4 Summary

In this chapter, we made a brief study on antenna systems for space-based SAR satellites. Different antenna system architectures were considered, and it is proposed a passive-array antenna architecture is suitable for small satellite mission. One challenge to realize this architecture is to realize a compact high-power RF source. Different antenna-panel technologies were also surveyed. The rectangular parallel-plate travelling-wave slot array antenna is found attractive due to its low-weight, compact pre-deployment packaging feasibility, low-loss at higher frequencies and space heritage.

We also studied the relationship between antenna characteristics and SAR image quality. A high antenna gain over the main-lobe and high beam-efficiency of the antenna patterns in range, cross-range direction is desired to improve the quality of SAR image.

Chapter 3

A Traveling Wave Dual Polarimetric Antenna for SAR

In Chapter.2, reason for choosing a passive-array centralized RF feed antenna system in small satellite SAR was outlined. Two key challenges were identified (Section.2.2), and this chapter addresses the first key challenge, which is the realization of a compact passive-array dual-polarization antenna, which shall be optimized for small satellite SAR.

The antenna panel technology was chosen to be a rectangular parallel-plate slot array, which falls within the category of traveling wave antennas. To perform optimization of the antenna panel design, a mathematical model of the phenomena is needed and some simplifications may be necessary. We divide the optimization process into two steps:

1. Optimal design of a single antenna panel.
2. Optimal design of excitation network of multiple antenna panels.

This breakdown in the design process is justified because of the way in which the antenna characteristics are related to SAR image characteristics (Section.2.3). The antenna pattern characteristics which need to be considered during the optimization process are the range pattern and cross-range pattern (Fig.2-8). The optimal design of the single antenna panel is carried out for purpose of achieving an optimal range

pattern. Later, the panel is fabricated and electrical characteristics measured. Using the measured characteristics in a mathematical model, we carry out optimal design of the array of multiple panels.

Section.3.1 introduces a mathematical model of a linear array of radiating elements for a traveling wave antenna. Section.3.2 surveys a number of antenna pattern synthesis algorithms and explains the selection of a multi-objective genetic algorithm as our algorithm of choice. Section.3.3 details the optimization procedure for design of a single panel. Section.3.4 applies the simulation results into a more accurate computer model of the antenna panel, and some adjustments are made to ensure acceptable electrical characteristics. Section.3.5 detail results of measurement of the fabricated antenna panel. In Section.3.6, the problem of optimal excitation synthesis of multiple panels is addressed, and a solution is proposed. Finally in Section.3.7 the results are summarized.

3.1 A Discrete Linear Array Model for Traveling Wave Antenna

There are established design principles for traveling wave antennas (uniform leaky wave, periodic leaky wave, waveguide slot-array antenna) given in [62] and [63]. In [64] the problem of finding an optimal aperture distribution for an array of cross-slots, begins by modeling the array of cross-slots as a continuous source distribution over the aperture. The model developed in [64] is identical with the design principle of uniform leaky wave antenna [62]. The resulting analytical expression of aperture distribution is later optimized by technique of calculus of variations.

The antenna of our interest has an array of slot-pairs spaced nearly one-free-space wavelength apart. Thus a model of discrete array of radiators is more appropriate than a model of continuous radiator source. The optimization solution found for a continuous source may not be the optimal when applied to a discrete source by sampling the continuous solution.

For the above reason, it is decided to pursue a discrete array model for the array of slot-pairs. In [63] [65][66, Chapter 8] a rectangular waveguide slot-array antenna is modeled as a transmission line with the slots represented by equivalent conductances. We use a similar model in terms of the 'coupling coefficients' as shown in Fig.3-1. The radiator element which leaks power to free-space is defined by its coupling coefficient (c_n): ratio of the power coupled to free-space (L_n) to the incident power at the radiator (P_n), $c_n = L_n/P_n$. P_{IN} is the input power to the array, P_{RES} is the residual power at end of array and d_n is the inter-element spacing between n^{th} radiator and $(n + 1)$ radiator where $n = 0, 1, \dots, N - 1$.

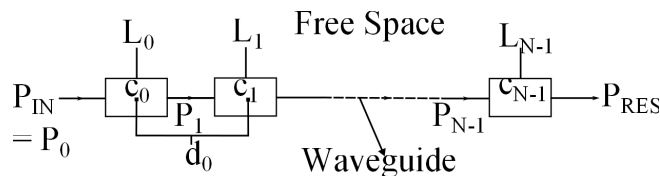


Figure 3-1: Model of traveling wave antenna with couplers

In reality, there shall be reflections from the individual radiators. However, in our simplified model, we ignore that phenomena. In the later part of design, the spacing between the radiators is changed so that the reflections from the adjacent radiators interfere destructively. Reflections from the individual radiators tend to add randomly, and because the radiators are lightly coupled, the array is essentially matched along its whole length [65, IV.B.]. Another simplification made is that the path loss of waveguide is negligible. In practice, there are conductive and dielectric losses associated with a traveling wave inside a waveguide.

Using the above model, we proceed to derive the relationship between set of coupling coefficients $\{c_n\}$, set of excitation coefficients $\{a_n\}$ and antenna far-field pattern characteristics such as peak gain G and beam efficiency B_E .

The leaked power at radiator n is proportional to the square of excitation amplitude $|a_n|$ at radiator n .

$$|a_n| = k\sqrt{L_n} \quad (3.1)$$

where k is a constant of proportionality.

We can express the excitations in terms of the coupling coefficient in an iterative manner as given in Table.3.1.

Table 3.1: Excitation of n^{th} radiator in terms of the coupling coefficient.

#	Waveguide Power	Leaked Power L_n	Magnitude of Element Excitation a_n
0	P_{IN}	$c_0 P_{IN}$	$k\sqrt{c_0 P_{IN}}$
1	$P_{IN} - c_0 P_{IN}$	$c_1(P_{IN} - c_0 P_{IN})$	$k\sqrt{c_1(P_{IN} - c_0 P_{IN})}$
.. so on	.. so on	.. so on	.. so on

The phase of excitation of each radiator depends upon the spacing between the radiators (d_n) and the wavelength in waveguide (λ_g). Let $\angle a_0 = 0$ rad.

$$\angle a_n = \angle a_{n-1} + \frac{2\pi d_{n-1}}{\lambda_g} \quad (3.2)$$

Total energy is conserved, hence:

$$\sum_{n=0}^{N-1} L_n + P_{RES} = P_{IN} \quad (3.3)$$

Let the configuration of the array of radiators be as shown in Fig. 3-2.

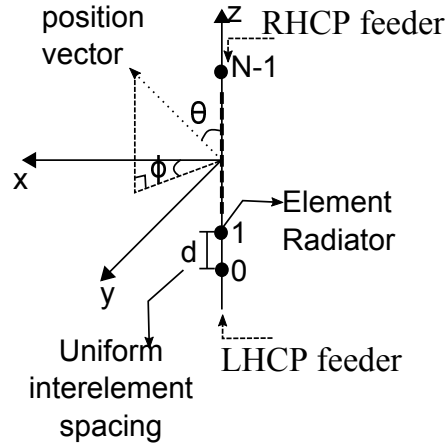


Figure 3-2: Linear array of radiators along z-axis

The far-field pattern on this linear array can be expressed in "pattern multiplica-

tion" [67] form as:

$$F(\theta, \phi) = F_{SE}(\theta, \phi)AF(\theta) \quad (3.4)$$

where, F_{SE} is the field pattern due to single radiator in the presence of all other radiators in array, $AF(\theta)$ is the array factor of the linear array.

$$AF(\theta) = \sum_{n=0}^{N-1} a_n \exp \frac{2\pi}{\lambda} (n-1)d \cos \theta$$

where, λ is free-space wavelength.

The total power radiated into free-space is:

$$P_{RAD} = k_P \int_{\phi=0}^{2\pi} \int_{\theta=0}^{\pi} |F(\theta, \phi)|^2 \sin \theta d\theta d\phi = \sum_{n=0}^{N-1} L_n \quad (3.5)$$

where k_P is a proportionality factor.

Residual power is:

$$P_{RES} = P_{IN} - P_{RAD} \quad (3.6)$$

We can write the antenna far-field gain as:

$$G(\theta, \phi) = \frac{\text{Power Radiated at } (\theta, \phi) \text{ per steradian}}{\text{Total Input Power}/4\pi} = \frac{4\pi k_P |F(\theta, \phi)|^2}{P_{IN}} \quad (3.7)$$

We define the 1-dimensional beam efficiency of the pattern in the YZ plane as the ratio of the total power radiated over main-lobe to the total power radiated in the YZ plane (see Eqn.2.6).

$$B_E = \frac{\int_{\theta=\theta^-}^{\theta^+} |F(\theta, \pi/2)|^2 d\theta}{\int_{\theta=0}^{\pi} |F(\theta, \pi/2)|^2 d\theta} \quad (3.8)$$

Pattern of Single Radiator

To determine the antenna pattern of the array of radiators, we need to know the pattern of radiator element, in our case the radiator element is slot-pair cut on an aluminum sheet with honeycomb spacing and fed with electromagnetic wave in Transverse Electromagnetic (TEM) mode. The properties of the individual radiators change when combined in an array as compared to their properties in an isolated state. They

"couple" to each other and the effects on array performance caused by this mutual coupling are significant and extensive [67]. The elemental pattern used in Equation.3.4 must also take into account the effects of mutual coupling.

[68] and [35] describe the synthesis of active phased array antenna pattern in TerraSAR-X using 40 cm long slotted waveguides sub-array as the radiator element. Each sub-array on the panel is considered as separate element and near-field measurements are made to get the "embedded sub-array pattern". This pattern is measured in the presence of other radiators on the panel and hence includes mutual coupling effects. This approach was feasible since they already had a fabricated antenna panel with sub-array radiators.

However, in a scenario when we are still in the design phase of the antenna panel, measured embedded radiator pattern is not available. It is possible to simulate a field pattern of an array element by making reasonable approximations. We consider the radiator element to be part of an infinite two-dimensional planar array. Although not a physically realistic configuration, the infinite-array model provides a reasonably good approximation to the performance of the interior elements of a large finite array [69, Chapter 9]. We build a unit cell with Periodic Boundary Conditions (PBCs) over the radiating element of interest as shown in Fig. 3-3. A "master-slave" relationship is defined between each of the PBC boundary pairs (M1/S1 and M2/S2). This entails enforcing a phase shift between the tangential electric fields appropriate to the desired array scan angle (scan-angle in our case is to the boresight). An absorbing boundary condition is applied to the top surface of unit cell. This structure is solved using commercial Finite Element Method (FEM) solver Ansoft High Frequency Structural Simulator (HFSS). Table. 3.2 lists important simulation parameters of the model. Fig. 3-4 shows the simulated directivity pattern of the slot-pair radiating element.

Such a technique has been applied before in modeling of phased array antennas. See [70] for description of using Ansoft HFSS for phased array modeling using unit cells and PBCs.

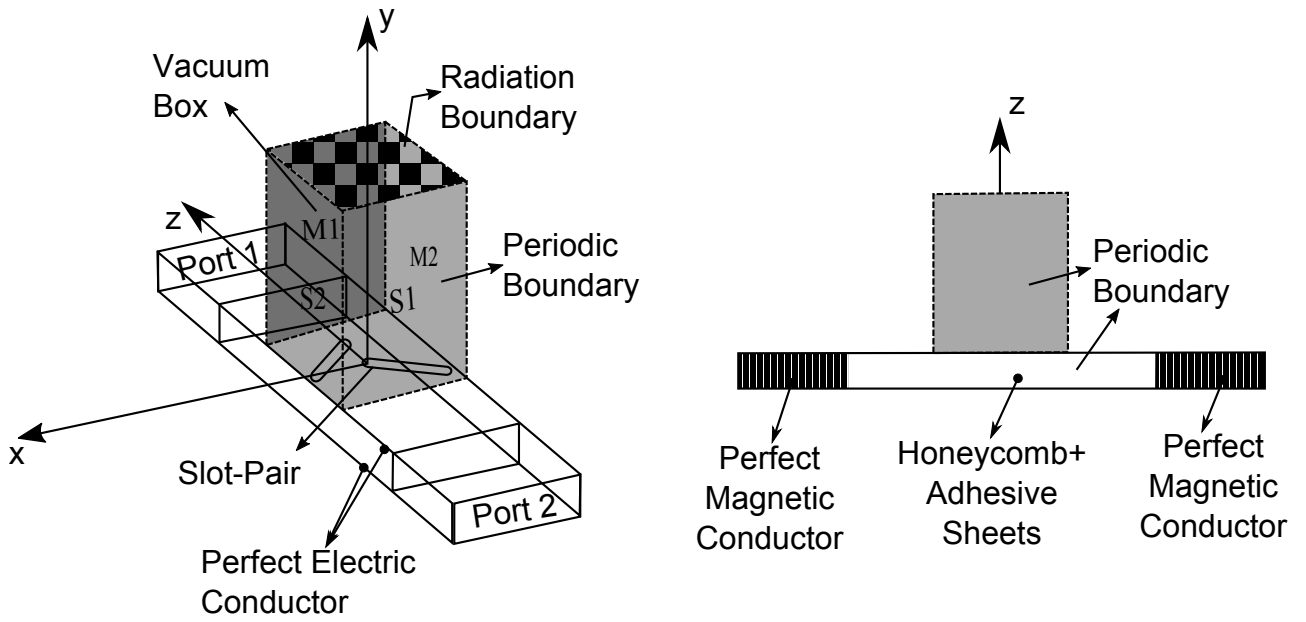


Figure 3-3: HFSS model of slot-pair

Table 3.2: HFSS slot-pair model parameters

Slot Length	13.3 mm
Adhesive thickness	0.09 mm
Adhesive permittivity	3.08
Honeycomb thickness	6 mm
Honeycomb permittivity	1.03
Simulated coupling coefficient	0.2255

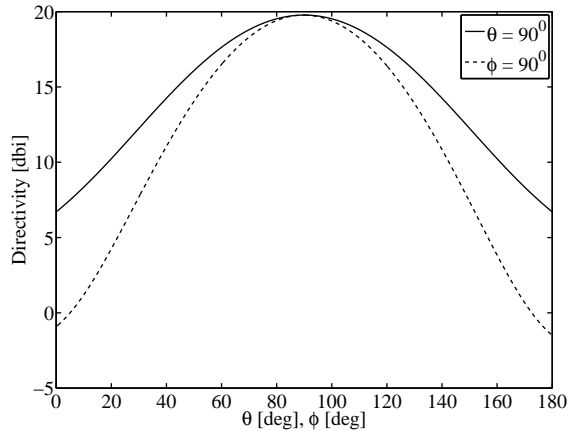


Figure 3-4: Relative power Pattern of single radiator.

3.2 Multi-objective Genetic Algorithm Optimization of Travelling Wave Linear Arrays

This section discusses various optimization algorithms available for optimizing antenna arrays and explains why we choose Non-dominated Sorting Genetic Algorithm-II (NSGA-II) as our optimization algorithm of choice.

3.2.1 Discussion on Classical Optimization Techniques used for Design of Antenna Pattern

A popular way to find an optimal antenna array is by use of antenna pattern synthesis techniques. A set of performance specifications (usually on the radiation pattern) are defined such as maximum sidelobe level of antenna, minimum peak gain, etc. The antenna variable is usually the excitation (amplitude and phase) of the array elements (in case of antenna made of discrete elements) or current distribution (in case of continuous antenna source), inter-element spacing in an array, geometrical configuration of the antenna. Some of the classic antenna synthesis algorithms are: placement of nulls in antenna pattern by treating the array-factor as a polynomial [71], use of z-transforms by treating the array synthesis problem as a linear sampled-data

systems problem [72][73], use of Tchebycheff polynomials for synthesizing patterns with the minimum possible side-lobe level for a given beamwidth (or vice-versa)[74], Fourier-transform method which yields an antenna beam pattern with minimum least square error from a desired pattern [44, Chapter 7], Taylor design to produce a pattern with decaying minor sidelobes [44, Chapter 7], non-uniform inter-element spacing to gain better performance [75] and many more.

The problem is the realization of the required excitations in antenna hardware may at times be difficult [76]. For example, in the discrete linear array model developed in Section.3.1 for a traveling wave antenna, we see that the normalized excitation amplitude of the radiators depends upon the coupling coefficient c of the current radiator and also of the previous radiators. Later on, we see (Section.3.3.3), for a dual-feed traveling wave antenna, the set of coupling distribution are restricted for the radiators which in turn restricts the set of excitation distribution, which can be achieved.

Another more general problem with the classical methods is that it may be necessary to modify the commonly used antenna pattern evaluation metrics or define another metric altogether as an optimization objective. For example, in case of traveling wave antennas, depending on the conductance of the radiators, there is residual power at the end of the antenna array. This residual power degrades the antenna gain, and has to be taken into account for a more sensible evaluation of antenna gain. The classical techniques, though mathematically elegant cannot be applied for general class of antenna pattern synthesis problems.

Moving away from classical antenna pattern synthesis methods to more general optimization algorithms, we see the most widely used optimization technique is solution by computing derivatives of the objective/ cost function. Methods that use derivatives converge to a local optimum solution near the starting point [77]. Depending on the objective/ cost function, there may or may not be a computable gradient.

The drawbacks in use of classical antenna pattern synthesis techniques and derivative-based optimization techniques have led to rise in use of metaheuristic algorithms

for optimization. Metaheuristics are general algorithmic frameworks, often nature-inspired, designed to solve complex optimization problems, and they are a growing research area since a few decades [78]. Examples of meta-heuristic optimization are genetic algorithm [79], particle-swarm [80] and simulated annealing [81]. The attractiveness of these algorithms is that they:

- Perform global-search [77]. They can 'escape' the local extrema, and search the entire terrain for a better extremum.
- Are simple to implement.
- Have been successfully applied to a broad class of problems.
- Can be solved using parallel computational machines [77] against other traditional algorithms which implement a sequential process.

Perhaps a 'draw-back' of metaheuristic algorithms is that they do not guarantee the obtained solution is the most optimal. That is, their purpose is to seek and find good solutions for the problem, rather than a guaranteed optimal solution [82]. In problems where the maxima/ minima of the objective function is not known a priori, this will be a problem.

3.2.2 Examples of Metaheuristic Optimization applied to case of Antennas

There are many published works on successful application of metaheuristic algorithms for antenna optimization. To illustrate the power of these algorithms over traditional algorithms, we survey numerous cases.

[83] used genetic algorithm to get optimal (low side-lobe level) phase tapering over the antenna array for different beam-steering angles. Digital phase shifters used in antenna arrays have limited precision (number of bits), and classical approach yields solutions with infinite precision. When applying genetic algorithm, the limited precision can be taken into account by simply using species(trial solutions of a population) of binary format.

[84] used particle-swarm algorithm for finding an optimal linear array geometry which suppresses sidelobe level and also places nulls at desired directions. This was achieved by defining a new objective function [84] given in Equation.3.9.

$$Fitness = \sum_i \frac{1}{\Delta\phi_i} \int_{\phi_{li}}^{\phi_{ui}} |AF(\phi)|^2 d\phi + \sum_k |AF(\phi_k)|^2 \quad (3.9)$$

where $[\phi_{li}, \phi_{ui}]$ s are the spatial regions in which sidelobe level is suppressed, $\Delta\phi_i = \phi_{ui} - \phi_{li}$, and ϕ_k s are directions of the nulls, $AF(\phi)$ is the array factor.

[85] compares performance of genetic and particle-swarm algorithms for finding optimal complex excitations for a linear phased array of 100 elements. The cost measure to be minimized is the sum of the squares of the excess far field magnitude above the specified sidelobe envelope. This penalizes sidelobes above the envelope, while neither penalty nor reward is given for sidelobes below the specification.

[86] uses simulated annealing to find an optimal linear array geometry and amplitude excitation to reduce peak sidelobe level. This illustrates the case when we have a large number of optimization variables and hence using metaheuristic methods, we can utilize all available degrees of freedom.

[87] has a comprehensive description of application of genetic algorithms in electromagnetics, with [87, Chapter 4] dedicated to optimizing antenna arrays.

In [88] the author uses particle-swarm optimization to synthesize optimal azimuthal beam pattern. Different objectives such as improving azimuthal ambiguity ratio, σ_{NEZ0} , radiometric accuracy and azimuthal resolutions are clubbed together in form of "antenna mask template". An single objective function is defined, which minimizes the error between design antenna pattern and current beam pattern.

3.2.3 From Single-Objective to Multi-Objective Optimization

Real-world optimization problems have often more than one objective, and in most cases, there is trade off between them. For example, while synthesizing an antenna pattern with low sidelobes, minimizing the sidelobe level results in larger main beamwidth. It is not possible to synthesize an antenna pattern with narrow main

beamwidth and low sidelobes at the same time (aperture area of antenna is fixed). This calls for the need of multi-objective optimization techniques.

Traditional Multi-Objective Optimization Techniques

In this subsection, four widely used traditional multi-objective techniques are briefly discussed. Consider optimization problem of M individual objective functions $f_1(\mathbf{x}), \dots, f_M(\mathbf{x})$. \mathbf{x} is the vector of optimization parameters in the feasible region.

1. *Weighted-sum technique*

In this technique, a single objective function is formed, which is a weighted sum of different individual objective functions.

$$F = \sum_{i=1}^M w_i f_i(\mathbf{x})$$

F is the final single-objective function and w_i are the weights for the objective functions. The weights are set depending on the degree of trade-off we would like to make between the objectives. In practice, it can be very difficult to precisely and accurately select the weights w_i , even for someone familiar with the problem domain [89]. Scaling among the objectives is needed, and small perturbations in these weights can lead to quite different solutions [89]. Some of the examples given in Section.3.2.2 used this method to define a single objective function.

2. *Method of distance functions* [90]

This is similar to the weighted-sum technique. A demand-level vector $\bar{\mathbf{y}}$ is specified, which is the 'goal' of the optimizer. The problem is formulated as follows:

$$Z = \left[\sum_{i=1}^M |f_i(\mathbf{x}) - \bar{y}_i|^r \right]^{1/r}, \quad 1 \leq r < \infty$$

3. *Constraint technique*

Another traditional approach is to move all but one objective to the constraint set. For a minimization problem; it is formulated as follows:

$$\text{minimize } f_1(\mathbf{x}), \text{ subject to } f_i(\mathbf{x}) < V_i, \quad i = 2 \text{ to } M$$

where, V_i is the maximum constrained value of function $f_i(\mathbf{x})$. Again, like in the setting the weights, it is difficult to set the constraining value V_i [89].

4. *Min-max formulation* [90]

This method attempts to minimize the deviations of the single-objective function from the individual optimum. It is formulated as follows:

$$\text{minimize } F(\mathbf{x}) = \max[Z_j(\mathbf{x})], \quad \mathbf{j} = \mathbf{1}, \mathbf{2}, \dots, \mathbf{M}$$

$Z_j(\mathbf{x})$ is calculated for non-negative target optimal value $\bar{f}_j > 0$ as follows:

$$Z_j(\mathbf{x}) = \frac{f_j - \bar{f}_j}{f_j}, \quad j = 1, 2, \dots, M$$

Priority of each objective can be varied by introducing dimensionless weights in the formulation. Again, setting the weights to trade off the priority is difficult.

Pareto Multi-Objective Optimization using Non-Dominated Sorting Genetic Algorithm-II (NSGA-II)

Moving away from the traditional method of multi-objective optimization is another approach, which determines the entire set of *Pareto* solutions. In the absence of any further information, one of the Pareto-optimal solutions cannot be said to be better than the other [91]. This property is also termed as *non-domination*. A Pareto-optimal set (also called Pareto-curve or Pareto-front) will contain solutions, which are non-dominated with respect to each other. As an example, consider a decision-making problem involved in buying a diamond. Say we make a survey of diamond producers over the world and on a graph plot out the available options in terms of

diamond purity and cost as shown in Fig.3-5.

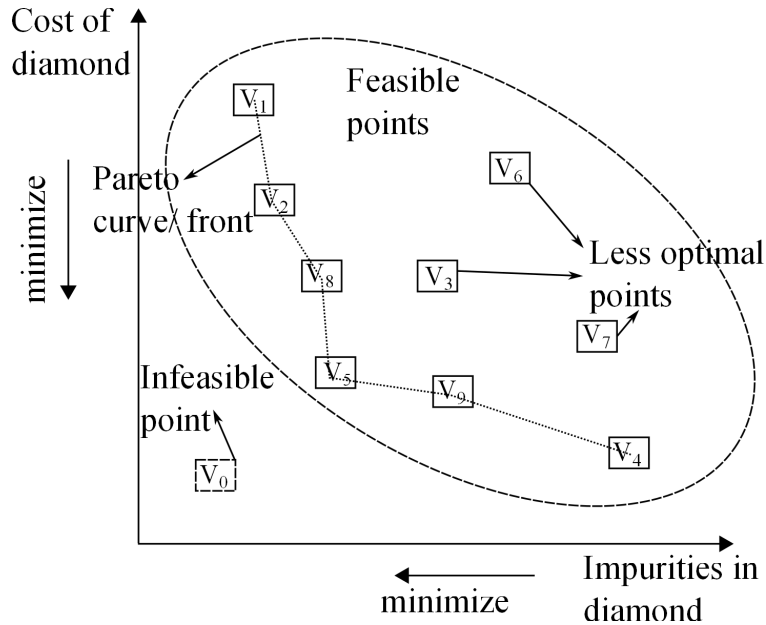


Figure 3-5: Illustration of Pareto-curve

Ideally, we would like to purchase a diamond, which has least impurities and minimal cost. We see from the Fig.3-5, there are a number of solutions (vendors) to choose from, $V_1, V_2, V_8, V_5, V_9, V_4$. All these solutions are non-dominated. As an example if we compare vendor V_2 to vendor V_9 , although the cost of diamond from vendor V_9 is lower, it has higher impurities compared to diamond from vendor V_2 . On another hand if we compare diamond from vendor V_8 and vendor V_3 though they both offer diamonds at same cost, the diamonds from vendor V_8 are purer. Thus V_8 *dominates* V_3 . A vendor such as V_0 cannot exist in the real world (assuming free-markets) and is thus an in-feasible solution.

Not all problems may have a convex Pareto front. Depending on the objectives, region of operation and constraints, the shape of the Pareto front can have different shapes and discontinuities. See [91] for example test problems. An added advantage in finding the Pareto front is, we can determine the relationship between the objectives.

There is a number of Pareto multi-objective optimization meta-heuristic algorithms. Among them, Genetic Algorithm (GA) has been the most popular heuristic

approach to multi-objective design and optimization problems [89]. The survey by [82] in the year 2002 indicated that 70% of the articles surveyed utilized genetic algorithms as their primary meta-heuristic technique for solving multi-objective problems. [89, Table 1] gives a list of well known multi-objective GA including their advantages and disadvantages. Among them, NSGA-II [91] is a well tested and efficient method. For these reasons, we choose NSGA-II as our primary optimization technique.

3.3 Synthesis of Optimal Aperture Field Distribution over an Antenna Panel

In this section, we discuss the synthesis of an optimal aperture field distribution over a single antenna panel. The aperture field will be optimized in the sense, that the far-field antenna pattern it produces, enhances the quality of SAR images.

3.3.1 Mathematical Model of Antenna Panel

To proceed, we first need a mathematical model of the antenna which forms a basis for the optimization. Recap from Fig.2-6 the structure of the antenna panel. Optimizing the antenna panel directly (for example, using a computer simulator to solve for Maxwell's equations over the antenna structure) is computationally heavy, especially if we run a meta-heuristic algorithm such as NSGA-II which requires many iterations to converge. Instead, we consider a simple model of the antenna panel, as a 2-dimensional array of slot-pairs as shown in Fig.3-6a. Total number of slot-pairs are $N \times M$. By changing the length of slots in the slot-pairs (for a given slot-pair; the two slots have same length), we can control the leaked power and hence the coupling coefficient as defined in Section.3.1. We have thus NM degrees of freedom to synthesize the aperture field. Though the simple model can easily process the 2-dimensional array model of the antenna panel, the next stage of design, which is to simulate and optimize in computer will be very laborious if we have NM different slot-pairs. Simulation in computer is discussed in Section.3.4 and is required to vary

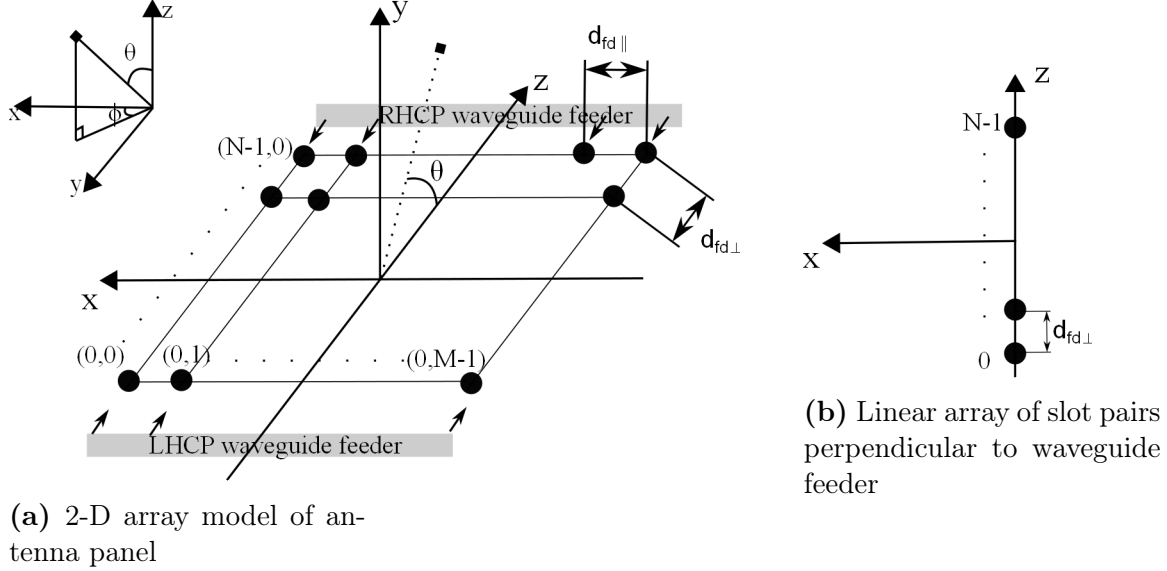


Figure 3-6: Array model of antenna

the inter-element spacing of the slot-pairs to minimize reflections.

To simplify the computer modeling task, we shall make a simplification for our design. We shall force the slot-pairs along the x-axis (see Fig.3-6a), i.e. along the waveguide feeder to be identical. In doing so we reduce our available degree of freedom from NM to only N . The trade-off is that we greatly simplify the design process in the later stage of antenna panel development. Further, we assume uniform interelement spacing $d_{fd\parallel}$ parallel to waveguide feeder.

Now our problem is to decide appropriate coupling coefficients (and thus slot-lengths) for the linear array of slot-pairs perpendicular to the waveguide feeder (Fig.3-6b). We can use the discrete linear-array model of traveling wave antenna developed in Section.3.1 to model this traveling wave linear array.

3.3.2 Optimization Objectives

In 2.3, we discussed the relationship between SAR performance and antenna pattern characteristics. Recall that the SAR performance characteristics of interest are SNR_{image} , range ambiguity and azimuthal ambiguity. The excitations and configuration of the linear-array of slot-pairs perpendicular to the waveguide-feeders are responsible for shape of the SAR range-plane antenna pattern (see Fig.2-10). Keep-

ing this in mind, we define the optimization objectives as follows:

1. Maximize the peak gain of the linear-array antenna pattern $G(\pi/2, \pi/2)$ (see Eqn.3.7) and hence improve SNR_{image} .
2. Maximize beam-efficiency of linear-array B_E (see Eqn.3.8) and hence improve range ambiguity performance.
3. Minimize residual power P_{RES} (see Eqn.3.6) so that transmitted power to the orthogonal polarization receiver is minimized.

Objective 3 is originally in form of a constraint, i.e. there is a requirement on the antenna hardware that the transmitted power from RHCP feeder to LHCP feeder or vice-versa, should be less than -20 dB. Instead of modeling this as a constraint in our optimization problem, we instead define it in form of a minimization objective. Note that while objectives 1,2 relate to the SAR performance, objective 3 arises due to the type of antenna we are using, i.e. dual-feed traveling wave antenna.

3.3.3 Optimization Constraint and Variables

A requirement on the synthesized RHCP and LHCP beam pattern is that they should be identical about the main-beam. This means the synthesized excitation should be identical for RHCP feed and LHCP feed. This is possible if the coupling distribution is symmetric [64] about the center of array. Symmetrical coupling distribution means traveling waves see identical disturbances irrespective of direction of feeding, and thus synthesized excitation is identical (but flipped about the center of array). Additionally, the spacing between the individual radiation in the linear array should allow for uniform phase excitation, so both the RHCP and LHCP beams point at same direction (bore-sight). It is easy to see that a uniform amplitude excitation is not achievable in case of dual-polarization, since the coupling distribution for uniform amplitude excitation is not symmetric.

Instead of specifying this requirement as a constraint in optimization, we instead implement this constraint by specifying the first $N/2$ coupling coefficients as the

optimization variables. The remaining of $N/2$ coupling coefficients are decided by the symmetry requirement on the coupling distribution.

3.3.4 Optimization Parameters

Table 3.3: Optimization parameters

Number of radiators in array (N)	24
Inter-element spacing ($d_{fd\perp}$)	$0.9\lambda_0$ which corresponds to approximately uniform phase excitation of all array elements ^a
Main lobe beamwidth	2 deg, corresponding to swath-width of 22.5 to 42 km at 600 km altitude, nadir-angle variation from 15 deg to 45 deg
Optimization variables	Set of coupling coefficients of the first $N/2$ radiators. The remaining coupling coefficients of the last $N/2$ radiators is fixed by the symmetric constraint
NSGA-II Parameters	
Population Size	500
Number of generations	504
Probability of cross-over	0.9
Probability of mutation	1/12
Distribution index for crossover	15
Distribution index for mutation	20

^aNominal value is λ_g . The value $0.9\lambda_0$ is found after trial and error during development of single-polarization parallel plate slot array antenna [51]

3.3.5 Optimization Results

Before we lay out the results, it is useful to have a solution with which we can compare it with. Sakakibara[64] carried out determination of an optimal coupling distribution for a dual-polarization (dual-feed) cross-slotted waveguide array antenna panel. The waveguide array is modeled as a continuous source distribution and used technique

of calculus of variations to find field-coupling distribution $\alpha(z)$ as a function of the residual power t , which maximizes the antenna peak gain. The major differences from the approach of Sakakibara and our approach are detailed in Table.3.4.

Table 3.4: Sakakibara approach vs Our approach

Sakakibara approach	Our approach
Array of slots is modeled as continuous line source.	Array of slots is modeled as linear array of discrete radiators, with each radiator having elemental pattern as that of the slot.
Single objective optimization problem. Find coupling distribution (as a function of residual power) to which maximizes peak gain. However, since the residual power is a variable, we can generate a Pareto curve of optimization of two objectives: maximize peak gain, minimize residual power.	Three objective optimization problem. Objectives are as defined in 3.3.2.
Calculus of Variations optimization.	Multi-objective genetic algorithm optimization.

Since Sakakibara’s optimization result is a continuous coupling function $\alpha(z)$, we perform the comparison by first discretizing the coupling function. This is justifiable since for the next step in antenna panel design, we need to start design in HFSS using a discrete set of coupling coefficients. The coupling coefficient is obtained by integrating the coupling per unit length $\alpha(z)$ over inter-element spacing.

$$c = \int_{-d_{fd\perp}/2}^{d_{fd\perp}/2} 2 * \alpha(z) dz \quad (3.10)$$

Pareto Curves

Fig.3-7 show resulting Pareto plots from NSGA-II and Sakakibara optimization. Note that In case of Sakakibara, the optimization objective to maximize beam-efficiency is absent.

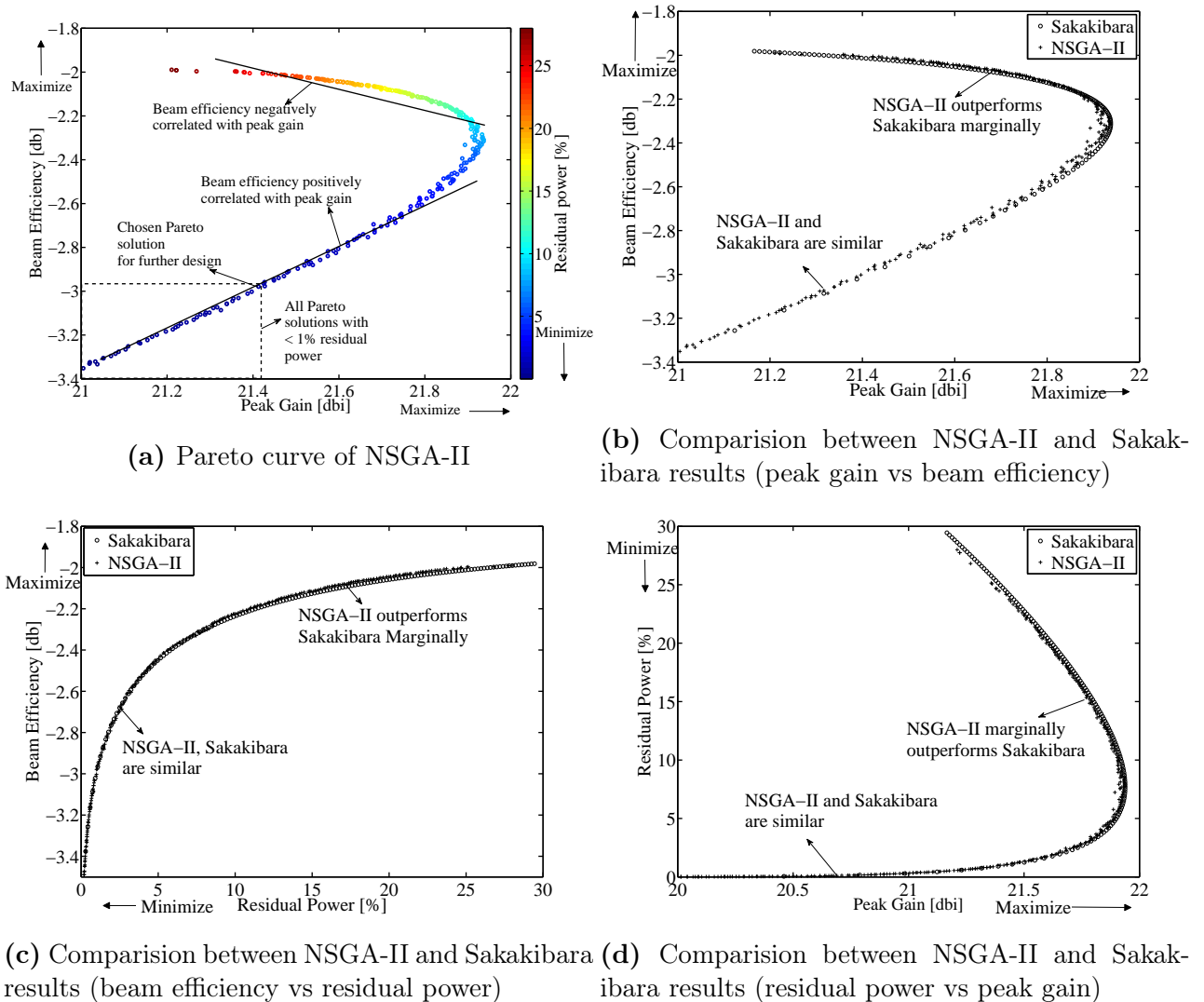


Figure 3-7: Pareto curves and comparison of results from NSGA-II and Sakakibara

Following important observations is made from the Pareto curves:

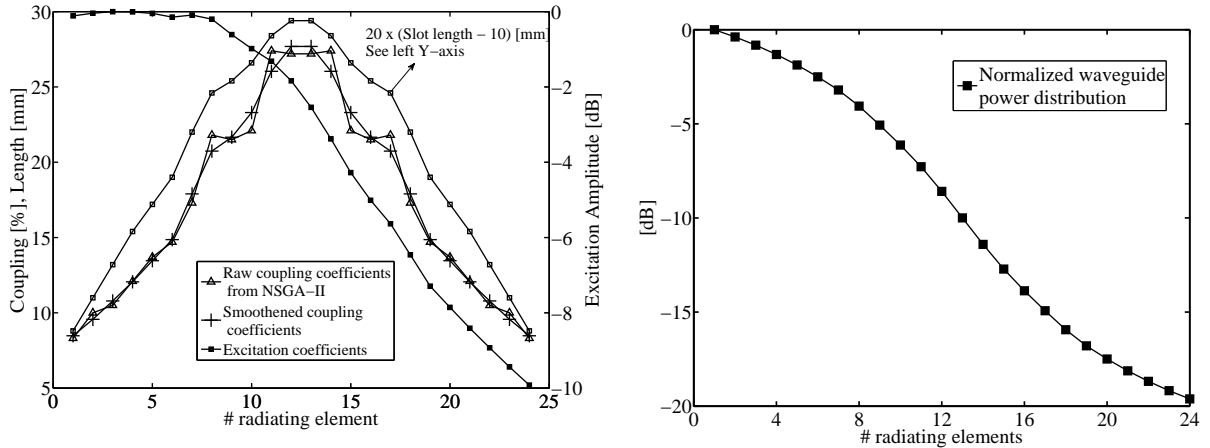
- There is a positive correlation between beam-efficiency and peak-gain in case of low residual power, while the correlation becomes negative when the residual power increases.

- The Pareto curve from NSGA-II and Sakakibara matches in the region of positive correlation of beam-efficiency vs peak-gain. The Pareto curve of NSGA-II performs marginally better in case when there is negative correlation between beam-efficiency and peak-gain. This can be expected since Sakakibara optimization does not have beam-efficiency as one of its optimization objectives.

This comparison with Sakakibara optimization method validates our discrete array traveling antenna model and use of multi-objective genetic algorithm NSGA-II to perform optimization. The advantage of our approach of using the meta-heuristic optimization algorithm is that we can have almost any kind of objective function, without having to worry about its continuity or having to solve using advanced calculus methods (if indeed it can be solved).

Description of chosen Pareto Point for Design

As stated before in Section.3.3.2, the objective to minimize residual power is really meant to be a constraint. In Fig.3-7a all the Pareto solution in the dashed box has residual power less than -20 dB. Thus only these solutions are of interest to us. Fortunately, there is a positive correlation between peak-gain and beam-efficiency in this region. accordingly we can choose a Pareto solution which corresponds to the maximum peak-gain (21.42 dBi) and maximum beam-efficiency (-2.98 dB) corresponding to the top-right corner of the dashed box in Fig.3-7a.



(a) Coupling and Excitation coefficients of the chosen Pareto solution. Note that the coupling distribution have been 'smoothened'. (b) Normalized waveguide Power distribution of the chosen Pareto solution.

Figure 3-8: Implemented Pareto solution

3.4 Computer Model and Simulation

A 3D structural model is built using Ansys electromagnetic simulator software called HFSS [92]. As mentioned in Section.2.2.1, previous to the dual polarization rectangular plate slot-pair array antenna panel, a single polarization rectangular plate slot-pair array antenna was designed, fabricated and tested. The dual-polarization antenna panel has a similar structure except for the additional LHCP waveguide feeder and different slot-pair lengths, configuration. This part of the work is done primarily by my colleague Dr. Prilando Akbar. Details may be referred in [55] [51]. For the sake of continuity of this dissertation, I present a brief summary below.

Using the set of optimal coupling coefficients (Section 3.3.5), first a linear array of radiating slot-pairs is built as shown in Fig.3-9a. The honeycomb dielectric is modeled as uniform volume with permittivity determined experimentally and thickness as specified by the manufacturer [56]. Two adhesive sheets are modeled also as uniform volume with permittivity and thickness as specified by the adhesive sheet manufacturer [57]. Periodic boundary condition is applied at side walls of the linear array to enable TEM wave propagation. The slot length is varied to match with the set

of design coupling coefficients. Inter slot-pair spacing is adjusted to obtain uniform E-field phase distribution at 9.65 GHz (the design center frequency). The HFSS radiating linear array model shows uniform aperture phase distribution and aperture amplitude distribution according to the original NSGA-II design (at 9.65 GHz)(see Fig.3-13).

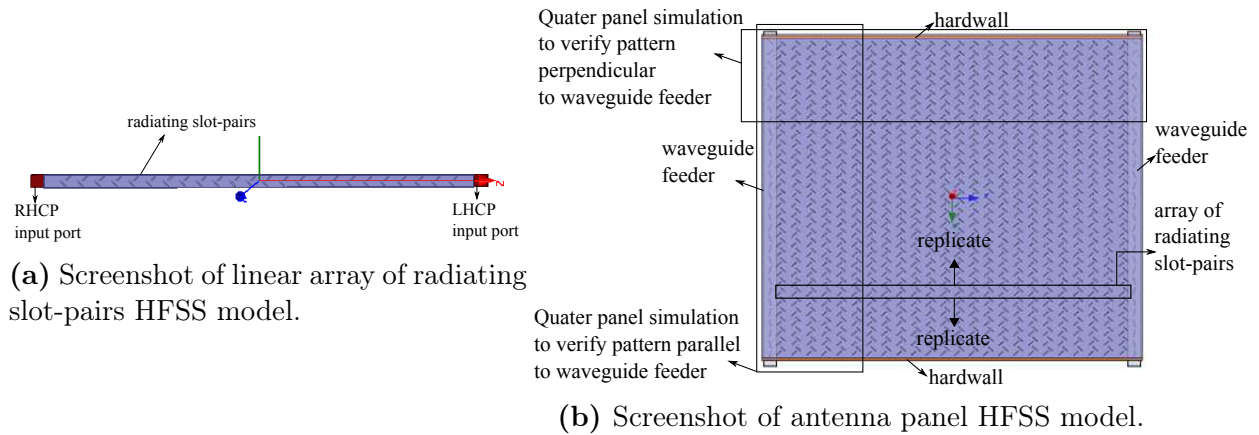


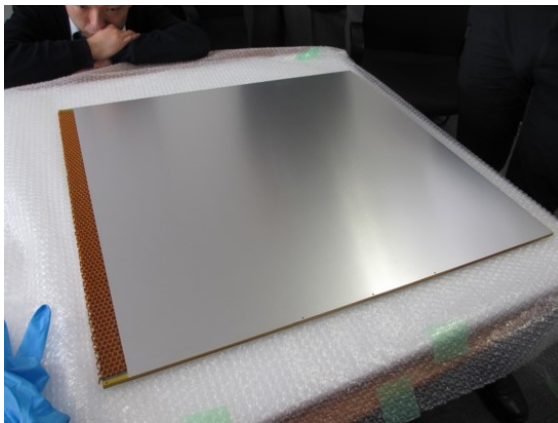
Figure 3-9: HFSS modeling

The waveguide feeder model used for the design of single-polarization uniform aperture excitation antenna panel is also used for the current dual-polarization antenna panel design, since the aperture excitation synthesis along the waveguide feeder is identical for the both the antenna panels. To build the complete antenna panel model, the linear array of radiating slot-pairs is replicated in the direction of the waveguide feeder as shown in Fig.3-9b.

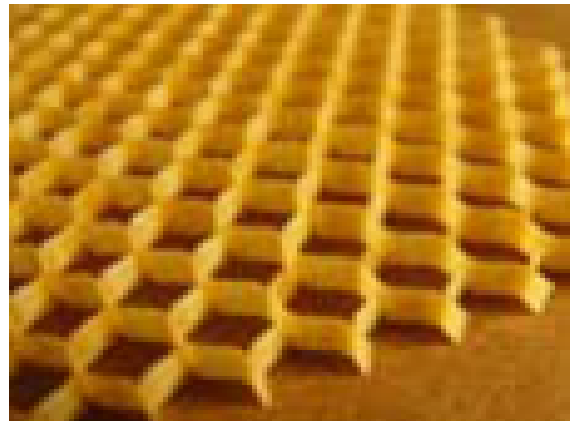
Simulation of the complete antenna panel is computationally intensive and time consuming. Hence we simulated two quarter panel structures to verify the antenna pattern in planes along the waveguide feeder and perpendicular to the waveguide feeder (see Fig.3-9b).

3.5 Test Results of Fabricated Antenna Panel Prototype

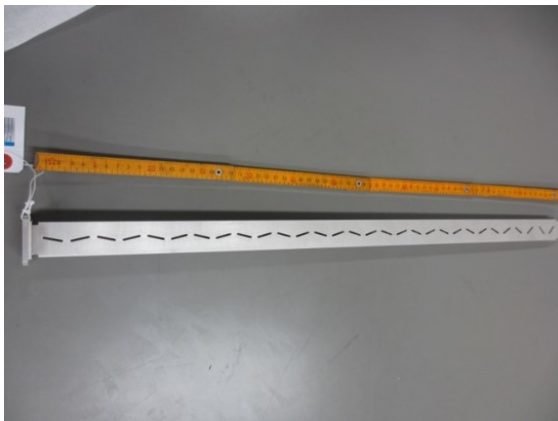
The designed antenna panel was fabricated. The outer dimensions of the fabricated antenna are shown in Fig.2-6. The radiating and feeder slot dimensions are those simulated in HFSS for design frequency of 9.65 GHz. Fig.3-10 shows photographs of antenna panel and its components.



(a) Back plate of antenna panel: Aluminum skin



(b) Nomex honeycomb sheet. This sheet is attached to the panel aluminum skins with adhesive.



(c) Rectangular slotted waveguide feeder



(d) Fabricated antenna panel. The radiating slot-pair can be seen cut on the front aluminum skin.

Figure 3-10: Photographs of the antenna panel and its components.

Three different measurements were carried out to test the electrical characteristics of the antenna panel. For all the measurements consider the coordinate system as shown in Fig.3-11.

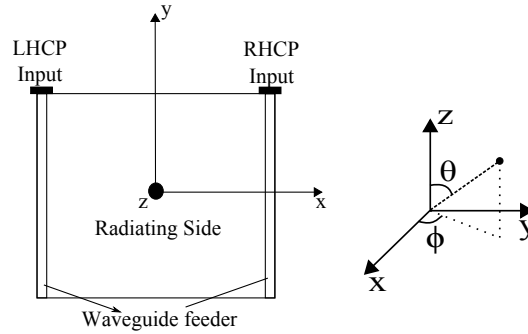


Figure 3-11: Coordinate system of antenna panel tests. The antenna panel is in XY plane, with its geometrical center at the origin. The radiating surface normal vector is towards +z direction.

3.5.1 Near Field Measurements

Near-field measurements are carried out to measure electric field amplitude, phase in near field region of the antenna panel. A photograph of the setup in an anechoic chamber is shown in Fig.3-12. This is a standard planar near field measurement setup [44, Chapter 17]. An open-ended rectangular waveguide is used as a receiver probe. The Antenna Under Test (AUT) is excited at either the RHCP or LHCP port by sinusoidal monotone signal in the frequency band of interest. The probe is placed about $4\lambda_0$ from the panel surface, where λ_0 is the wave-length in free-space. The probe is moved over a planar surface (relative to the antenna panel), and it takes measurements at spacing $\Delta x = \Delta y = 1.5cm$ over 75×75 points in arectangular grid. This satisfies Nyquist's criterion of maximum allowable sampling distance at the highest frequency of interest (9.85 GHz) [44, Balanis]. Measurements are made at different frequencies within the bandwidth of interest. A second run of the measurement is performed, this time keeping the receiver probe at orthogonal polarization. Probe compensation is performed to take into account the directive pattern of the open-ended rectangular waveguide. The circular polarization component is calculated from the measured pair of orthogonal components. Fourier transform is applied on the near-field data to compute the far zone electric field.

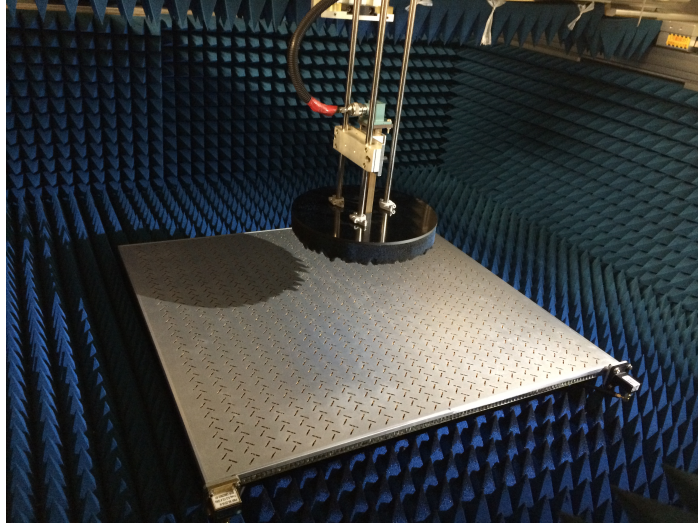
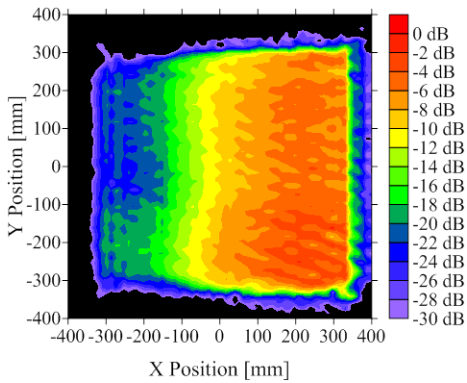
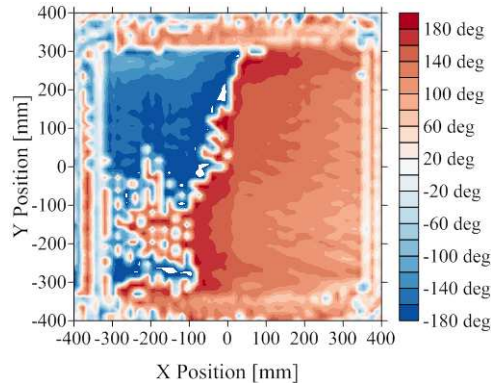


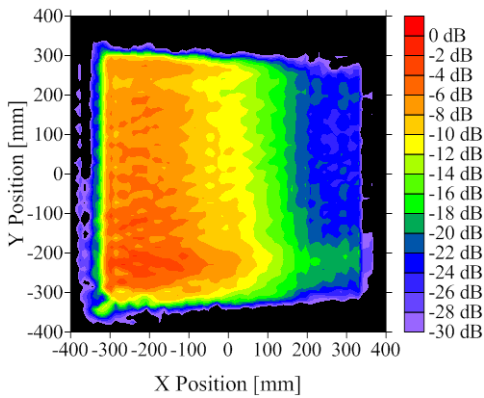
Figure 3-12: Near field test setup in Tokyo Institute of Technology (TIT)



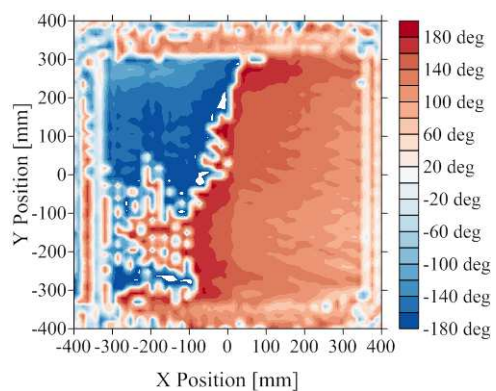
(a) RHCP near zone electric field amplitude distribution.



(b) RHCP near zone electric field phase distribution.



(c) LHCP near zone electric field amplitude distribution.

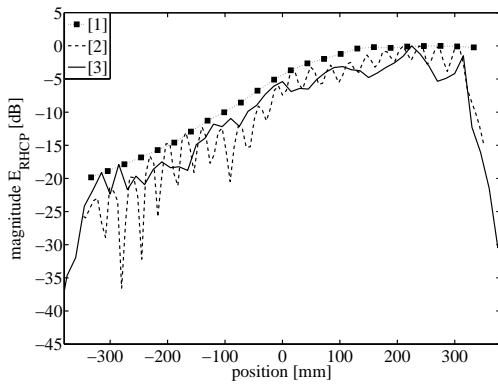


(d) LHCP near zone electric field phase distribution.

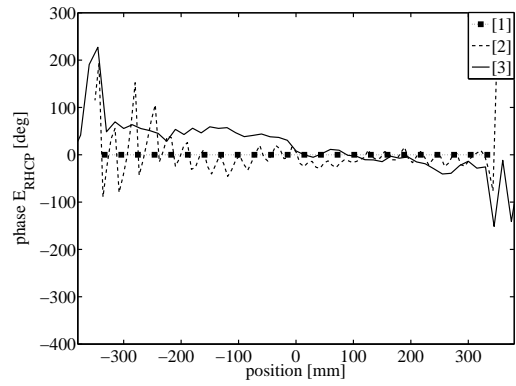
Figure 3-13: Near field electric field amplitude and phase distribution at 9.65 GHz

Fig.3-13 shows the 2-dimensional measured electric field amplitude and phase distribution over the antenna panel for RHCP and LHCP polarizations at 9.65 GHz. A linear phase taper is observed in direction perpendicular to the waveguide feeder. This becomes more apparent in Fig.3-14 where a comparison is drawn for three cases:

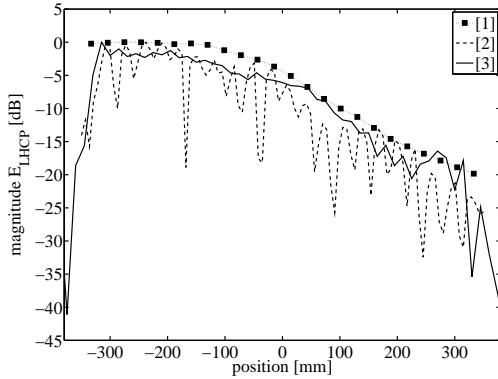
- [1] Design field excitation coefficients of dual-feed linear array of point radiators.
- [2] Simulated near field distribution of linear array of slot-pairs designed in HFSS.
- [3] Near field measurements of the antenna panel along line $y = 0$.



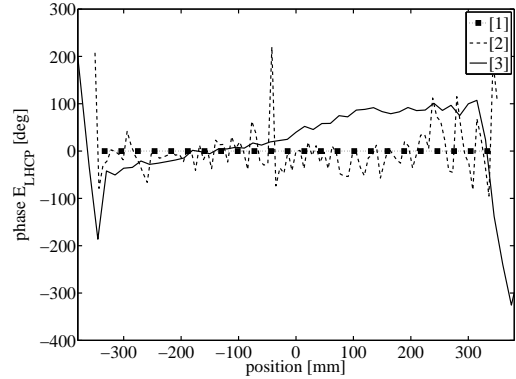
(a) RHCP waveguide feeder is excited.



(b) RHCP waveguide feeder is excited.



(c) LHCP waveguide feeder is excited.



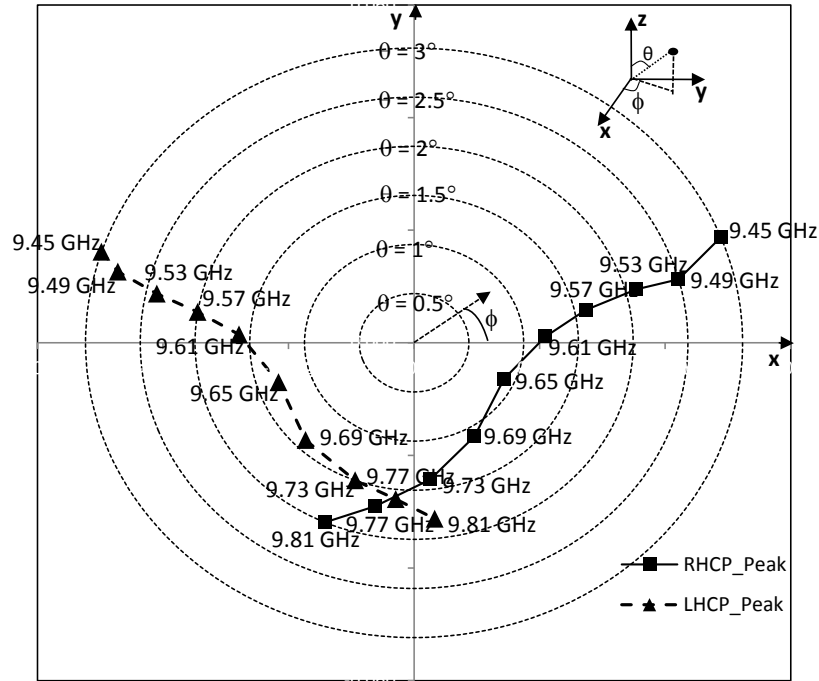
(d) LHCP waveguide feeder is excited.

Figure 3-14: RHCP and LHCP electric field amplitude and phase distribution at 9.65 GHz. [1] Design field excitation coefficients of dual-feed linear array of point radiators. [2] Simulated near field distribution of the linear array of slot-pairs designed in HFSS. [3] Near field measurements of the antenna panel along line $y = 0$.

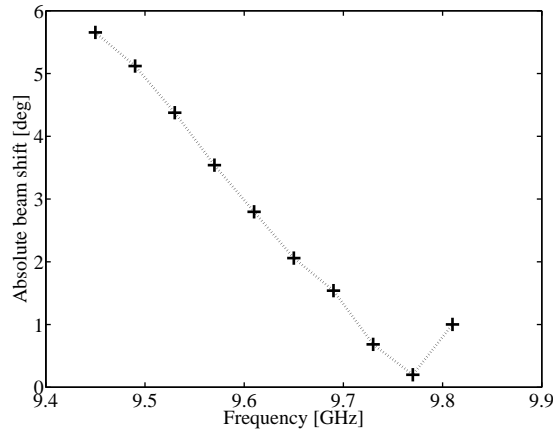
Looking at Fig.3-14, we see that the field amplitude distribution of the design, HFSS simulations and panel measurements closely matches. However, the measured phase

distribution of antenna panel shows a non-zero linear slope at 9.65 GHz. The original design and HFSS design was carried out to have uniform phase distribution at 9.65 GHz. Since the direction of feeding in the traveling wave antenna for RHCP, LHCP configuration is opposite, the linear phase tapers shows positive and negative slope accordingly (see Fig.3-14). The linear phase taper leads to beam shift about the panel normal vector and the RHCP, LHCP main beam tilt in opposite directions.

Fig.3-15a shows a projected sphere plot of the position of peaks at different frequencies of the RHCP and LHCP beams. Fig.3-15b shows the absolute beam shift between the RHCP LHCP peaks as a function of frequency. The RHCP LHCP peaks coincide closely at 9.77 GHz, against the designed 9.65 GHz. This deviation from our design is attributed to incorrect modeling of the honeycomb sheet and adhesive layer modeling in HFSS. The excitation phase distribution in traveling wave antenna is dependent on the wavelength in the waveguide. Inaccurate modeling of the waveguide inner dielectric leads to erroneous phase excitation simulation.



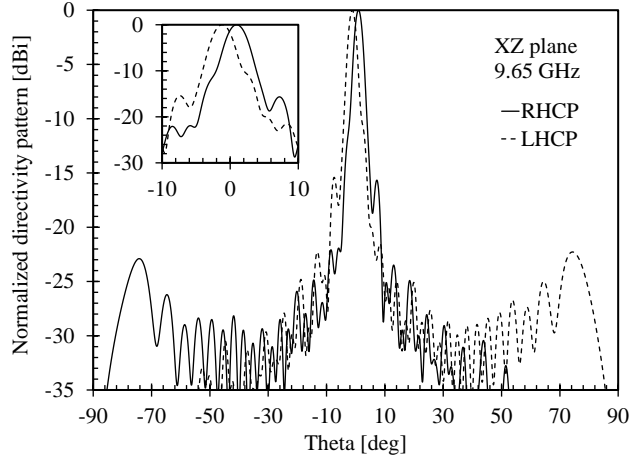
(a) Projected location of peaks at different frequencies. The RHCP and LHCP beams coincide around 9.77 GHz.



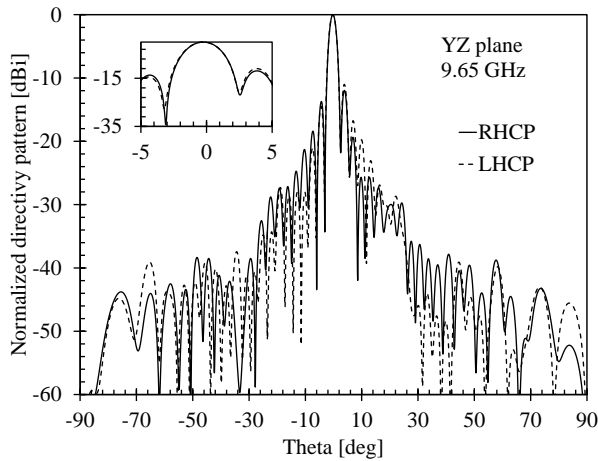
(b) Beam shift between RHCP, LHCP beams

Figure 3-15: Frequency dependence of antenna directivity (RHCP and LHCP).

Fig.3-16 shows the normalized directivity pattern (at 9.65 GHz) in the planes perpendicular to the waveguide feeder (XZ plane) and along the waveguide feeder (YZ plane). The beam shift between the RHCP and LHCP beams is 2.1 deg. Large sidelobes are observed in case of XZ pattern. This is because the slot-pair spacing is near $1\lambda_0$, which leads to grating lobes in the array factor term.



(a)



(b)

Figure 3-16: RHCP and LHCP far-field normalized directivity patterns (at 9.65 GHz) in the XZ plane and YZ plane. Note that the RHCP pattern corresponds to excitation of the RHCP feeder, and LHCP pattern corresponds to excitation of LHCP feeder.

It is worthwhile to see the range-ambiguity performance of the measured pattern in range direction (see Fig.3-17). The *IRASR* (Eqn.2.2) was simulated assuming a flat Earth model as a function of the look angle γ and f_P . The performance degrades as we move towards higher f_P and higher γ . Operation at lower f_P allows imaging over a wide range of γ with acceptable *IRASR* (< 20 dB). This can be made possible using up/down chirp in transmitting waveform, hence effectively halving the f_P to be considered in range-ambiguity calculations [59].

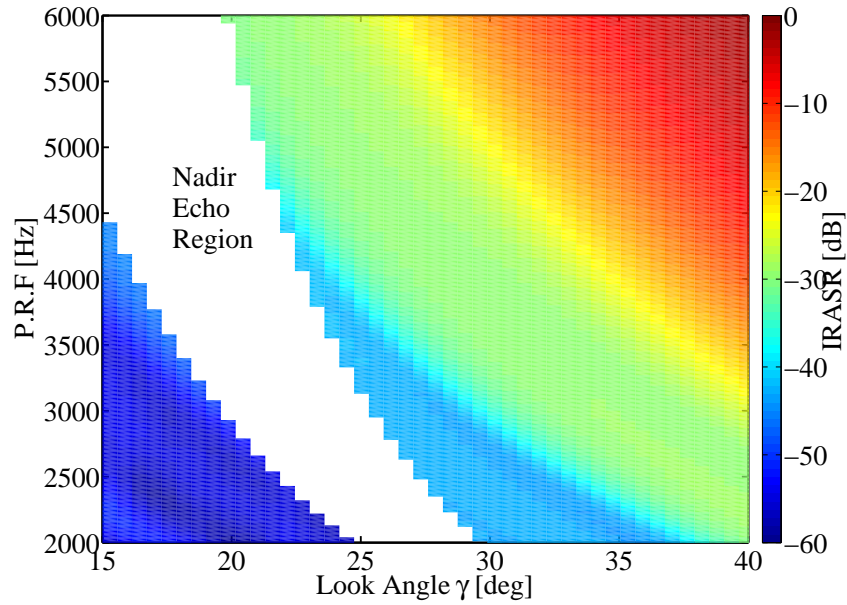
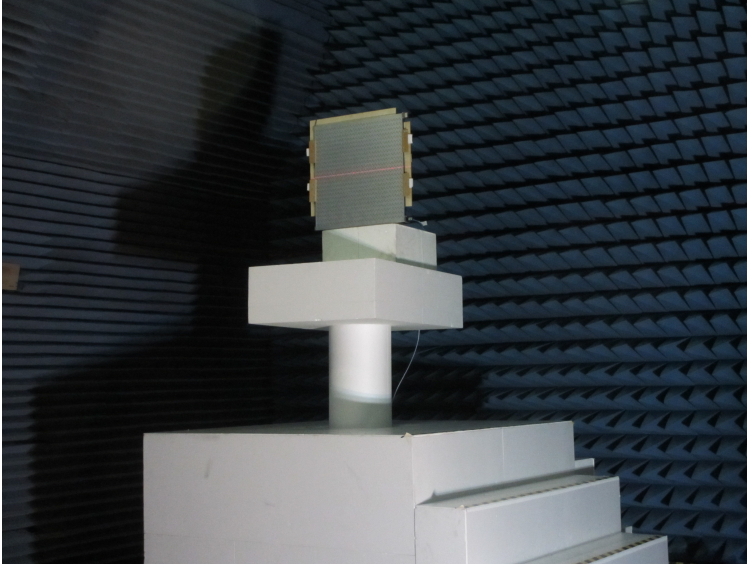


Figure 3-17: Range ambiguity performance of the antenna. Satellite altitude is taken as 600 km, and pulse duty cycle of 20%. An horizon angle of 66 deg from nadir is assumed beyond which no echoes shall be received. The antenna pattern is of RHCP pattern in XZ plane. Reflectivity of the surface is uniform (independent of incidence angle). γ is stepped at a resolution of 0.01° , and f_P step size is 10Hz . The swath-width imaged is constant 25 km at all (f_P, γ) . The blank region corresponds to times when nadir echo interference with desired signal occurs. The front-end Low Noise Amplifier (LNA) may saturate in this scenario, and hence operation at these operating points should be avoided.

3.5.2 Far-Field Measurements

Far-field measurements are carried out to measure the antenna absolute gain and axial ratio. The pattern shape too is measured and compared with the directive patterns from near-field measurement. Fig.3-18 shows the far-field measurement setup in a large anechoic chamber. The antenna panel is mounted on a wooden support and placed on foam structure. A standard X-band horn antenna is used for calibration. The receiver antenna too is linearly polarized X-band horn antenna. To measure the axial-ratio we rotate the receiver horn antenna manually and take gain measurements.



(a) Antenna Under Test (AUT) mounted on wooden support



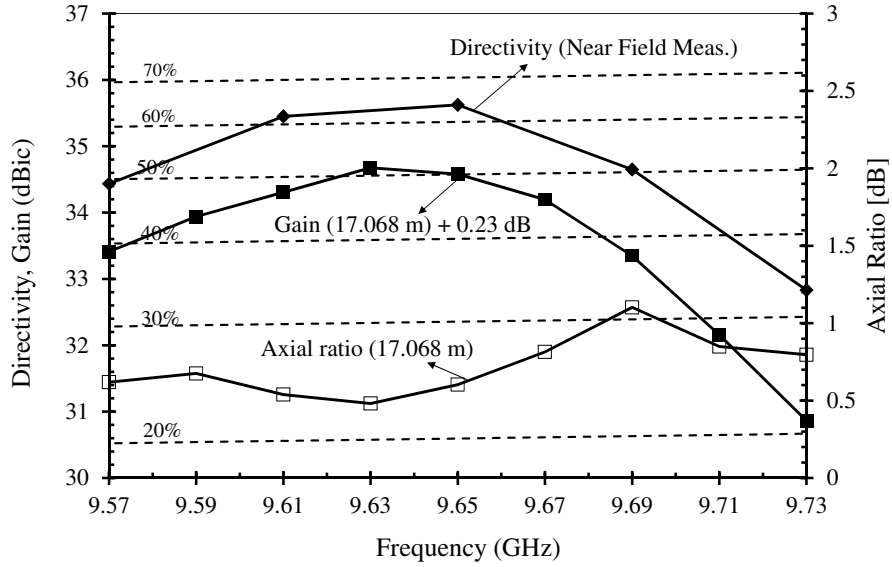
(b) Standard X-band horn antenna for calibration



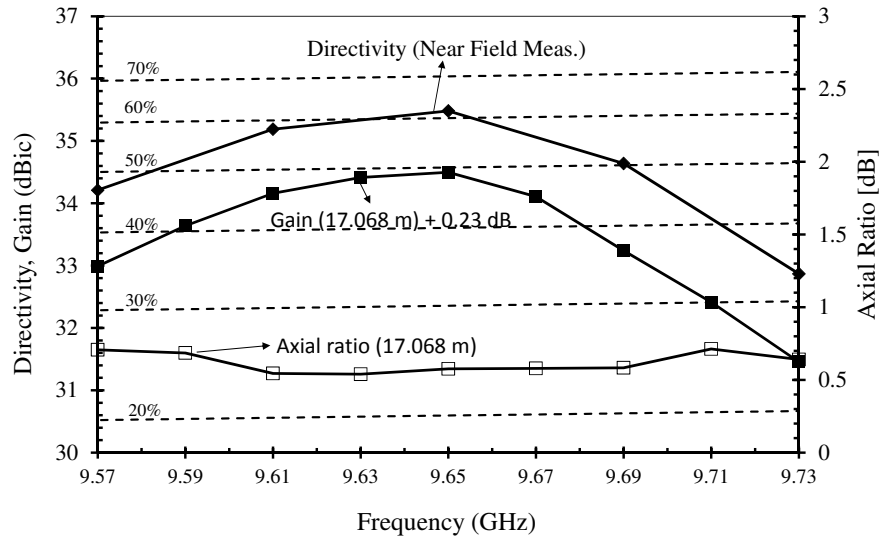
(c) Receiver X-band horn antenna

Figure 3-18: Far-field antenna test setup

The distance between the Antenna Under Test (AUT) and receiver horn antenna is 17.068 m which is less than the Fraunhofer far-zone criteria ($2D/\lambda^2$, D is the maximum dimension of antenna). An adjustment factor 0.23 dB is added to the measured gain to give equivalent far-zone gain measurement. Fig.3-19 shows the gain, directivity and axial ratio measurements at different frequencies. This plot was made with the AUT pointing in the direction which yields peak at 9.65GHz.



(a) RHCP



(b) LHCP

Figure 3-19: Directivity, gain and axial ratio. The measurements shown are at direction corresponding to maximum directivity (and gain) at 9.65 GHz. An adjustment factor of 0.23 dB is added to the gain measured at 17.068 m.

At 9.65 GHz, RHCP beam has directivity of 35.6 dBic and gain of 34.6 dBic corresponding to aperture efficiency of 50.1%. The LHCP beam has directivity of 35.5 dBic and gain of 34.5 dBic corresponding to aperture efficiency of 49.2%. The conductor and dielectric losses in the antenna can be estimated by finding the difference between directivity and gain measurements. In Table.3.5 we compare the measure-

ment results of this dual-polarization antenna panel with the previously fabricated single-polarization, uniform aperture excitation rectangular parallel-plate slot-pair array antenna in [55] [51].

Table 3.5: Comparison of the dual-polarization antenna panel with single-polarization, uniform aperture excitation rectangular parallel-plate slot-pair array antenna.

Parameter	Single polarization antenna panel [55] [51]	Dual polarization antenna panel
Aperture efficiency	RHCP: 54%	RHCP: 50.1% LHCP: 49.2%
Antenna losses	1.6 dB	1 dB

¹ Calculations are made by taking value of peak gain, peak directivity at 9.65 GHz.

Degradation in aperture efficiency is expected for the case of the dual-polarization antenna panel, since the aperture amplitude is tapering perpendicular to waveguide feeder(see Fig.3-14). The losses are also smaller in this case since the effective dielectric volume in which the traveling wave energy propagates is less as compared to the case of the uniform aperture excitation antenna panel.

3.5.3 Voltage Network Analyzer (VNA) Tests

Voltage Network Analyzer (VNA) is used to measure the reflectivity and transmission s-parameters of the RHCP, LHCP waveguide feeder input ports. A photograph of the VNA test setup is shown in Fig.3-20. Foam wedges are laid on top of the antenna panel to absorb radiations and prevent backscatter from surrounding objects.

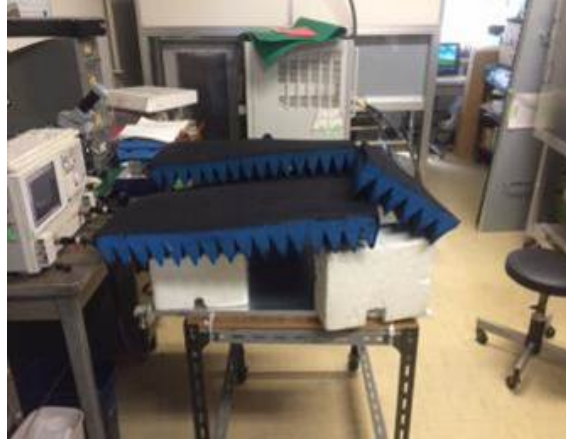


Figure 3-20: VNA test setup

Fig.3-21 shows the measured reflection and isolation s-parameters over a wide frequency band. The residual power is less than -20 dB as designed, and reflection is less than -15 dB, within our bandwidth of interest.

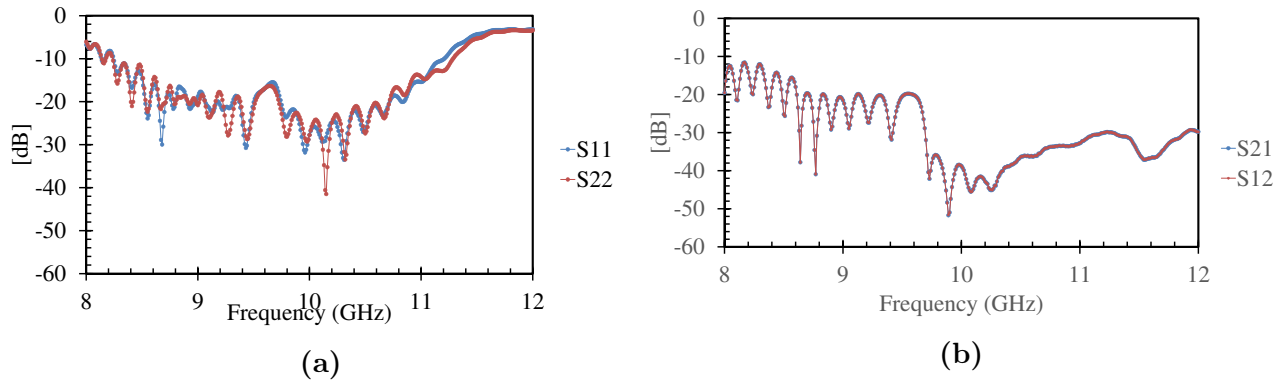


Figure 3-21: Reflection and Isolation between RHCP port (port 1) and LHCP port(port 2).

3.6 Synthesis of Optimal Excitations of an Array of Antenna Panels

After obtaining the field-pattern of the antenna panel, we begin the design of the set of excitation coefficients for the array of antenna panels. We can write the equivalent mathematical model as shown in Fig.3-22. All panels are identical and are approxi-

mated to a single-point radiator with the elemental pattern as that of the measured antenna panel pattern. They are uniformly spaced by distance equal to nearly 1 panel length. The panels are excited by a waveguide feeder network, an example of which is shown in Fig.3.5. We make a simplification to our design by constraining all the panels to be excited in-phase.

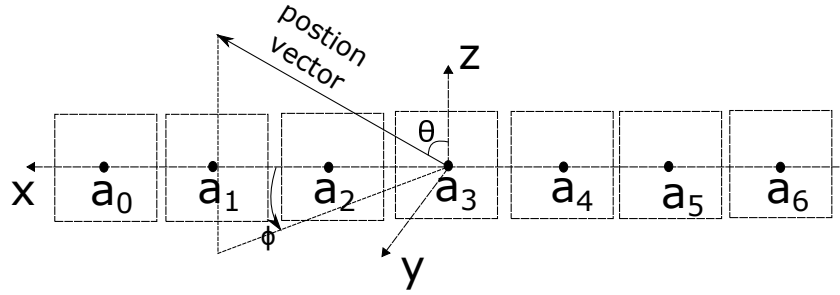


Figure 3-22: Linear array model of antenna panels.

We can write the crossrange pattern $F_{cr}(\phi)$ of the SAR antenna as:

$$F_{cr}(\phi) = F_{panel}(\pi/2, \phi)AF_2(\pi/2, \phi) \quad (3.11)$$

where, F_{panel} is the antenna panel pattern obtained from measurements (see Fig.3-16b for plot of F_{cr}). The excitation of the array of panels has the effect on the overall antenna directivity D_{SAR} and cross-range pattern (see Fig.2-11). Thus we may define the optimization objectives as:

1. Maximize minimum directivity over main lobe of the cross-range pattern $D_{SAR}(\pi/2, \phi)$ to improve σ_{NEZ}^0 .

$$D_{SAR}(\pi/2, \phi) = k|E_{cr}|^2/(a_0^2 + a_1^2 + \dots + a_6^2) \quad (3.12)$$

where k is a constant of proportionality and can be proven to be the same irrespective of the set of amplitude excitations a_0, a_1, \dots, a_6 chosen.

2. Maximize the modified beam efficiency (see eqn. 2.7) of the crossrange pattern

to reduce azimuthal ambiguity.

$$B_E^M = \int_{\phi=\pi/2-\delta}^{\pi/2+\delta} |F_{CR}(\phi)|^2 \sin^2 \phi d\phi / \int_{\phi=\phi_{hrz}^-}^{\phi_{hrz}^+} |F_{CR}(\phi)|^2 \sin^2 \phi d\phi$$

2δ is the mainlobe beamwidth about the crossrange direction, $\langle \phi_{hrz}^-, \phi_{hrz}^+ \rangle$ correspond to horizon angles beyond which echoes will not occur.

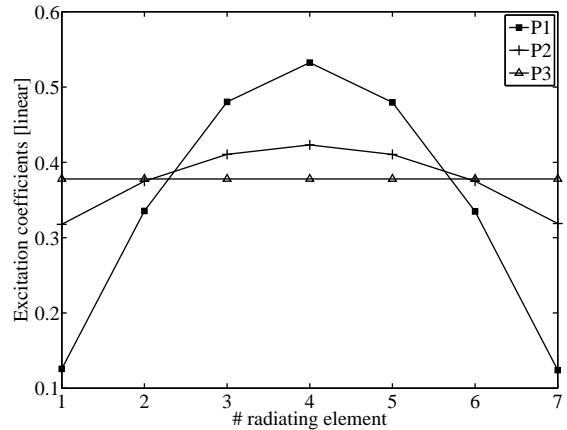
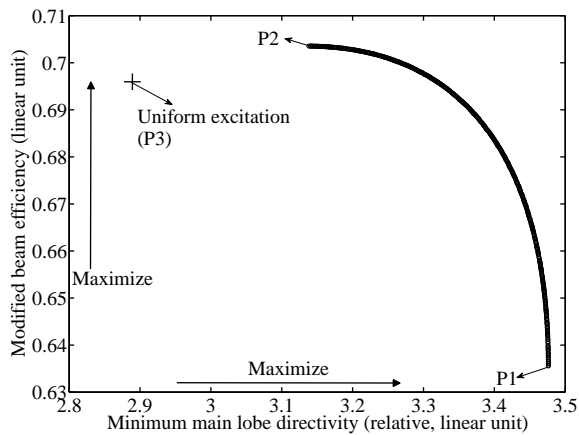
We use NSGA-II as our multiobjective optimization algorithm. Table.3.6 shows the simulation parameters.

Table 3.6: Optimization parameters for crossrange pattern synthesis.

Number of radiators	7
Inter-element spacing	$70 \text{ cm} \approx 1L_{panel}^{feeder}$ L_{panel}^{feeder} is length of panel along waveguide feeder
Main lobe beamwidth	$\lambda/7L_{panel}^{feeder} = 0.36 \text{ deg}$
Horizon angle about nadir	66 deg
Optimization variables	Set of excitation amplitudes
NSGA-II Parameters	
Population size	500
Number of generations	500
Probability of cross-over	0.9
Probability of mutation	1/7
Distribution index of crossover	15
Distribution index of mutation	20

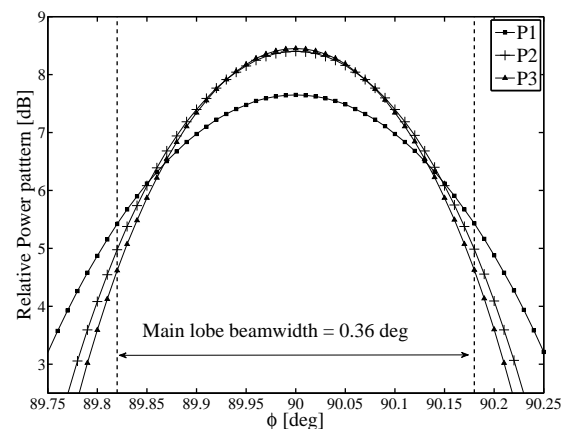
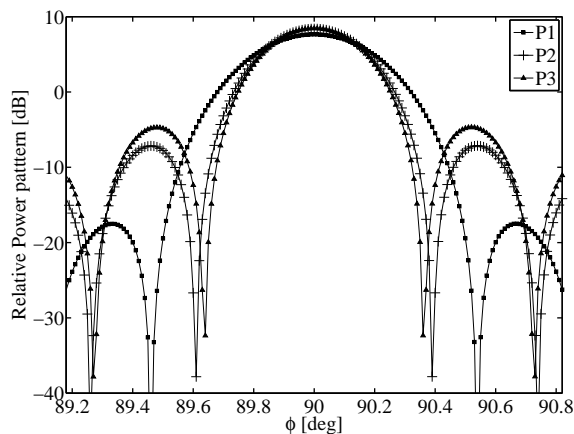
The optimization results are detailed in Fig.3-23. The Pareto front converges to the convex shape as shown in Fig.3-23a and remains fairly independent on use of a different number of generations or different number of species. It is useful to compare three points in the Pareto graph labeled as P1, P2 and P3. P3 is a point corresponding to case of uniform excitation and is not a solution of the optimization. However, it

is plotted to get a better idea of the solutions. P3 is inferior in terms of the chosen objectives. P1 corresponds to the solution point which yields maximum minimum main lobe directivity while P2 corresponds to solution point yielding maximum B_E^M . The tradeoff between P1 and P2 is 6.8% difference in B_E^M and 0.44 dB difference in minimum main lobe directivity.



(a) Pareto curve from optimization. The concave shape indicates a trade-off between the defined objectives.

(b) Excitation coefficients corresponding to points P1, P2 and P3 in the pareto-curve.



(c) Antenna power pattern of points P1, P2 and P3 showing the peak and first side-lobe levels.

(d) Antenna power pattern of points P1, P2, P3 showing the main-lobe.

Figure 3-23: Results of NSGA-II optimization of the antenna cross-range pattern

3.7 Summary

This chapter presented optimal design for space-based SAR antenna using a traveling wave antenna. Though it was carried out specifically for parallel-plate slot-pair array antenna, the mathematical model of the traveling wave antenna, optimization procedure may be applied to a more general class of antenna design problems. Use of a multi-objective optimization algorithm yielding Pareto solutions has been uncommon in antenna design problems, but are shown to be useful.

A prototype antenna panel was fabricated and tested. It shows aperture efficiency of 50.1% and 49.2% at 9.65 GHz for RHCP and LHCP beams respectively. A beam shift was also observed between the RHCP, LHCP beams at design frequency of 9.65 GHz. The deviation in design is attributed to inaccurate modeling of the honeycomb, adhesive permittivity between the parallel plates. More generally, the frequency dependent beam-shift effect of travelling wave antenna restricts its application to narrow-band systems.

Finally using the measured results of a single antenna panel, an excitation configuration for array of multiple panels is proposed. This configuration can be later used in design of RHCP, LHCP waveguide feeder network.

Chapter 4

Design of Cylindrical Cavity Power Combiner

This chapter describes the design of a low-loss, X-band RF power combiner, an important technology needed to be realized for enabling small satellite SAR using a centralized RF feed passive-array antenna.

Section.4.1.1 details the power requirements of the SAR mission. Different high RF power sources and the reason behind the decision of using RF power source made of coherently combined SSPA outputs is discussed in Section.4.1.2. In Section.4.2, an overview of power combiners is provided based on study from previous literature. Power combining architectures is discussed and examples of power combiners previously implemented is described. Based on this study, we select a suitable power combining structure for Section.4.3 details the proposed structure design. Section.4.4 describes implementation of design by modeling and simulation in a computer electromagnetic simulation software. Later a prototype unit is fabricated whose electrical characteristics are measured with help of VNA. The measured and simulated results are compared. Finally we summarize in Section.4.2.

4.1 Background

4.1.1 Power requirements

The power requirement of the SAR depends for a given orbit altitude, antenna, frequency of operation, imaging geometry, and target σ_N of the mission, where $\sigma_N = \frac{\sigma_0}{SNR_{image}}$, where σ_0 is the distributed target reflectivity (m^2/m^2). The σ_N is given by Eqn.4.1 [16, Pg. 20].

$$\sigma_N = \frac{256\pi^3 kT}{c} (R^3 v_x \cos \psi_g) \frac{B_T F_N L_{radar} L_{atmos}}{P_{avg} G_A^2 \lambda^3} \frac{L_R L_a}{a_{wr} a_{wa}} \quad (4.1)$$

where,

λ is operating wavelength.

$R \approx \frac{H}{\cos \eta}$ is distance (range) to target, H is satellite altitude and η is nadir-offset angle.

$P_{avg} = P_t d$, is the average transmitted power, P_t is peak transmit power and d is duty cycle.

ψ_g , is grazing angle at target location.

c is velocity of light.

k is Boltzmann constant.

v_x is orbital velocity which can be determined from satellite altitude.

T is nominal scene noise temperature $\approx 290\text{K}$.

F_N is system noise factor for the receiver and typically has a value of 3 to 3.5 dB for X-Band sub-kilowatt radar systems.

B_T is effective signal bandwidth of the radar waveform within the data.

G_A is the antenna gain-factor. We can get a rough estimate by employing the following relation: $G_A = 4\pi\eta_{ap}A_A/\lambda^2$, where η_{ap} is aperture efficiency, A_A is the physical area of antenna. Note that this relation assumes uniform aperture excitation field distribution.

a_{wr} is range impulse response broadening factor due to data weighting or windowing.

a_{wa} is azimuth impulse response broadening factor.

L_r is reduction in SNR gain due to non-ideal range filtering.

L_a is reduction in SNR gain due to non-ideal azimuth filtering.

L_{radar} is hardware system losses. Typical numbers are 0.5 dB to 2 dB from Tx amplifier to the antenna port, and perhaps an additional 0.5 dB to 1.5 dB two-way through the radome. L_{atmos} is the atmospheric loss factor (two-way).

Note: The typical values stated above are taken from [16].

For the mission microXSAR, we may use the following values to get an estimate of the minimum peak transmitting power required: $\sigma_N < -20$ dB, $B_T = 150$ MHz, $F_N = 3.5$ dB, $A_A = 0.7 * 4.9$ m², $\eta_{ap} = 60\%$, $\eta = 25$ deg, $v_x = 7616$ m/s corresponding to $H = 500$ km, $\psi_g = 90 - \eta = 55$ deg, $R = 610.39$ km, $a_{wr} \approx L_r \approx 1.2$, $a_{wa} \approx L_a \approx 1.2$, $d = 20\%$. $L_{radar} = 3.5$ dB, $L_{atmos} = 0.5$ dB.

$$\implies P_t \geq 748\text{W}.$$

4.1.2 High RF Power Sources for Space Applications

Table.2.1 surveys the RF power technologies used in various SAR missions. The other space application in which a centralized high-power RF supply is used, is in communication satellites. There are mainly two types of high-power transmitters used in space-technology: vacuum-tube and solid-state devices (SSPA). Among vacuum-tube technologies, there are various types such as klystrons, traveling wave tube amplifiers (TWTAs), magnetrons, crossed-field amplifiers, gyrotrons [93]. Historically speaking, the most popular high-power RF source has been TWTAs. For example, in a study by [94], a survey of 565 communication satellites was conducted with launch years 1982 to 2016. Of the 565 satellites, the amplifier type (TWTA/SSPA) was not specified for 260 payloads. Of the remaining 305 satellites, 74% of the satellites has entirely SSPA payloads, 6% has SSPA only payloads, and 20% had combination of both type of amplifiers onboard.

The debate between TWTA and SSPA as a better choice for high-power RF supply has still not reached a conclusive point. In the private industry, there are players actively manufacturing products using both technologies. The fundamentally different operating technologies also lead to different performance characteristics, which make

them difficult to compare. TWTAs may outperform SSPAs in terms of output power, power efficiency, size and cost [95]. The lower power efficiency of SSPAs leads to large heat generation, which must be dissipated by heat sinks. While the basic SSPA RF module is smaller in comparison with those of TWTAs, the required heat sinks typically cause the overall SSPA package to be larger than the TWTA [94]. A lower output power implies, a SSPA radar transmitter has to employ higher duty cycle to meet requirements of average power. This has a significant effect on the rest of the radar system where large pulse width limits the maximum pulse repetition frequency (for a fixed observable swath) [17].

However, TWTAs, being multi-electrode vacuum device, have several challenges in development. They require highly sophisticated High-Voltage Electronic Power Conditioners (HV-EPC) to provide conditioned and isolated voltage rails, with stringent regulation / ripple requirements [96]. SSPAs on the other hand, would require a relatively low dc voltage DC/DC converter, which may be shared with other satellite components such as reaction wheels, sensors.

Another interesting performance characteristic to consider is graceful degradation. In theory, a high-power RF source using SSPAs exhibits graceful degradation characteristics, since it is made by coherently combining RF output of several SSPAs [95]. Therefore in case of failure of one of the RF power amplifiers, the entire high-power RF supply unit should not stop working altogether. Although this hypothesis is good in theory, a different behavior has been observed in practice. [97] in the year 2005 made a statistical comparison of TWTAs vs SSPAs of the Boeing fleet of commercial satellites in-orbit. In this report, it is noted that most of the failures of SSPAs were not graceful-degradation reflecting gradual loss of power, but in fact, hard failures such as no downlink, sudden loss of power/shutoff. Thus the usefulness of graceful degradation characteristic of SSPAs is debatable.

Next performance metric to compare is the demonstrated in-orbit reliability. A metric of evaluating the reliability of a device is Failures in Time (FIT) experienced per billion amplifier operating hours. Fig.4-1 is reproduced from [98] where a recent in-orbit analysis of TWTAs vs SSPAs of the Boeing fleet of satellites was studied. It

shows the FIT rate of SSPAs is decreasing at a higher rate as compared to TWTAs. In near future, the FIT rate of SSPA may go well below that of TWTAs, making them more attractive.

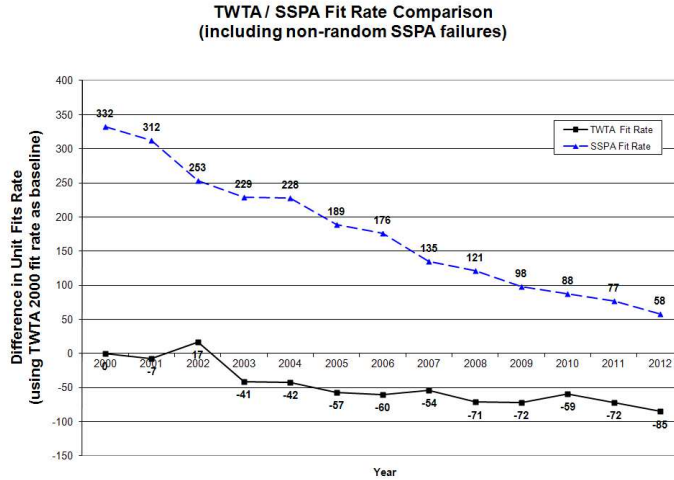


Figure 4-1: Running trend of On-Orbit Relative FIT Rate [98].

In terms of the development cost and handling, SSPA would score over TWTA, since SSPAs are relatively easily available at lower costs and do not require specialized equipment for testing and prototyping. They do, however, require a low-loss power combining structure, which can add coherently output of several SSPAs to a single high-energy RF pulse. TWTA handling requires special skill to deal with high-voltage electronics. Many commercial simulation software are available to simulate behavior of SSPAs using the manufacturer given circuit models. These factors make us lean towards choosing SSPAs over TWTAs.

4.2 Power Combiners Overview

This section discusses background topics related to power combiners such as their characteristics, power combining methods, different power combining architectures and finally a survey on microwave power combiner realized in the past. This serves as the foundation for the implemented power combiner design.

4.2.1 General Characteristics of Power Combiners

As stated in Section.4.1.2, high-power amplifiers using SSPAs need to be made by combining output power coherently from several SSPAs. The science behind RF power combining emerged since the late 1960s and is quite mature. With the help of current electromagnetic simulation software, it is now possible to quickly arrive at a working model of power combiner by starting with a reasonable power combining architecture. Keeping this in mind, it can be said the main challenge in this task is the selection of a reasonable architecture and a rough electric structure to start optimization and design using computer simulations.

A powerful mathematical technique for microwave network analysis is using scattering matrix (S-matrix). Irrespective of the underlying architecture, topology, and components used, the combiner can be represented by a S-matrix. The scattering matrix relates the voltage waves incident on the ports to those reflected from the ports [99] and can be later applied to determine performance characteristics of power combiner. It also has practical use since the S-matrix can be directly measured using a network analyzer.

Consider an arbitrary N port microwave network as shown in Fig.4-2.

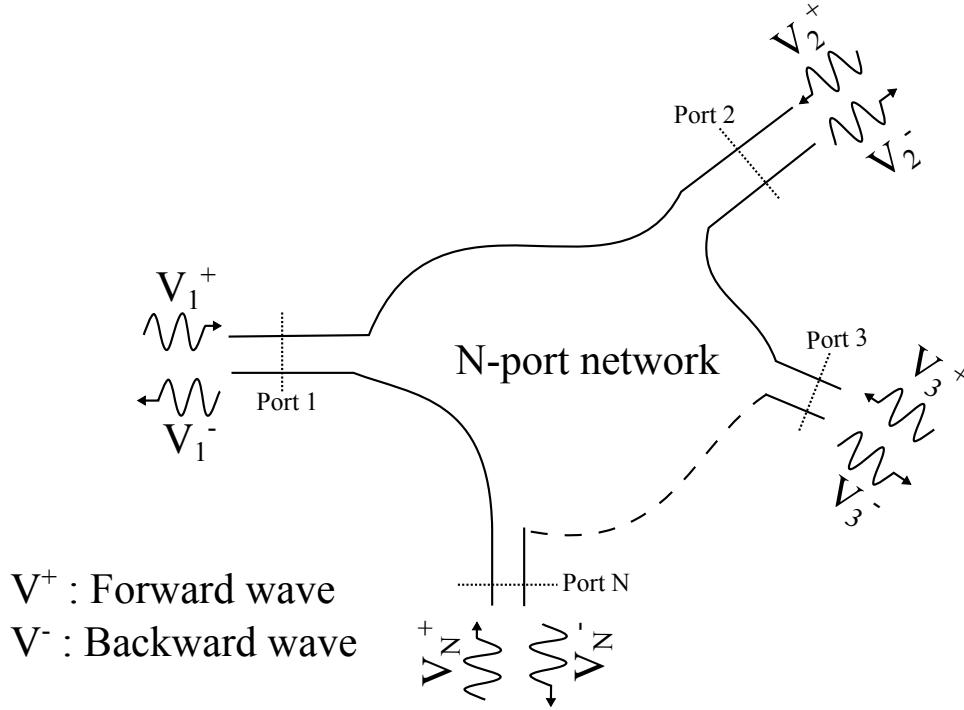


Figure 4-2: Arbitrary N port microwave network.

The S-matrix is defined as [99]:

$$\begin{bmatrix} V_1^- \\ V_2^- \\ \vdots \\ V_N^- \end{bmatrix} = \begin{bmatrix} S_{11} & S_{21} & S_{13} & \dots & S_{1N} \\ S_{21} & S_{22} & S_{23} & \dots & S_{2N} \\ \vdots & \vdots & \vdots & \vdots & \vdots \\ S_{N1} & S_{N2} & S_{N3} & \dots & S_{NN} \end{bmatrix}$$

$$[V^-] = [S][V^+] \quad (4.2)$$

where $[V^-]$ is matrix of reflected waves and $[V^+]$ is matrix of incident waves, $S_{ij} = \frac{V_i^-}{V_j^+} \Big|_{V_k^+ = 0 \text{ for } k \neq j}$

Let us now see the basic performance characteristics of a power combiner and write it in terms of S-matrix. Let port N be the output port and ports 1 to (N-1) be input ports of the power combiner. Therefore,

$$[V^+] = [1 \quad 1 \dots 1 \quad 0]^T$$

1. Insertion loss: The insertion loss of a power combiner represents the efficiency of the combining in the combiner. It is simply the ratio of output power to the total input power in decibels.

$$\begin{aligned}
IL_{dB} &= 10 \log_{10} \frac{|V_N^-|^2}{|V_1^+|^2 + |V_2^+|^2 + \dots + |V_{N-1}^+|^2} \\
&= 10 \log_{10} \frac{|S_{N1}V_1^+ + S_{N2}V_2^+ + \dots + S_{N(N-1)}V_{N-1}^+|^2}{|V_1^+|^2 + |V_2^+|^2 + \dots + |V_{N-1}^+|^2} \quad (4.3)
\end{aligned}$$

If expressed as linear term, i.e. ratio of output power to total input power, it is called as combining efficiency.

2. Bandwidth: Bandwidth is the range of frequencies over which the power combiner exhibits the desired/ good combining characteristics such as insertion loss, active return loss, etc. The chosen bandwidth depends on the application and for radars is generally narrowband.
3. Active return loss: A power amplifier has a maximum rating on the reverse flowing power it can handle at its output port. If the reverse power at the power amplifier output exceeds this rating it can damage the power amplifier. If the power combiner is interfaced to the power combiner via an isolator, we have to consider the maximum reverse power rating of the isolator.

Increased reverse power also implies a loss in combining efficiency. We evaluate this factor by a metric called the active return loss. Active return loss is the ratio of backward power at output port of a single power amplifier to the output power produced by that power amplifier as given in Eqn.4.4.

$$\text{active } S_{k \text{ dB}} = 20 \log_{10} \frac{|V_k^-|}{|V_k^+|} = 20 \log_{10} \left| S_{k1} \frac{V_1^+}{V_k^+} + \dots + S_{kk} + \dots + S_{k(N-1)} \frac{V_{N-1}^+}{V_k^+} \right| \quad (4.4)$$

where k is the port of interest.

4. Graceful degradation: In general when there is a failure of one or more input

power amplifiers, there is degradation in combining efficiency. Having graceful degradation means the operational amplifiers are not affected by the failures, and that the greatest possible power be delivered to output port [100]. For example, say in a power combiner with N amplifiers, if M amplifiers fail, the output power should decrease to $(N - M)/N$ of the original output power.

5. Size: We desire a compact size of the power combiner so it can be accommodated in small satellite bus. Additionally, the topology of the power combiner influences the arrangement of power amplifiers and other components relevant to radar transmitter electronics. A planar topology would allow for easy placement of heat pipes to dissipate generated heat.

4.2.2 Power Combining Techniques

Microwave and millimeter-wave power combining techniques have been of interest since the late 1960s, with development in solid-state microwave sources such as the IMPATT diode in 1956 [101], GaAs MESFET in 1966 [102], GaAs HEMT in 1979 [103] and its derivatives: pseudomorphic HEMT and metamorphic HEMT, and since late 1990s the GaN HEMT. Although the nature of microwave sources has continually evolved, the science of power combining remains same, i.e. the power combining techniques are relatively independent. An extensive review of the power combining techniques can be found in the literature in [104]. Though it was published three decades ago the lessons from them are still relevant today. Fig.4-3, reproduced from [104] shows a classification of different basic combining techniques.

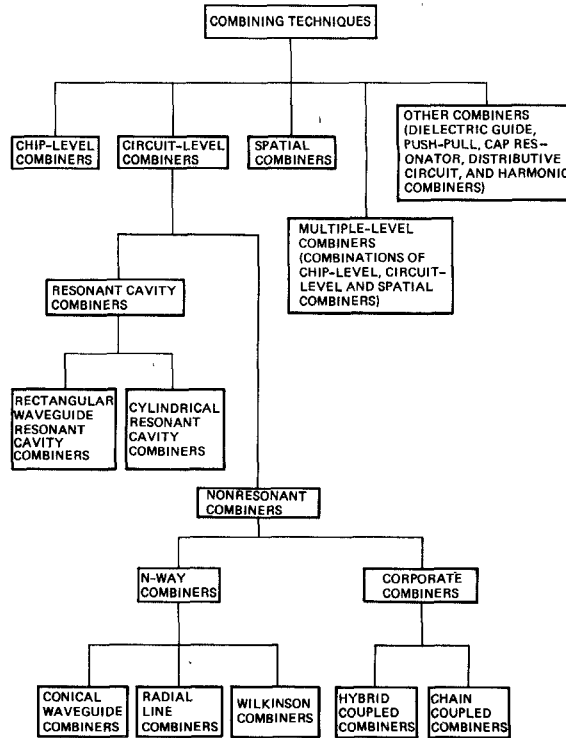


Figure 4-3: Different combining techniques [104].

Power combiners are divided into mainly four categories as shown in Fig.4-3: chip level combiners, circuit level combiners, spatial combiners, and combinations of the three.

Chip-level combiners employ power combining techniques directly on chip, for example, [105] demonstrated monolithic power combining using current at 2.4 GHz producing up to 33.5-dBm saturated power with 37.6% Power Added Efficiency (PAE).

Spatial combiners consist of a large array of radiating elements. They utilize the proper phase relationship of many radiating elements to combine the power in space [104]. A phased array antenna is an example, which utilizes separate power amplifier modules to excite individual radiators, and at the far-field combines power at the peak direction. Another example is reported in [106] which uses a grid of fifty MESFET's arranged as 25 differential amplifiers, which accept vertically polarized power and amplifies it and radiates it as horizontally polarized power.

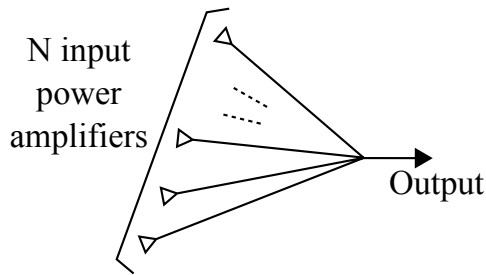
In circuit level combiners the sources are treated as a discrete unit manufactured

separately from the power combining unit. They are thus much larger as compared to chip-level combiners. Circuit level combiners can be broken down into resonant cavity combiners and non-resonant cavity combiners. [107] reviews circuit level combining architectures, namely chain/serial, tree/corporate and N-way combiners (see Fig.4-4). Resonant cavities are usually N-way combiners, i.e. power combining takes place at a single stage.

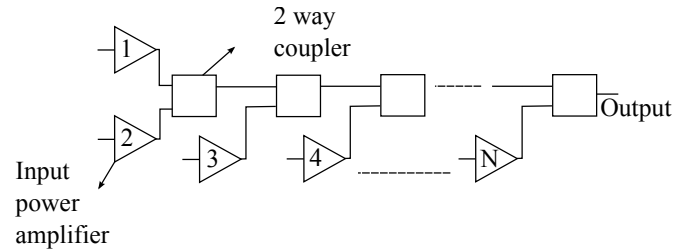
Resonant cavity combiners are commonly cylindrical or rectangular cavities. One of the first resonant cavity structures was reported in [108], which utilized coaxial lines mounted on the narrow side wall of X-band rectangular cavity, coupling with magnetic-field of TE_{10n} mode in resonant cavity.

Non-resonant combiners can employ either N-way or serial, tree architectures. For example, the Wilkinson [109] and radial-line combiners [110] feed N input lines of characteristic impedance Z_0 to an output line with characteristic impedance $\sqrt{N}Z_0$. Serial and corporate combiners use 2-way couplers such as Wilkinson combiner, branch line 90° hybrid, rat race and coupled line directional coupler (see Fig.4-4).

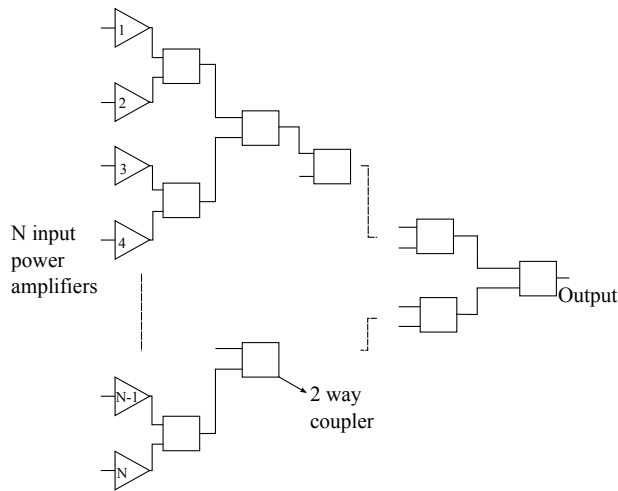
Table.4.1 is a recent (Year 2015) review on power combining methods reported in [111]. Different circuit level power combining methods are evaluated according to various performance characteristics such as combining efficiency, bandwidth, etc. It can be seen that resonant combiners exhibit maximum combining efficiency, but only a narrow operational bandwidth. Low bandwidth is due to the resonant nature of the combining cavities, while large combining efficiency is because combining takes place in air/vacuum, a low loss dielectric medium. Spatial combiners (spatial combiners in [111] refers to "closed" systems, i.e. they are contained within an over-moded, conductive structure or cavity (ex: see [112]) and not too phased arrays) exhibit poor efficiency but are otherwise excellent for large power combining. Combiners using a number of combining stages such as a tree structure will exhibit lower efficiency as compared to N-way combiners where combining takes place in a single stage (ex: non-resonant radial, conical).



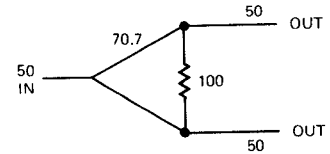
(a) N-way power combiner architecture



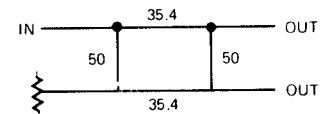
(b) Chain/ Serial power combining architecture



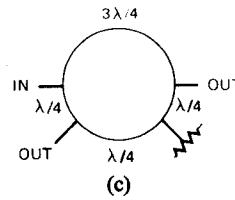
(c) Tree/ Corporate power combining architecture



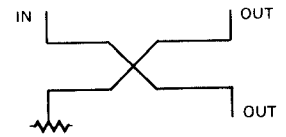
(a)



(b)



(c)



(d)

(d) Common forms of power combiner couplers [107]. (Strictly speaking, dividers are pictured here; if input and output roles are interchanged they become combiners.) (a) Wilkinson combiner (2-way). (b) Branch line 90° hybrid. (c) Rat race. (d) Coupled line directional coupler.

Figure 4-4: Circuit level power combining architectures

Table 4.1: Summary of Power Combining Methods [111]

Method	Combining Eff. (%)	Bandwidth	Planar	Suitability for large order combining	Heat removal	Graceful Degradation
Tree of Binary Hybrids	70-80	Octave	Y	Poor	Good	Yes
Resonant Radial	95	Narrow, <1%	N	Good	Good	No
Non-Resonant Radial	80-90	Moderate	N	Good	Fair	Moderate
Conical	80-90	Moderate	N	Good	Fair	No
Spatial Combiners	40-55	Moderate	N	Excellent	Fair	No
Traveling Wave or Serial	75	Octave	Y	Fair	Good	Yes
Non-Uniform TL	70-80	Multi-Octave	Y	Poor	Good	Moderate

4.2.3 Survey of Microwave Power Combiners

In this section, a survey of previous microwave circuit level power combiners is presented. Each power combiner has a fundamental different structure and different performance characteristics. The survey helps in narrowing down our search of a suitable combining structure for application in small satellite SAR system. As a precaution, it should be noted that some of the combiner efficiency results reported in the survey includes efficiency of the individual power amplifiers.

Kurokawa Rectangular Cavity Combiner (1971) [108]

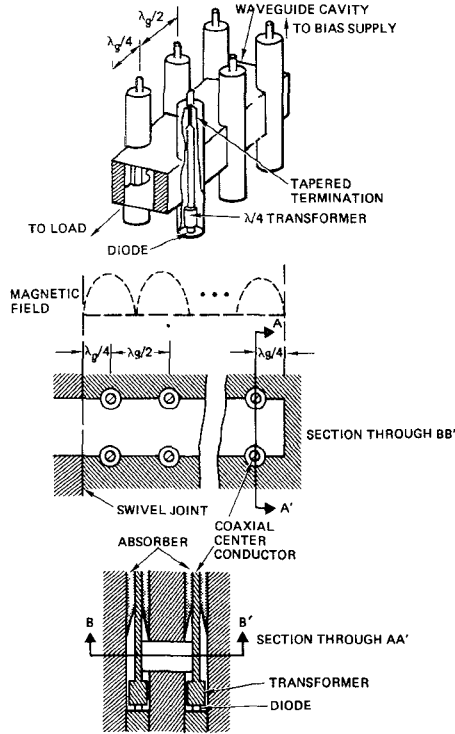


Figure 4-5: Kurokawa rectangular cavity combiner [104]

Output of 12 packaged IMPATT diodes is combined in rectangular cavity TE_{10n} mode. Magnetic field coupling by coaxial lines placed every $\lambda_g/2$ distances at the side wall of cavity starting from position $\lambda_g/4$ at the short end of cavity, i.e. they are placed at magnetic field maxima of the cavity. In-phase excitation of the coaxial lines excites TE_{106} mode. Other end of coaxial cable is terminated by a tapered absorber 10.5 W CW power, with 6.2 percent efficiency is obtained at 9.1 GHz.

A disadvantage with this structure is that the cavity length increases with an increase in the number of inputs. This can excite spurious modes in the

frequency band of interest, which reduces combining efficiency.

Matsumura Circular TM_{0m0} Mode Cavity Combiner with Coaxial Interface (1987) [113]

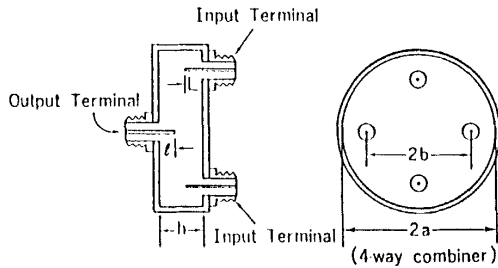


Figure 4-6: Structure of cylindrical cavity TM_{0m0} combiner [113].

40 W, 12 GHz band TM_{0m0} mode 8-way cylindrical combiner was fabricated with input 5W FET amplifiers. It exhibited less than 0.5 dB insertion loss in 300 MHz bandwidth. The combiner uses open-circuited coaxial line inputs and outputs. Slits and subcavity auxiliary structure is developed to suppress the effect of spurious modes in case of failure of one or more

FETs, and thus provide graceful degradation characteristics.

Matsumura Circular TM_{0m0} Mode Cavity Combiner with Waveguide Ports (1988) [114]

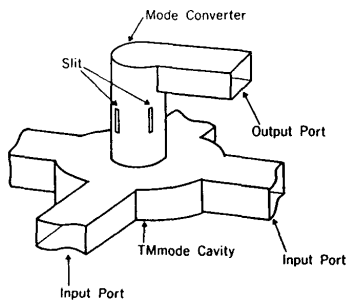


Figure 4-7: Structure of four-way cavity combiner [114].

A 14 GHz four-way combiner with TM_{020} mode is reported exhibiting insertion loss of 0.25 dB. Rectangular waveguides are connected as input terminals with a circular waveguide as output port. The output is transformed into a rectangular waveguide via a TM_{01} - TE_{10} mode transformer. Slits are cut in axial direction of the circular waveguide to radiate energy from unwanted TE_{11} mode. Additionally, four slits are placed radially on the bottom of the resonator to absorb spurious modes in case of malfunction of one or

more input power amplifiers. The 1 dB down bandwidth about 14.25 GHz can be seen to be 500 MHz.

Knox Waveguide Combiner (1995) [115]

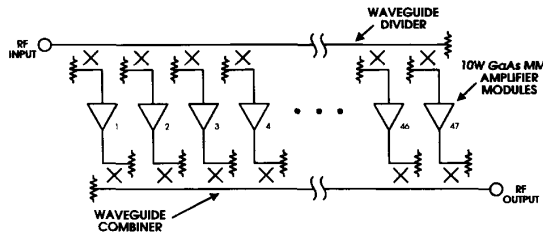


Figure 4-8: Block diagram of an X-band 400W solid-state amplifier [115]

Forty-seven 10W GaAs MMIC amplifier modules was combined using a 47:1 low-loss waveguide combiner, achieving output power of 400 W CW in X-Band. It reported less than 0.5 dB insertion loss and port-to-port isolation of greater than 25 dB. A microstrip to waveguide transition is used to facilitate the combination of all modules in the waveguide medium.

Kanto suspended line substrate corporate combiner (2008) [116]

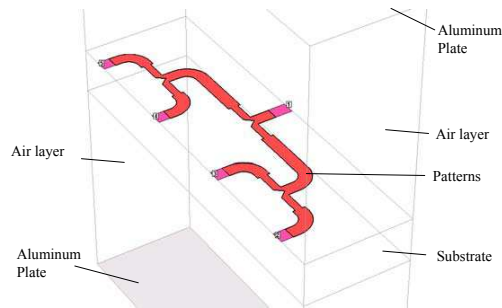


Figure 4-9: Suspended microstrip line corporate power combiner [116].

Output powers from four 80 W GaN HEMTs is combined in a suspended line, corporate binary structure. It consists of copper patterns on 0.25 mm PTFE substrate and two aluminum plates. Between the substrate and aluminum plates, 1.2 mm air layers are used as the dielectric to decrease dielectric loss. Reflection s-parameters for the input ports are poor, because isolation resistors were removed to minimize insertion loss of combiner.

Ghanadi microstrip radial combiner (2011) [117]

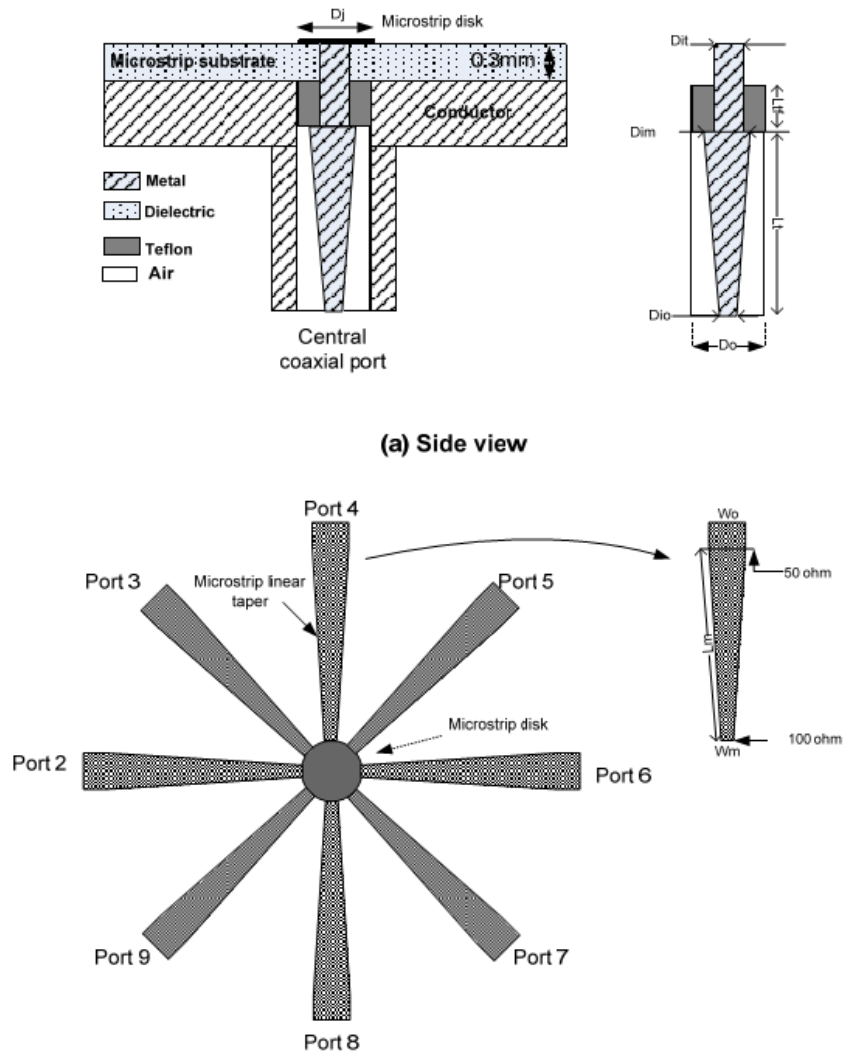


Figure 4-10: Drawing of 8-way microstrip combiner with important parameters [117].

An N-way radial wideband microstrip power combiner is fabricated and tested to give insertion loss below 1.5 dB, return loss above 10 dB operating from 2 GHz to 17 GHz. The input microstrip lines and output coaxial cable is tapered towards the central microstrip patch, for the sake of impedance matching.

4.3 Description of Proposed Structure

4.3.1 Selection of Power Combining Technique

Section.4.2 presented an overview of power combining techniques, including a survey of previous power combiners. The requirements of power combiner (See Section.4.1.1) can be met by combining the power from six GaN HEMT power-amplifier, each unit power-amplifier capable of sourcing 150 W peak power at 25% duty cycle. Furthermore, the chirp bandwidth of SAR system is fixed at 200 MHz, which is $\approx 2\%$ of the carrier frequency, which can be met by a narrow-band power combiner.

Chip level power combiners currently are limited to low power output and do not meet the specifications of high power in radars. A traveling-wave combiner such as the Knox waveguide combiner [115], does not offer compact size with a large number of power amplifier inputs. An N-way combining architecture is preferred over chain, tree architecture, so the number of combining stage are reduced. A non-resonant, wideband N-way radial combiner such as the Ghandadi microstrip radial combiner [117] offers comparatively higher insertion losses since the combining takes place in a lossy dielectric substrate. Resonant cavity N-way combiners are applicable since the bandwidth requirement is relatively low and resonant cavity combiner offer good combining efficiency.

Among the resonant cavity combiners, the rectangular resonant cavity structure (example: Kurokawa rectangular cavity combiner [108]) and the cylindrical cavity structure (example: Matsumura TM_{0m0} mode cavity combiner [113][114]) look promising. In a cylindrical cavity combiner, the power amplifier inputs may be placed in an axially symmetric fashion, which would result in a similar diagonal s-parameters in the power combiner network S-matrix, and would hence be simpler to design.

SSPAs are commonly mounted on a printed circuit board, and the RF output is made available by a microstrip line interface. It would be desirable to directly connect the output microstrip lines to the power combiner, rather than change the type of interface using a adapter. The output of the power combiner has to be interfaced to the antenna rectangular waveguide feeder network, and thus direct rectangular

waveguide output interface is desired. Based on these considerations, a qualitative power combining structure is drawn in Fig.4-11.

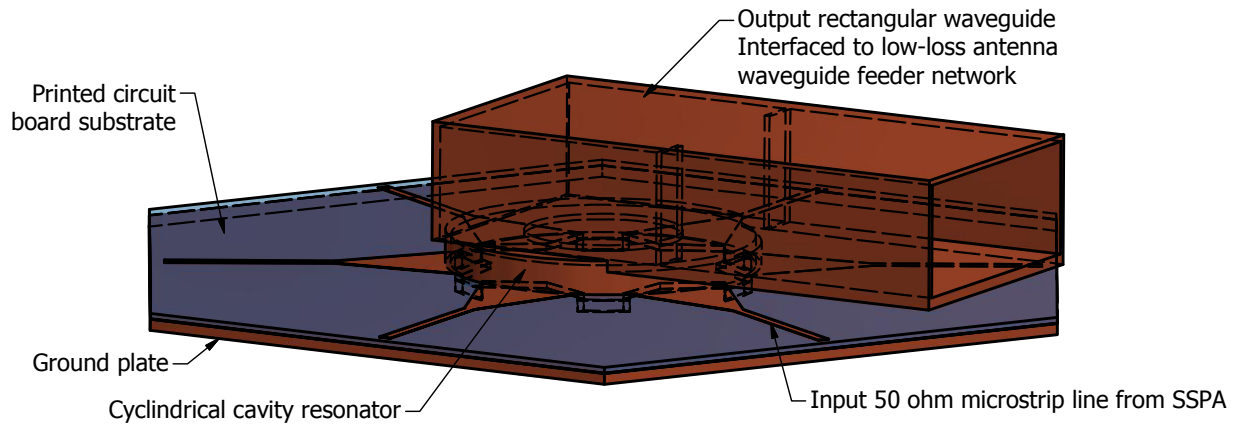


Figure 4-11: Qualitative structure of proposed cylindrical cavity power combiner.

The rest of this section describes the process behind obtaining initial dimensions of the above proposed structure (such as cylinder radius, cylinder height, etc) to make a computer simulation model. Later in simulation, more optimization is done by varying the initial dimensions to realize a low-loss power combiner.

4.3.2 Cylindrical Cavity

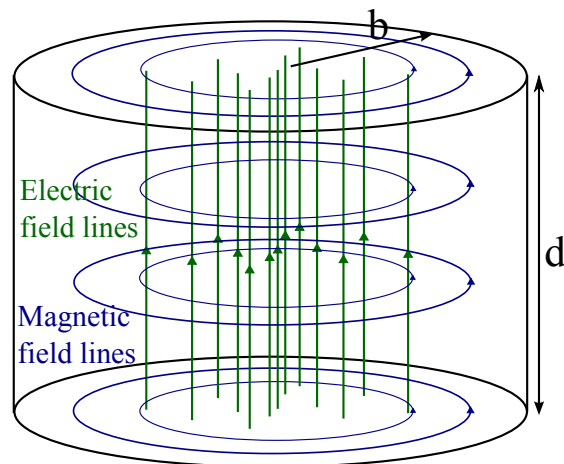


Figure 4-12: Illustration of TM_{010} mode in cylindrical cavity

Fig.4-12 shows an illustration of TM_{010} mode in cylindrical cavity. The input microstrip lines are placed in an axially symmetric fashion around the cylinder, and when excited in-phase will couple to the TM_{010} magnetic field lines. The resonant frequency of the TM_{lmn} mode for a cylindrical cavity is given by Equation.4.5[99, Chapter 6]:

$$f_{nml} = \frac{c}{2\pi\sqrt{\mu_r\epsilon_r}} \sqrt{\left(\frac{p_{nm}}{b}\right)^2 + \left(\frac{l\pi}{d}\right)^2} \quad (4.5)$$

where, b is the radius of cavity, d is the height of cavity, c is the velocity of light, μ_r and ϵ_r are relative permeability and relative permittivity of the cavity medium respectively, p_{nm} is m^{th} root of $J_n(x)$. For a air-filled cavity with TM_{010} resonant frequency fixed at 9.65 GHz, we get the radius of cavity $b = 11.89\text{mm}$.

To determine the cavity height, we look at the mode chart (Fig.4-13). The mode chart shows what modes can be excited at a given frequency for a given cavity size [99, Chapter 6]. We should be careful that no other modes can be excited in our bandwidth of interest (+/- 100 MHz) which leads to three possible operating regions:

$$0.07 < (2b/d)^2 < 0.23 \quad (4.6)$$

$$0.26 < (2b/d)^2 < 0.93 \quad (4.7)$$

$$1.02 < (2b/d)^2 \quad (4.8)$$

For radius $b = 11.89\text{mm}$, we get:

$$49.6\text{mm} < d < 89.9\text{mm}$$

$$24.7\text{mm} < d < 46.6\text{mm}$$

$$d < 23.5\text{mm}$$

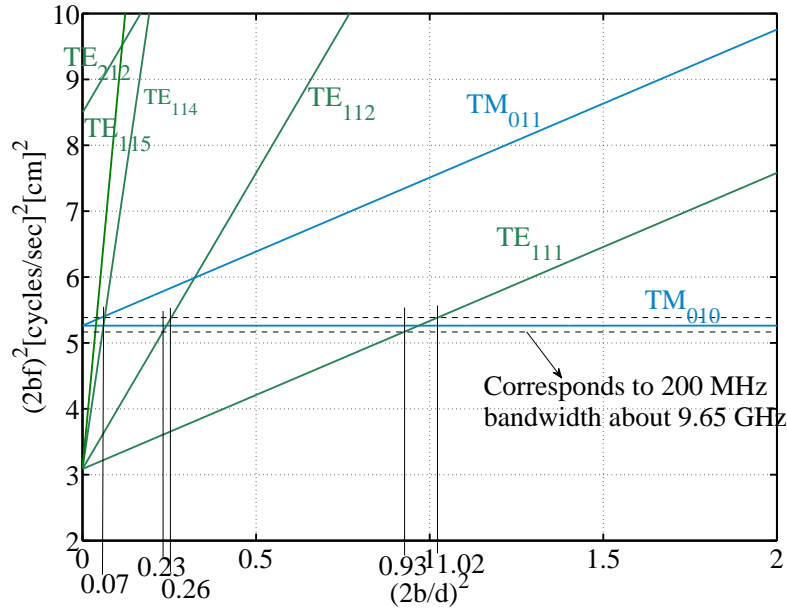


Figure 4-13: Cylindrical cavity mode chart. Feasible region of operation corresponds to 200 MHz bandwidth.

The unloaded quality factor Q_0 of the cavity resonator is given by Eqn.4.9 [118].

$$Q_0 = \frac{\eta p_{01}}{2R_S (b/d + 1)} \quad (4.9)$$

where R_S is the surface resistance and $\eta = 120\pi$. Thus a larger d is preferable for higher Q_0 and hence lower conductive losses. However, the cavity height also influences the external Q of the combiner and hence the bandwidth. Hence it must be appropriately chosen.

4.3.3 Microstrip Line Interface to Cavity

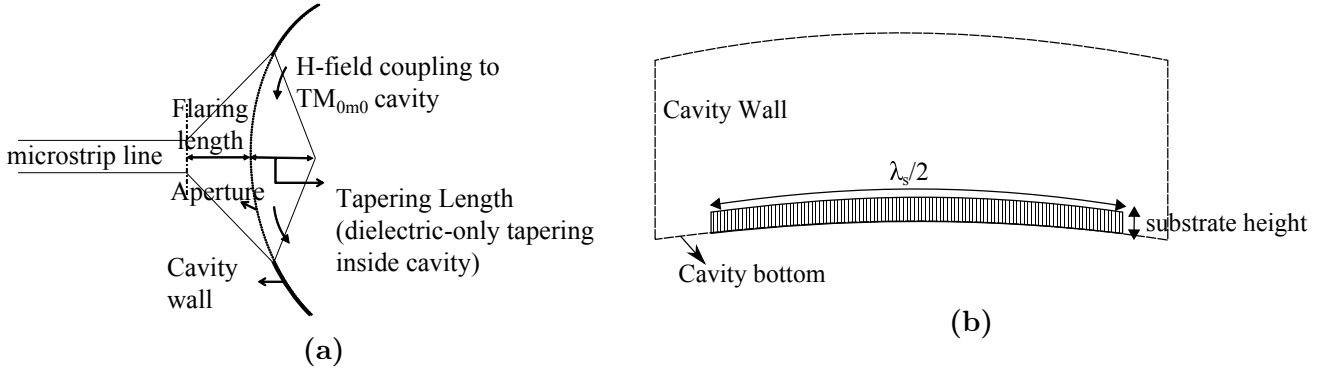


Figure 4-14: Microstrip line interface to cavity

The microstrip line interface to the cavity wall is shown in Fig.4-14. A thin slot of nominal length $\lambda_s/2$ is cut on the cavity wall parallel to TM_{010} magnetic field lines, and hence leaks TM_{010} energy from the cavity (if we think of the combiner as a divider, which is true for reciprocal microwave networks). λ_s is the wavelength in substrate.

The microstrip line is designed to be of characteristic impedance 50ohm, and is gradually flared to meet the slot cut on the cavity wall. Inside the cavity, the substrate is gradually tapered. The gradual flaring, tapering structure is done to prevent sudden discontinues, which can cause reflections.

4.3.4 Substrate Selection

There are mainly three considerations on choice of the substrate for the circuit board.

1. It is desired that the permittivity of the substrate is high, so that the guide wavelength is low, and hence the length of the slots cut on the cavity wall is low. The perimeter of the cavity wall is fixed for a particular resonant frequency (TM_{010} mode), which limits the maximum number of slots of length $\lambda_s/2$ which can be cut on the cavity cylinder.
2. In general, a substrate exhibits complex permittivity with some conductivity. The imaginary part of the dielectric constant and conductivity give rise to losses

in form of heat. The total loss is specified by a parameter called the loss-tangent which is desired to be low.

- 3. Radar is a high-power application, which requires proper thermal management. A circuit material's power-handling capability is related to its capability to control to control temperature rises as a function of applied and dissipated power [119]. Better thermal conductivity leads to less mechanical stress, and improvement in circuit performance, lifetime.

RT/duroid 6035HTC laminate from Rogers Corporation is a feasible candidate. The laminate relative dielectric constant (Dk) is 3.6, loss tangent of 0.0013 at 10GHz and thermal conductivity of 1.44W/m/K. Fig.4-15 shows heat flow versus the temperature rise for different $Dk = 3.5$ laminates. The heat rise of a resistor placed on a microstrip circuit attached to a controlled heat sink was measured, at increasing power levels [120]. RT/duroid 6035HTC exhibits the best characteristics.

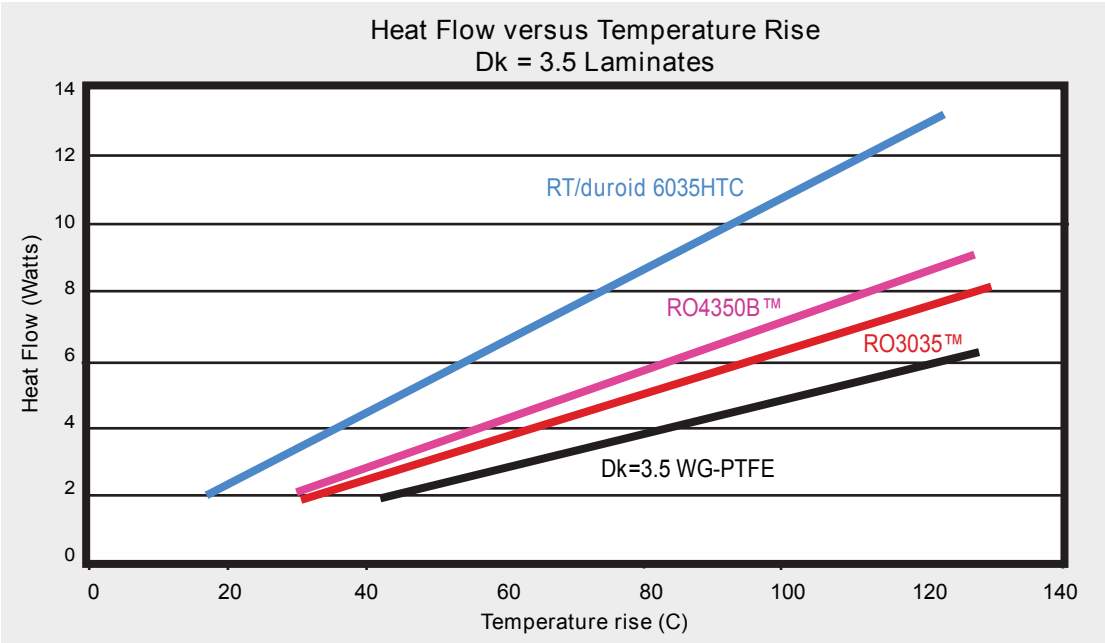


Figure 4-15: Heat flow versus temperature change. $Dk = 3.5$ Laminates. Four different 3.5 Dk laminate materials were tested, and the RT/duroid 6035HTC laminate most effectively dissipated heat away from the resistor to enable the lowest temperature rise [120].

4.3.5 Rectangular Waveguide Interface to Cylindrical Cavity

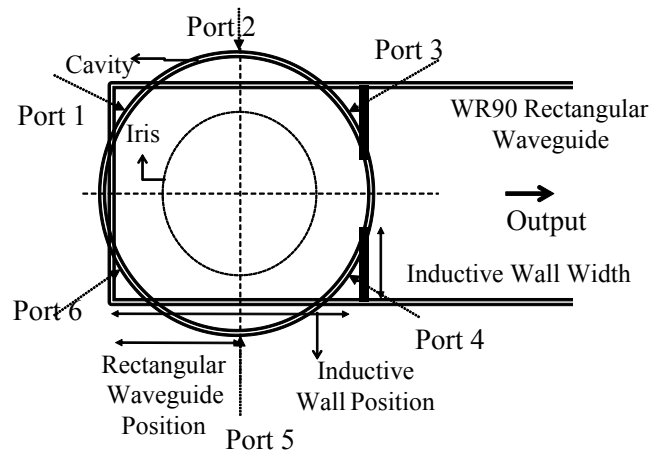
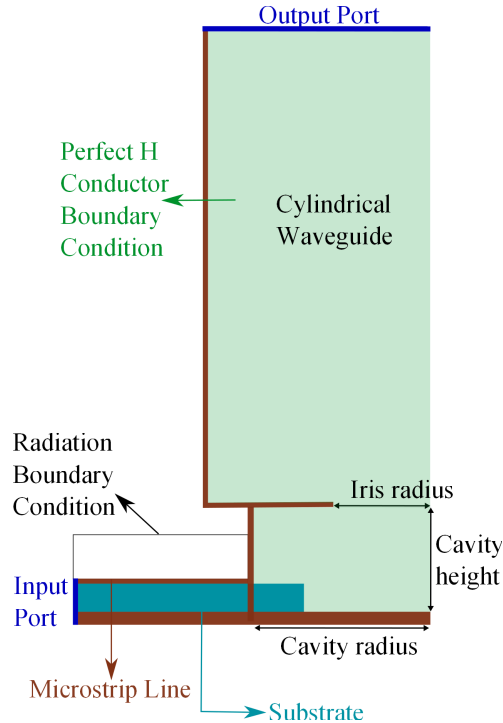


Figure 4-16: Rectangular waveguide interface to cylindrical cavity

The rectangular waveguide interface to the circular cavity is shown in Fig.4-16. A circular iris on the cavity top wall leaks energy into the rectangular waveguide. The cylinder cavity center is aligned at nominal distance of $\lambda_{rw}/4$ from the shorted end of rectangular waveguide, where λ_{rw} is the TE_{10} wavelength in rectangular waveguide. This allows coupling to the TM_{010} magnetic field to the TE_{10} magnetic field in rectangular waveguide. Inductive walls [121, Chapter 4] are placed at nominal distance of $\lambda_{rw}/2$ from the waveguide short. The width and position of the inductive walls are varied for impedance matching.

4.4 Implementation of the Design

4.4.1 Reduced Model Driven Mode Simulation



Parameter	Value
Cavity, Cylinder thickness	1 mm
Conductor material	Copper
Substrate	Rogers 6035 RTD
Substrate height	0.508 mm
Microstrip Line width	1.0768 mm
Microstrip Line thickness	15.24 um
Cylinder radius	14.8 mm

Figure 4-17 & Table 4.2: Reduced model of the power combiner.

The purpose of simulating a reduced model is to accelerate the design process. HFSS simulations are computationally intensive and having a reduced model helps to speed up the solver. Also a reduced model helps to work with fewer optimization variables in the preliminary stage.

Fig.4-17 shows the structure of the reduced power combiner. Since we have six inputs, we break down the TM_{010} cavity in azimuthally symmetric fashion about its longitudinal axis into 6 sectors. The sectored-plane of the $1/6$ th cavity is set to perfect magnetic conductor boundary condition to support TM_{010} mode. The reduced cavity is coupled to a reduced cylindrical waveguide to which we can attach a port. Note we cannot directly simulate coupling to output rectangular waveguide since the rectangular waveguide cannot be reduced in azimuthally symmetric fashion. The reduced cavity is interfaced to flared microstrip input line with dielectric tapering.

The optimization variables are detailed in Table.4.3 along with the initial values. We solve by adjusting the variable values about their initial values, and seeing the effect on the optimization criterion, which is to minimize reflection s-parameter of the input microstrip line port.

Parameter	Initial Value	Optimized Value
Aperture Width	$\lambda_{ms}/2 = 9.27\text{mm}$	13.52 mm
Flaring Length	-X-	8.22 mm
Tapering Length	-X-	2.95 mm
Cavity Radius	11.89 mm	13.95 mm
Iris Radius	-X-	8.00 mm
Cavity Height	$49.6\text{mm} < d < 89.9\text{mm}$ (or) $24.7\text{mm} < d < 46.6\text{mm}$ (or) $d < 23.5\text{mm}$	3.00 mm

Table 4.3: Optimization variables for the reduced model.

4.4.2 Full Model Driven Mode Simulation

Figure.4-18 and Table.4.4 show the simulation model of the entire unit along with important parameters. This model has the complete cylindrical cavity and separate input ports for the six SSPAs. The circular output waveguide is replaced by rectangular waveguide with a matched output port.

Note that circular azimuth symmetry of the structure is broken once the rectangular waveguide is placed and thus the characteristics of ports 1,2,3,4,5,6 are now not

identical. Noting the symmetry about hexagon diagonal line joining vertices between port 1,6 and 3,4 (see Fig.4-18), we expect the characteristics of following pairs of input ports are identical: (1,6), (2,5) and (3,4). During optimization, we try to match the characteristics of all the ports by introducing unequal flaring length for the three pairs of ports.

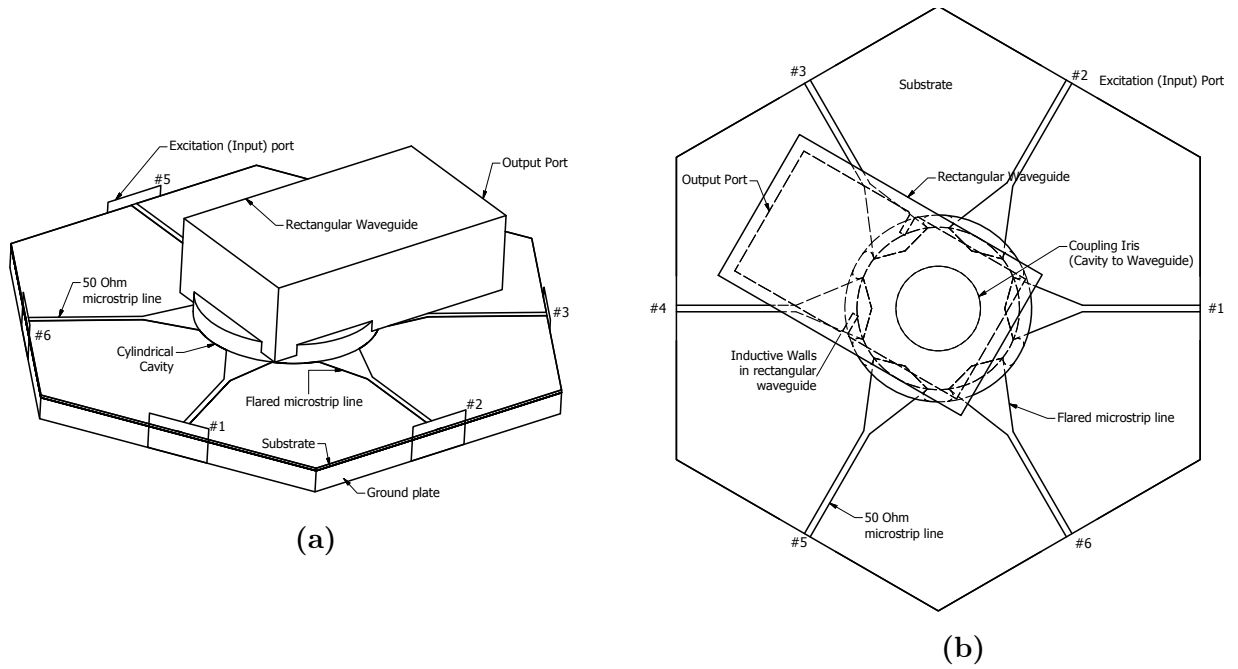


Figure 4-18: HFSS full model simulation. Cavity thickness was increased from 1 mm to 2 mm to meet manufacturer requirement. Additionally, non-zero fillet radius is taken into account. Mechanical support structures are added, but not shown in above figure since they have small effect on electrical performance.

Parameter	Initial Value	Optimized Value
Rectangular waveguide position	$\lambda_{rw}/4 = 10.59\text{mm}$	10.1 mm
Inductive wall position	21.18 mm	20.94 mm
Inductive wall width	-X-	3.70 mm
Aperture width	From reduced model	10.57 mm
Flaring length	”	9.45 mm
Tapering length	”	2.45 mm
Cavity radius	”	13.45 mm
Iris radius	”	7 mm
Cavity height	”	3.08 mm

Table 4.4: Optimization variables for the full model.

4.4.3 Prototype Assembly

The small size of the components and non-standard microstrip line to cavity interface made the fabrication of the prototype unit challenging. The overall power combiner model was broken down into individual sub-components, which could be fabricated using standard techniques. Later, the sub-components were assembled in-house using low-temperature solder and adhesive. The assembly process is illustrated in Fig.4-19.

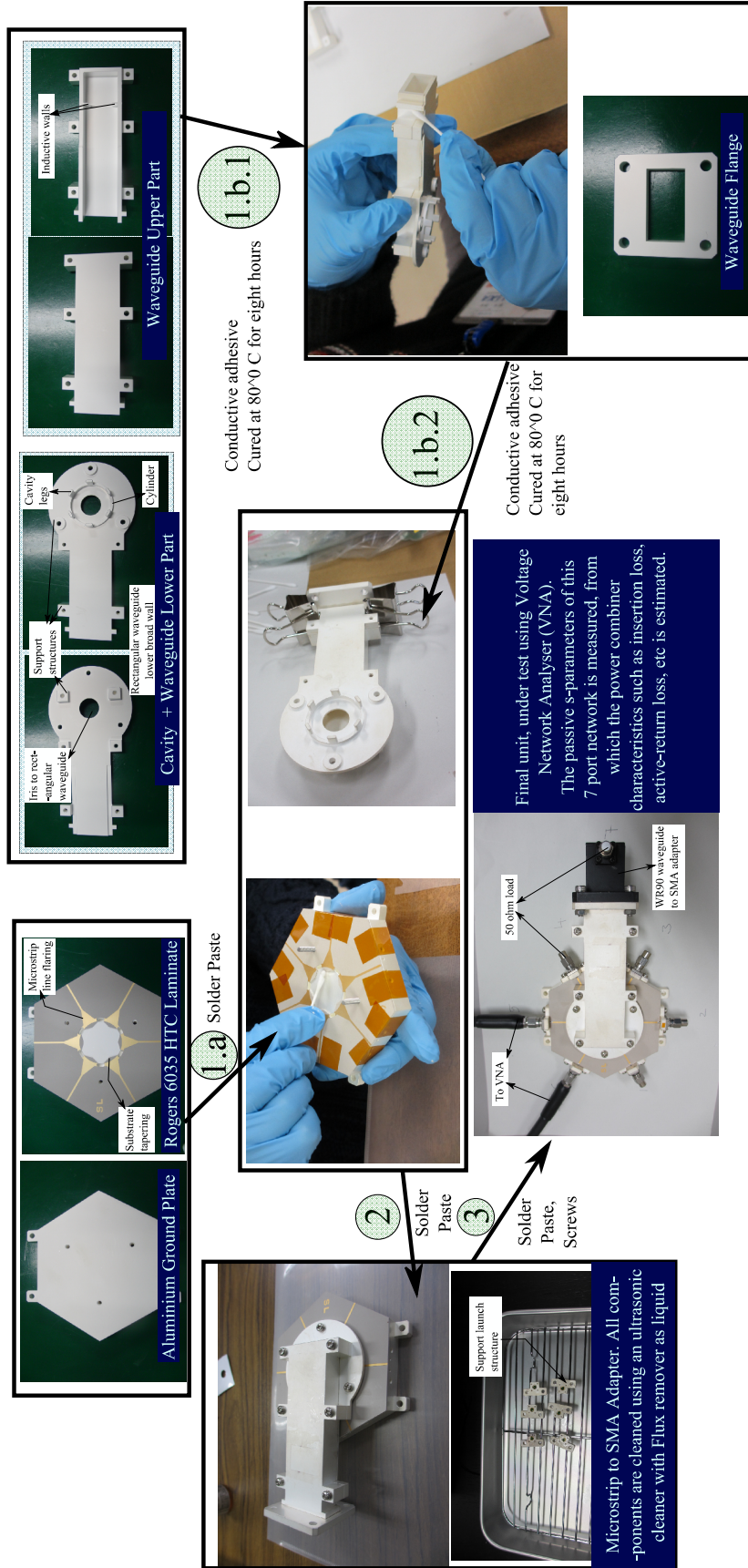
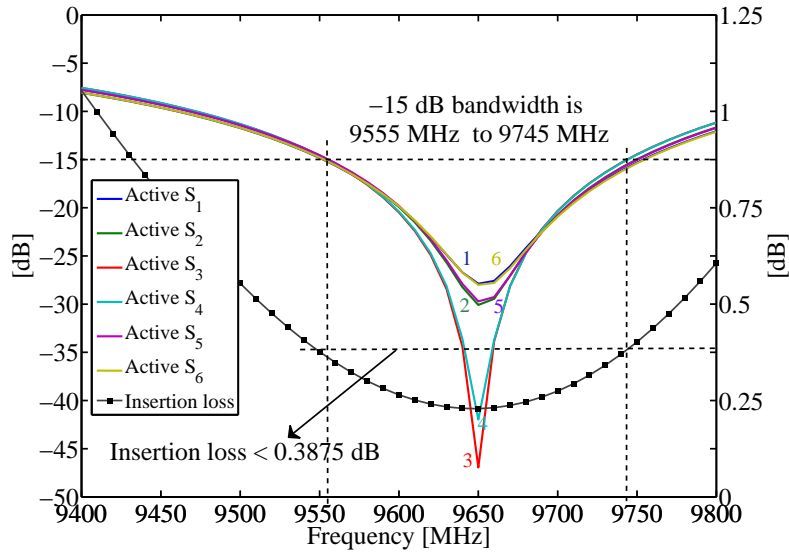


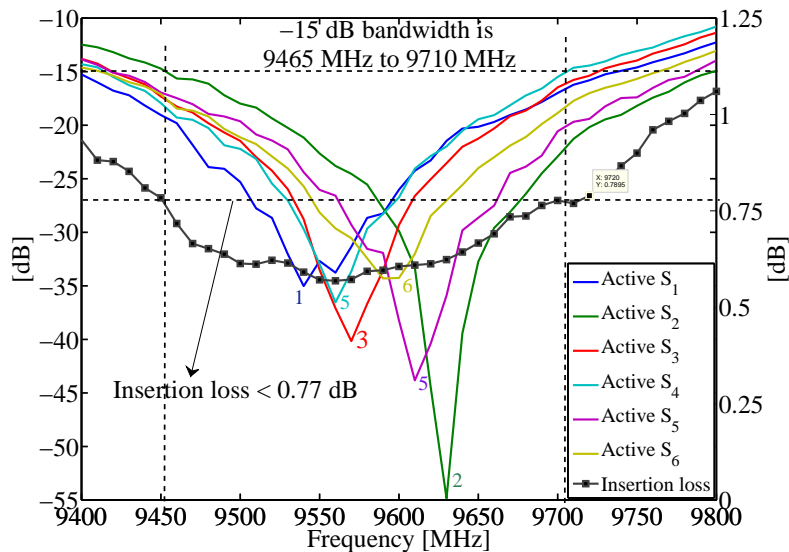
Figure 4-19: Illustration of power combiner assembly process

4.4.4 Simulation versus Measurement Results

Fig.4-20 and Table.4.5 summarize the simulated and measured power combiner characteristics. The measured center frequency is about 60 MHz below the design center frequency. Moreover, the measured -15 dB bandwidth is higher. This deviation from design is attributed to errors in manufacturing of the prototype parts and its assembly.



(a) Simulation results.



(b) Measurement results. The adapter losses in the experimental setup are also included in the shown insertion loss.

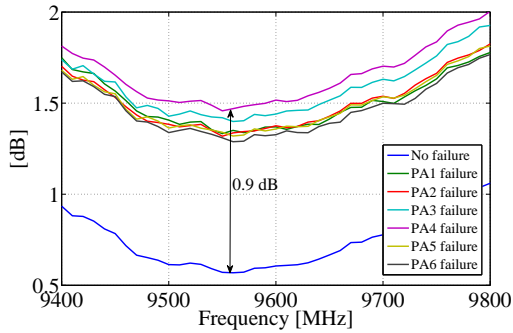
Figure 4-20: Power combiner simulation versus measurement results.

Table 4.5: Power Combiner: Simulated versus Measured Characteristics

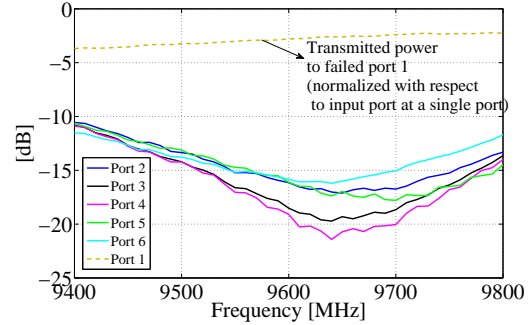
Parameter	Simulation	Measured
Bandwidth	190 MHz	245 MHz
Center frequency	9650 MHz	9588 MHz
Insertion loss	<0.3875 dB	< 0.77 dB ^a

^aIncludes measurement adapter losses

Fig.4-21 shows the degradation characteristics of power combiner on failure of one power amplifier. The degradation depends on the position of the failed power amplifier with respect to the output rectangular waveguide. Here we assume that even after failure, the port of the failed unit is perfectly matched. Such a scenario is valid when the power amplifier is connected to the power combiner via an isolator.. The transmitted power to the failed port is high (-2 dB as seen in Fig.4-21b). This places a requirement on the isolator to be capable of handling this high return power.



(a) Insertion loss in case of one power amplifier failure degrades by 0.9 dB compared to the case of no-failure. Note that the insertion loss in case of failure of one power amplifier is calculated with respect to input power from the five active power amplifiers.



(b) Return power in case of degradation of the power amplifier at position '1' is <-12.4 dB in bandwidth of interest to the active ports. The transmitted power to the failed unit is -2.5 dB (relative to input power at a single port).

Figure 4-21: Power combiner measured degradation characteristics.

4.5 Summary

In this chapter, we addressed the issue of design of high-power RF source to act as a centralized transmitter to excite the passive SAR antenna. The power requirement calculations were made, which showed peak transmitting power requirement above 748 W. Previously implemented high RF power sources were discussed, specifically vacuum-type power amplifiers and SSPAs. To achieve high-output power using SSPA technology power combiners is explored. A cylindrical cavity power combiner with microstrip line inputs and rectangular waveguide output is proposed and designed. The simulated and measurement power combiner properties are compared. The fabricated prototype unit shows insertion loss less than 0.77 dB over 245 MHz bandwidth (-15 dB level of the active return power at the input power amplifiers). The compact structure and low-loss characteristics favor its application in small satellite SAR.

Chapter 5

Conclusion

This dissertation work has developed critical microwave design technology for realization of small satellite SAR. A passive-array antenna with central high-power RF source was proposed as candidate for the antenna system. We have applied a novel multi-objective meta-heuristic optimization technique for optimal design of a passive travelling-wave slot array antenna panel. Large aperture efficiency for dual-polarization and a high beam-efficiency was achieved and demonstrated in a prototype unit. To realize a high-power RF source, we developed a resonant cavity power combiner with direct interface to SSPAs and a low-loss waveguide output. A prototype unit was fabricated and verified to yield low RF loss in a compact structure.

It is hoped that this work will contribute to the development of the proof-of-concept small-satellite SAR MicroXSAR by JAXA. In this chapter, we summarize the dissertation contents briefly; highlight key lessons learnt and contributions of this work to the research community. Finally future research problems are described, mainly arising from the limitations of the present work.

5.1 Summary and Discussion

We have gone through the entire design and development cycle of the problem in this dissertation. First, we studied the previous antenna systems of space-based SAR satellites (large satellites) and got an idea of the trade-offs involved in selection of

system architecture and technology. This literature study is especially important in context of space-technology development since technologies with prior space-heritage are preferred. Thus we also get information of past, current technologies under play in space environments and lessons learnt from their implementation. It is, however, difficult to make thorough comparison studies of these different cases since most of the time the goals and requirements of their respective space-missions are distinctive. Nevertheless, we get a fair understanding into the ideas of previous space-based SAR scientists and engineers, which has helped to shape the development process of the small-satellite SAR antenna system in this dissertation. One of the contributions of this work it is hoped would be to serve as a guide to future antenna-system developers not only for SAR, but also for other applications.

Active-phased array antenna systems are tempting since they offer high functionality like beam-steering and beam-formation. Beam-steering offers flexibility in changing the swath being imaged electronically by altering the excitation phase of antenna array elements. Beam-formation allows the formation of optimal beams, which are synthesized with some a-priori information of the area imaged. The optimal beams can reduce SAR ambiguities by placing nulls in antenna pattern at the direction of high-gain scatters. However, this added functionality comes at a cost of increasing the size, mass and cost of the system. A passive array system on another hand offers no beam-steering or beam-formation, but doesn't have the problems with size, weight and cost associated with active-array systems. One could, in principle, offer "beam-steering" capabilities to satellite equipped with passive array antennas by mechanically rotating the satellite body, although this would consume more satellite resources and is relatively inaccurate. The small-satellite bus technology development is rapidly progressing, and we can expect high satellite pointing, angular velocity accuracy, which would allow for accurate mechanical beam-steering.

Microwave frequencies are the preferred choice for satellite SAR against the lower frequencies, since the size of antenna can be reduced. Higher frequencies are attenuated by atmosphere and are unsuitable for Earth observation. However, the challenge with higher frequencies it is observed is to increase antenna aperture efficiency. Mi-

crostrip patch array antenna which has been popular at lower frequencies has high ohmic losses at microwave frequencies. The attenuation of the traveling-wave in the antenna array feeder has to be kept minimal, which is possible in slotted-waveguide array antennas, which use only vacuum (lossless-dielectric) medium for the traveling wave. TerraSAR-X and ERS-I are shown to be examples of slotted waveguide array antennas.

The challenge with slotted-waveguide array antennas have been to realize dual-polarization efficiently over an available physical area of antenna aperture. TerraSAR-X attempts to solve this problem by simply placing two slotted rectangular waveguides of H, V polarization slots (one polarization on a narrow-wall and other polarization of broad-wall of rectangular waveguide) alternatively. However, it is expected that there be strong mutual coupling effects (between the H-slots and V-slots) to be taken care of in such a dual-polarization configuration. In this dissertation, we have implemented a unique dual-polarization slotted antenna design, a parallel-plate antenna with orthogonal slot-pairs. This orthogonal slot-pair configuration allows for radiation of orthogonal circular polarizations, by simply changing the direction of feed of the traveling-wave inside the parallel-plate. Similar antenna has been used previously in the Venus Akatsuki space-mission, with only single polarization. The challenge in introducing dual-polarization is that it allows only for symmetric slot-pair geometry with uniform phase excitation. Such a constraint is necessary to realize identical circular-polarization beams.

The next step was to decide the appropriate slot-geometries for the antenna aperture. The slot-geometries effect the aperture illumination, which in turn effects the far-field antenna beam pattern. The effect of far-field antenna pattern on the quality of SAR image was also studied. Suitable metrics such as peak-gain, minimum main-lobe-gain, 1-dimensional beam-efficiency taking into account the range modulation effects are expressed in terms of antenna parameters. There has been previous work relating to synthesis of appropriate field-patterns for application in SAR, most of which are applicable in an unconstrained domain, i.e. the excitation profile of the antenna array is not constrained. Also these work assumes a parallel feed array

architecture, one in which each array-element is excited separately.

The parallel-plate slot-pair antenna on other hand falls under the class of traveling-wave antennas, where the power is fed in a serial fashion. A new antenna array mathematical model was proposed to model this traveling-wave array. The main strength of this model is that it expresses the antenna array excitation coefficients in terms of the slot-coupling coefficients which are turn are directly related to the physical length of the slot. High coupling indicated slot-lengths near to resonant length, while low coupling is achieved vice-versa. Traditional antenna pattern synthesis techniques were reviewed and are found unsuitable for this optimization problem. Meta-heuristic optimization techniques are found more suitable for the following main reasons:

1. They allow for definition of wide-range of objective functions, which may or may-not show discontinuities.
2. Low complexity of implementation.
3. They have shown success previously in a problem domain of antenna pattern synthesis, some cases of which were reviewed in this dissertation.

Among meta-heuristic algorithms, there are many options available, the most popular of which is genetic algorithm. We also discussed various ways in which multiple objectives may be optimized. The traditional multiple-objective optimization approach is to make a linear combination or define linear constraints of all the objectives and re-define a single objective function. The drawback of such a technique is that it is difficult to select the weighting factors without prior knowledge of the problem domain. Such a problem is not present in Pareto optimization approach where all the objectives are optimized simultaneously. The result is a Pareto-front which contains non-dominated solutions. NSGA-II is such a Pareto-optimization tool using genetic algorithm in its kernel. The use of this algorithm in the problem domain of antenna pattern synthesis is relatively new.

We made few simplifications to the antenna excitation synthesis problem and essentially divided the problem to design of 1-dimensional SAR range and cross-range

patterns. First, an entire single panel was designed using NSGA-II so it yields optimal SAR range pattern. The result of the algorithm was used to build and verify a realistic antenna panel model in electromagnetic simulation software. Later, a prototype model of the antenna panel was fabricated, and its electrical characteristics measured and compared with the simulation results. The antenna-panel exhibits predicted antenna pattern along with low cross-polarization at the main-lobe. Aperture efficiency of nearly 50% is achieved for both circular polarizations.. This is excellent when we compare with a naive approach of realizing dual-polarization on two physically separate apertures.

The measured center frequency (9.77 GHz) deviated from the design frequency (9.65 GHz) by 1%. This leads to about 2 deg beam-shift between the orthogonal circular polarizations beams at 9.65 GHz. Here we observe a drawback of using dual-feed traveling wave architecture for realizing dual polarization. For a given frequency the beam shifts in opposite directions depending on the direction of feed and length of feed. The bandwidth of such a type of antenna is thereby limited to narrowband.

The excitation of an array of antenna panels affects the cross-range pattern. Here again, we use NSGA-II to find optimal excitations of the antenna panels. Note that in this problem, we are not constrained by the dual-feed configuration. However traditional array optimization techniques are not applicable since the inter-element spacing of this array is $\gg \lambda_0$. We also introduced a new objective function which includes the range modulation effect, to minimize the azimuthal ambiguities.

The next challenge dealt was the realization of a high-power RF source which can act as a central transmitter. SSPA technology at X-band using GaN HEMT has been steadily growing and the output power capability of a single power amplifier unit has increased. To realize the peak power requirements of SAR satellite, it is necessary to coherently combine the output from a number of SSPAs. We reviewed the power combining architectures and examined their strengths and weakness. Additionally, reviewed were practically realized power combiners using different power combining architectures. For purpose of radar, the bandwidth requirement maybe lowered. Resonant cavity structures can thereby be implemented since they show

the least insertion loss and are compact as compared to tree combining architectures implemented in striplines.

To interface the SSPA output in microstrip lines directly to a cavity structure, a novel flaring and tapering structure of the microstrip line and substrate respectively is developed. Slits of length approximately $\lambda_{ms}/2$ are cut on the cavity walls through which the microstrip line is inserted. We can match the impedances of the microstrip line from SSPA and the cavity by varying the flaring, tapering and slot lengths. The cavity is further directly interfaced to an output WR90 rectangular waveguide. By reducing the number of mode conversions (TEM to TM₀₁₀ to TE₁₀) and by having only a single combining stage, we are able to minimize the insertion loss of the overall structure. The proposed cavity power combiner structure was fabricated, and the measured insertion loss is <0.77 dB over bandwidth of 245 MHz at center frequency of 9588 MHz against the design center frequency of 9650 MHz.

Here we can make an interesting observation regarding narrow-band systems. The measured center-frequency deviates by <1% from the design frequency. This is because errors during manufacturing and assembly result in the actual power combiner from having values of the parameters (such as cavity radius, cavity height,.... etc) different from the design value. This small error however, is still not acceptable since the system is narrow-band and the bandwidth of the system may entirely fall outside frequency band of interest. One obvious way to prevent this from happening is to use manufacturing and assembly process with lower error tolerences. However this has to happen at a high-cost. Another way is to have a tuning element in the system (such as making the cavity height variable) which can bring back the center-frequency to the desired value. The achieved bandwidth maybe be lower than the designed bandwidth since the values of other parameters (cavity radius, substrate ,etc.) may be slightly different from the optimum design parameters. Thus the design philosophy in case of narrow-band systems should be to design the system beforehand over a larger bandwidth than requirement and to have a tuning parameter which can change the center-frequency.

Another interesting observation is to compare the reflection s-parameter of an

input port to the active S parameter of the same port. The passive reflection s-parameter of port k is found by exciting only port k, and terminating all other ports by matched impedances. The active-S parameter on other hand is found by exciting all input ports.

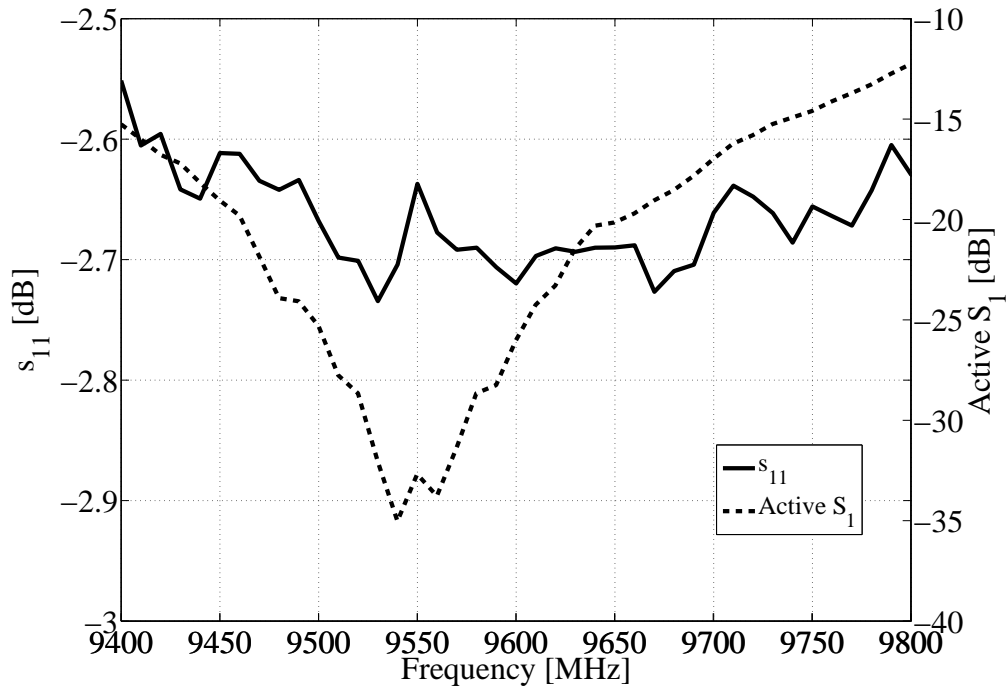


Figure 5-1: Reflection s_{11} versus active S_1 for the prototype power combiner.

Fig.5-1 shows the reflection s-parameter of port 1 is very poor. However, in case of activation of all input-ports the return power level at port decreases. This is because the fields coupled from the rest of input ports (ports 2,3,4,5 and 6) interferes destructively with the s_{11} field. Therefore, we also see that upon failure of one of the power amplifiers (Fig.4-21) not only does the insertion loss degrade, but also the active-S parameters of the operational input ports also degrade. There is also the loss due to return power to the failed amplifier port.

Such a behavior is unlike the case of power combiners using isolation resistors in their architecture (example: tree-type combing structure using Wilkinson 2-way dividers). The reflection and isolation s-parameters of such type of combiners is low.

Upon the degradation of one of more power-amplifiers, insertion loss degrades because of loss of power dissipated in isolation resistors. In case of resonant cavity combiners, the loss of power is due to increased return power to the input ports.

5.2 Suggestions for Future Work

Low-loss Power Distribution Network

This dissertation dealt with aspects of antenna panel and RF power source development related to the antenna system of small-satellite SAR. In Chapter.3.6 optimal excitation coefficients of antenna panels was found. The actual technology behind distributing power from the central RF power source to the antenna panels is not discussed.

In case of passive antenna array systems, it is necessary to have this power distribution network low-loss over the required bandwidth. Waveguide feeder networks are low-loss and are hence preferred. Lessons learned from the case of ERS-1 C-band SAR satellite which also uses a rectangular waveguide feeder network may be applied here. Another challenge is to ensure equal feed lengths (at least the electrical length at center frequency) to each panel/ sub-panel so that excitation phase is same over all the panels/ sub-panels for a given frequency. The power-dividing structures employed in the power-distribution network have to be engineered to appropriate power-dividing ratios and phase-shifts at the divider outputs.

Wide-band Dual-Polarization Antenna

A major limitation of using the dual-feed configuration in slotted waveguide antennas to achieve dual-polarization, is the beam-shift produced between the main-lobe of the two orthogonal polarization when the operating frequency is away from the center frequency. This limits the total chirp bandwidth and hence achievable ground resolution of the SAR system.

To further increase the bandwidth capability one technique is to reduce the length

of waveguide feeder as shown in Fig.5-2 by introducing center-feed configuration. We thus split each panel into two sub-panels. This, however, comes at cost of increasing the number of power-dividing structures and waveguide-feeder in the main power distribution network.

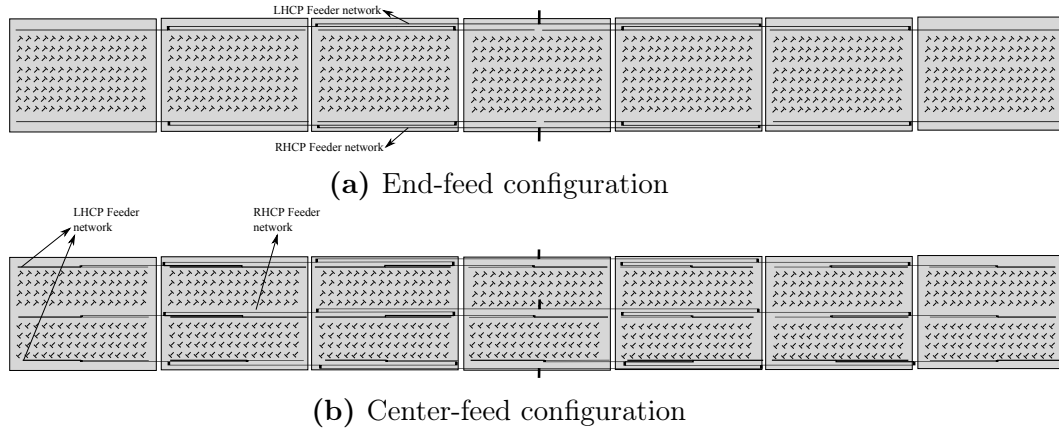


Figure 5-2: Feeder network configurations. By introducing more stages in the power distribution network the length of waveguide feeder for each sub-panel is reduced. However, the hardware structures and complexity increases.

Bibliography

- [1] D. Butler, “Many eyes on Earth,” *Nature*, vol. 505, no. 7482, pp. 143–144, jan 2014. [Online]. Available: <http://dx.doi.org/10.1038/505143a>
- [2] T. Wanwiwake and C. Underwood, “A Bi/Multi-Static microsatellite SAR constellation,” in *Small Satellites for Earth Observation*, H. P. Röser, R. Sandau, and A. Valenzuela, Eds. Wiss.-und-Technik-Verlag, 1996.
- [3] R. Sandau, “Status and trends of small satellite missions for Earth observation,” *Acta Astronautica*, vol. 66, no. 1, pp. 1–12, 2010.
- [4] “GRUS,” <https://en.axelspace.com/solution/grus/>, accessed: 2015-12-22.
- [5] “PLANET LABS,” <https://www.planet.com/>, accessed: 2015-12-22.
- [6] “Skybox Imaging,” www.skyboximaging.com, accessed: 2015-12-22.
- [7] J. Van Zyl and Y. Kim, *Synthetic aperture radar polarimetry*. John Wiley & Sons, 2011, vol. 2.
- [8] “TerraSAR-X - Germany’s radar eye in space,” http://www.dlr.de/eo/en/desktopdefault.aspx/tabid-5725/9296_read-15979/, accessed: 2015-11-24.
- [9] K. Ouchi, “Recent trend and advance of synthetic aperture radar with selected topics,” *Remote Sensing*, vol. 5, no. 2, p. 716, 2013. [Online]. Available: <http://www.mdpi.com/2072-4292/5/2/716>
- [10] “World’s first commercial 1 meter radar satellite,” http://www.pasco.co.jp/global/english/solutions/measuring_technologies/index_2.html, accessed: 2015-12-22.
- [11] H. Saito, A. Tomiki, P. R. Akbar, T. Ohtani, K. Nishijo, J. Hirokawa, and M. Ando, “Synthetic aperture radar compatible with 100kg class piggy-back satellite,” in *2013 Asia-Pacific Conference on Synthetic Aperture Radar (AP-SAR)*. IEEE, 2013, pp. 88–91.
- [12] H. Saito, “Compact X band synthetic aperture radar on 100kg small satellite,” in *IAA Symposium on Small Satellites for Earth Observation*, April 2015.

- [13] P. R. Akbar, J. T. S. Sumantyo, and H. Saito, "Study of synthetic aperture radar sensor onboard small satellite," *Technical report of IEICE. SANE*, vol. 112, no. 330, pp. 31–36, nov 2012. [Online]. Available: <http://ci.nii.ac.jp/naid/110009641712/en/>
- [14] R. Sullivan, "Synthetic aperture radar," in *Radar Handbook*, 3rd ed., M. I. Skolnik, Ed. McGraw-Hill, 2008, ch. 17.
- [15] A. Freeman, W. Johnson, B. Huneycutt, R. Jordan, S. Hensley, P. Siqueira, and J. Curlander, "The "myth" of the minimum sar antenna area constraint," *IEEE Transactions on Geoscience and Remote Sensing*, vol. 38, no. 1, pp. 320–324, 2000.
- [16] A. Doerry, "Performance limits for synthetic aperture radar-second edition," Sandia National Laboratories, Sandia National Laboratories, Albuquerque ,NM, Tech. Rep. SAND2006-0821, feb 2006.
- [17] K. Tomiyasu, "Tutorial review of synthetic-aperture radar (SAR) with applications to imaging of the ocean surface," *Proceedings of the IEEE*, vol. 66, no. 5, pp. 563–583, 1978. [Online]. Available: <http://dx.doi.org/10.1109/PROC.1978.10961>
- [18] J. C. Curlander and R. N. McDonough, *Synthetic Aperture Radar Systmes and Signal Processing*. Wiley Interscience, 1991.
- [19] D. Bickel, B. Brock, and C. Allen, *Spaceborne SAR Study: LDRD 92 Final Report*. Sandia National Laboratories, 1993.
- [20] J. R. James, P. S. Hall, and C. Wood, *Microstrip antenna : Theory and Design*. Peregrinus on behalf of the Institution of Electrical Engineers London ; New York, 1981.
- [21] Y. Kim and R. L. Jordan, "Spaceborne SAR antennas for Earth science," *Spaceborne Antennas for Planetary Exploration*, pp. 305–340, 2006.
- [22] R. Jordan, "The Seasat-A synthetic aperture radar system," *IEEE Journal of Oceanic Engineering*, vol. 5, no. 2, pp. 154–164, apr 1980. [Online]. Available: <http://dx.doi.org/10.1109/JOE.1980.1145451>
- [23] L. J. Cantafio, "Space-based radar systems and technology," in *Radar Handbook*, 2nd ed., M. Skolnik, Ed. New York: McGraw-Hill, 1990, ch. 22.
- [24] W. Johnson, "Magellan imaging radar mission to Venus," *Proceedings of the IEEE*, vol. 79, no. 6, pp. 777–790, jun 1991. [Online]. Available: <http://dx.doi.org/10.1109/5.90157>
- [25] "The Magellan spacecraft," <http://www2.jpl.nasa.gov/magellan/guide4.html>, accessed: 2015-10-4.

- [26] “The Radar system,” <http://www2.jpl.nasa.gov/magellan/guide5.html>, accessed: 2015-10-4.
- [27] “ERS-1: Four years of operational experience,” <http://www.esa.int/esapub/bulletin/bullet83/mckay83.htm>, accessed: 2015-10-4.
- [28] E. Attema, “The active microwave instrument on-board the ERS-1 satellite,” *Proceedings of the IEEE*, vol. 79, no. 6, pp. 791–799, jun 1991. [Online]. Available: <http://dx.doi.org/10.1109/5.90158>
- [29] R. Petersson, E. Kallas, and K. van't Klooster, “Radiation performance of the ERS-1 SAR EM antenna,” in *1988 IEEE AP-S. International Symposium, Antennas and Propagation*, 1988. [Online]. Available: <http://dx.doi.org/10.1109/APS.1988.94030>
- [30] “Radar travelling wavetube amplifier (TWTA),” <http://www.space-airbusds.com/en/equipment/radar-travelling-wavetube-amplifier-twta-jwv.html>, accessed: 2015-10-4.
- [31] “RADARSAT-1,” <http://www.asc-csa.gc.ca/eng/satellites/radarsat1/>, accessed: 2015-10-4.
- [32] R. Raney, A. Luscombe, E. Langham, and S. Ahmed, “RADARSAT (SAR imaging),” *Proceedings of the IEEE*, vol. 79, no. 6, pp. 839–849, jun 1991. [Online]. Available: <http://dx.doi.org/10.1109/5.90162>
- [33] J. Way and E. Smith, “The evolution of synthetic aperture radar systems and their progression to the EOS SAR,” *IEEE Geoscience and Remote Sensing Letters*, vol. 29, no. 6, pp. 962–985, 1991. [Online]. Available: <http://dx.doi.org/10.1109/36.101374>
- [34] M. Stangl, R. Werninghaus, and R. Zahn, “The TerraSAR-X active phased array antenna,” in *IEEE International Symposium on Phased Array Systems and Technology, 2003.*, 2003. [Online]. Available: <http://dx.doi.org/10.1109/PAST.2003.1256959>
- [35] B. Grafmuller, A. Herschlein, and C. Fischer, “The TerraSAR-X antenna system,” in *IEEE International Radar Conference, 2005.*, 2005. [Online]. Available: <http://dx.doi.org/10.1109/RADAR.2005.1435823>
- [36] S. Riendeau and C. Grenier, “RADARSAT-2 antenna,” in *Aerospace Conference, 2007 IEEE*. IEEE, 2007, pp. 1–9.
- [37] C. Livingstone, I. Sikaneta, C. Gierull, S. Chiu, and P. Beaulne, “RADARSAT-2 system and mode description,” DTIC Document, Tech. Rep., 2006.
- [38] “RADARSAT-2,” <https://directory.eoportal.org/web/eoportal/satellite-missions/r/radarsat-2>, accessed: 2015-09-17.

- [39] U. Naftaly and R. Levy-Nathansohn, "Overview of the TECSAR satellite hardware and mosaic mode," *IEEE Geoscience and Remote Sensing Letters*, vol. 5, no. 3, pp. 423–426, 2008.
- [40] "TecSAR (SAR technology demonstration satellite)," <https://directory.eoportal.org/web/eoportal/satellite-missions/t/tecsar>, accessed: 2015-09-17.
- [41] "Cosmo-skymed (constellation of 4 sar satellites)," <https://directory.eoportal.org/web/eoportal/satellite-missions/c-missions/cosmo-skymed>, accessed: 2015-10-6.
- [42] P. Capece, L. Borgarelli, M. D. Lazzaro, U. D. Marcantonio, and A. Torre, "COSMO SkyMed active phased array SAR instrument," in *2008 IEEE Radar Conference*. IEEE, may 2008. [Online]. Available: <http://dx.doi.org/10.1109/RADAR.2008.4720773>
- [43] R. Arora, C. Rao, B. Bakori, R. Neelakantan, and J. Vachchani, "Synthetic aperture radar payload on-board RISAT-1: configuration, technology and performance," *Current Science*, vol. 104, no. 4, p. 446, 2013.
- [44] C. A. Balanis, *Antenna Theory*, 3rd ed. Hoboken, NJ: Wiley Interscience, 2005.
- [45] Y. Kankaku, Y. Osawa, S. Suzuki, and T. Watanabe, "The overview of the l-band sar onboard alos-2," in *Proceedings of Progress in Electromagnetics Research Symposium*, 2009.
- [46] D. Parker and D. Zimmermann, "Phased arrays - part 1: theory and architectures," *IEEE Transactions on Microwave Theory and Techniques*, vol. 50, no. 3, pp. 678–687, mar 2002. [Online]. Available: <http://dx.doi.org/10.1109/22.989953>
- [47] D. Ehyaie, "Novel approaches to the design of phased array antennas," Ph.D. dissertation, The University of Michigan, 2011.
- [48] I. Chiba, "Digital beamforming (DBF) antenna system for mobile communications," in *Proceedings of International Symposium on Phased Array Systems and Technology*, 1996. [Online]. Available: <http://dx.doi.org/10.1109/PAST.1996.566093>
- [49] "White paper: Passive phased arrays for radar antennas," EMS Technologies, Inc., Norcross, Georgia, Tech. Rep., December 2005. [Online]. Available: http://dandsmicrowave.com/papers/Brunasso_Passive%20Phased%20Arrays%20for%20Radar%20Antennas.pdf
- [50] P. Capece and A. Torre, "SAR antennas," in *Space antenna handbook*, W. A. Imbriale, S. Gao, and L. Boccia, Eds. Wiley Online Library, 2012, ch. 13.

- [51] P. R. Akbar, H. Saito, M. Zhang, J. Hirokawa, and M. Ando, "Parallel-plate slot array antenna for deployable sar antenna onboard small satellite," *IEEE Transactions on Antennas and Propagation*, vol. 64, no. 5, pp. 1661–1671, May 2016.
- [52] J. Hirokawa, M. Ando, and N. Goto, "Waveguide-fed parallel plate slot array antenna," *IEEE Transactions on Antennas and Propagation*, no. 2, pp. 218–223, 1992. [Online]. Available: <http://dx.doi.org/10.1109/8.127406>
- [53] "Venus climate orbiter AKATSUKI," http://global.jaxa.jp/countdown/f17/pdf/presskit_akatsuki_e.pdf, accessed: 2015-10-6.
- [54] H. Ueda, J. Hirokawa, M. Ando, O. Amano, and Y. Kamata, "Space-use radial line slot antenna in 8GHz band with honeycomb structure," in *2008 IEEE Antennas and Propagation Society International Symposium*, jul 2008. [Online]. Available: <http://dx.doi.org/10.1109/APS.2008.4619914>
- [55] P. Akbar, M. Zhang, J. Hirokawa, H. Saito, and M. Ando, "X-band parallel-plate slot array antenna for SAR sensor onboard 100 kg small satellite," in *Proc. of IEEE International Symposium on Antennas and Propagation and North American Radio Science Meeting*, Vancouver, BC, Canada, 2015.
- [56] "SAH aramid fiber/ phenolic resin honeycomb datasheet," http://showaircraftusa.com/theme/showa_001_blue/doc/SAH-Technical-Data-Rev1.pdf, Showa Aircraft Industry Co., Ltd., Nov. 2012, accessed: 2015-09-1.
- [57] "Fm73 epoxy film adhesive datasheet," http://cytec.com/sites/default/files/datasheets/FM_73_081111.pdf, Cytec, Aug. 2011, accessed: 2015-09-1.
- [58] M. Samardzija, T. Kai, J. Hirokawa, and M. Ando, "Single-layer waveguide feed for uniform plane TEM-wave in oversized-rectangular waveguide with hard-surface sidewalls," *IEEE Transactions on Antennas and Propagation*, vol. 54, no. 10, pp. 2813–2819, oct 2006. [Online]. Available: <http://dx.doi.org/10.1109/TAP.2006.882166>
- [59] J. Linjiao, "Range ambiguity distribution characteristic of spaceborne sar and its design consideration," *Journal of Electronics (China)*, vol. 12, no. 2, pp. 160–167, 1995. [Online]. Available: <http://dx.doi.org/10.1007/BF02778440>
- [60] H. Griffiths and P. Mancini, "Ambiguity suppression in sars using adaptive array techniques," in *[Proceedings] IGARSS'91 Remote Sensing: Global Monitoring for Earth Management*, 1991. [Online]. Available: <http://dx.doi.org/10.1109/IGARSS.1991.580292>
- [61] S. Y. Kim, N. H. Myung, and M. J. Kang, "Antenna mask design for SAR performance optimization," *IEEE Geoscience and Remote Sensing Letters*, vol. 6, no. 3, pp. 443–447, jul 2009. [Online]. Available: <http://dx.doi.org/10.1109/LGRS.2009.2016356>

- [62] A. A. Oliner and D. R. Jackson, "Leaky-wave antennas," in *Antenna Engineering Handbook*, 4th ed., J. L. Volakis, Ed. New York: McGraw-Hill, 2007, ch. 11.
- [63] R. A. Gilbert, "Waveguide slot antenna arrays," in *Antenna Engineering Handbook*, 4th ed., J. L. Volakis, Ed. New York: McGraw-Hill, 2007, ch. 9.
- [64] K. Sakakibara, Y. Kimura, J. Hirokawa, M. Ando, and N. Goto, "A two-beam slotted leaky waveguide array for mobile reception of dual-polarization DBS," *IEEE Transactions on Vehicular Technology*, vol. 48, no. 1, pp. 1–7, 1999. [Online]. Available: <http://dx.doi.org/10.1109/25.740055>
- [65] W. H. Kummer, "Feeding and phase scanning," in *Array Systems*, 2nd ed., ser. Microwave Scanning Antennas, R. C. Hansen, Ed. New York and London: Academic Press, 1966, vol. 3, ch. 1.
- [66] H. J. Visser, *Array and Phased Array Antenna Basics*. Wiley-Blackwell, jul 2005. [Online]. Available: <http://dx.doi.org/10.1002/0470871199>
- [67] A. A. Oliner and R. G. Malech, "Radiating elements and mutual coupling," in *Array Theory and Practice*, 2nd ed., ser. Microwave Scanning Antennas, R. C. Hansen, Ed. New York and London: Academic Press, 1966, vol. 2, ch. 2.
- [68] M. Bachmann, M. Schwerdt, and B. Bräutigam, "Accurate antenna pattern modeling for phased array antennas in sar applications—demonstration on terrasar-x," *International Journal of Antennas and Propagation*, vol. 2009, 2009.
- [69] J.-M. Jin and D. J. Riley, *Finite element analysis of antennas and arrays*. Hoboken, N.J.: John Wiley & Sons, 2009.
- [70] N. Appannagarri, I. Bardi, R. Edlinger, J. Manges, M. Vogel, Z. Cendes, and J. Hadden, "Modeling phased array antennas in ansoft HFSS," in *Proceedings 2000 IEEE International Conference on Phased Array Systems and Technology (Cat. No.00TH8510)*, 2000. [Online]. Available: <http://dx.doi.org/10.1109/PAST.2000.858966>
- [71] S. A. Schelkunoff, "A mathematical theory of linear arrays," *Bell System Technical Journal*, vol. 22, no. 1, pp. 80–107, jan 1943. [Online]. Available: <http://dx.doi.org/10.1002/j.1538-7305.1943.tb01306.x>
- [72] D. Cheng and M. Ma, "A new mathematical approach for linear array analysis," *IRE Trans. Antennas Propag.*, vol. 8, no. 3, pp. 255–259, may 1960. [Online]. Available: <http://dx.doi.org/10.1109/TAP.1960.1144842>
- [73] D. Gaushell, "Synthesis of linear antenna arrays using z transforms," *IEEE Transactions on Antennas and Propagation*, vol. 19, no. 1, pp. 75–80, jan 1971. [Online]. Available: <http://dx.doi.org/10.1109/TAP.1971.1139864>

- [74] C. Dolph, “A current distribution for broadside arrays which optimizes the relationship between beam width and side-lobe level,” *Proceedings of the IRE*, vol. 34, no. 6, pp. 335–348, jun 1946. [Online]. Available: <http://dx.doi.org/10.1109/JRPROC.1946.225956>
- [75] H. Unz, “Linear arrays with arbitrarily distributed elements,” *IRE Trans. Antennas Propag.*, vol. 8, no. 2, pp. 222–223, mar 1960. [Online]. Available: <http://dx.doi.org/10.1109/TAP.1960.1144829>
- [76] W. Stutzman and S. Licul, “Synthesis methods for antennas,” in *Modern Antenna Handbook*, C. A. Balanis, Ed. Wiley-Blackwell, aug 2008, ch. 13. [Online]. Available: <http://dx.doi.org/10.1002/9780470294154>
- [77] R. L. Haupt, “Genetic algorithms for antennas,” in *Modern Antenna Handbook*, C. A. Balanis, Ed. Wiley-Blackwell, aug 2008, ch. 32. [Online]. Available: <http://dx.doi.org/10.1002/9780470294154>
- [78] L. Bianchi, M. Dorigo, L. M. Gambardella, and W. J. Gutjahr, “A survey on metaheuristics for stochastic combinatorial optimization,” *Natural Computing*, vol. 8, no. 2, pp. 239–287, sep 2008. [Online]. Available: <http://dx.doi.org/10.1007/s11047-008-9098-4>
- [79] D. E. Goldberg, *Genetic Algorithms in Search, Optimization and Machine Learning*, 1st ed. Boston, MA, USA: Addison-Wesley Longman Publishing Co., Inc., 1989.
- [80] J. Kennedy and R. Eberhart, “Particle swarm optimization,” 1995.
- [81] S. Kirkpatrick, C. D. Gelatt, and M. P. Vecchi, “Optimization by simulated annealing,” *Science*, vol. 220, no. 4598, pp. 671–680, 1983. [Online]. Available: <http://www.sciencemag.org/content/220/4598/671.abstract>
- [82] D. Jones, S. Mirrazavi, and M. Tamiz, “Multi-objective meta-heuristics: An overview of the current state-of-the-art,” *European Journal of Operational Research*, vol. 137, no. 1, pp. 1–9, feb 2002. [Online]. Available: [http://dx.doi.org/10.1016/S0377-2217\(01\)00123-0](http://dx.doi.org/10.1016/S0377-2217(01)00123-0)
- [83] R. Haupt, “Optimum quantised low sidelobe phase tapers for arrays,” *Electron. Lett.*, vol. 31, no. 14, p. 1117, 1995. [Online]. Available: <http://dx.doi.org/10.1049/el:19950786>
- [84] M. Khodier and C. Christodoulou, “Linear array geometry synthesis with minimum sidelobe level and null control using particle swarm optimization,” *IEEE Transactions on Antennas and Propagation*, vol. 53, no. 8, pp. 2674–2679, aug 2005. [Online]. Available: <http://dx.doi.org/10.1109/TAP.2005.851762>
- [85] D. Boeringer and D. Werner, “A comparison of particle swarm optimization and genetic algorithms for a phased array synthesis problem,” in *IEEE Antennas and*

- Propagation Society International Symposium. Digest. Held in conjunction with: USNC/CNC/URSI North American Radio Sci. Meeting (Cat. No.03CH37450)*, 2003. [Online]. Available: <http://dx.doi.org/10.1109/APS.2003.1217430>
- [86] V. Murino, A. Trucco, and C. S. Regazzoni, "Synthesis of unequally spaced arrays by simulated annealing," *IEEE Transactions on Signal Processing*, vol. 44, no. 1, pp. 119–122, 1996.
- [87] R. L. Haupt and D. H. Werner, *Genetic algorithms in electromagnetics*. John Wiley & Sons, 2007.
- [88] S.-H. Lim, J.-H. Han, S.-Y. Kim, and N.-H. Myung, "Azimuth beam pattern synthesis for airborne SAR system optimization," *Progress In Electromagnetics Research*, vol. 106, pp. 295–309, 2010. [Online]. Available: <http://dx.doi.org/10.2528/PIER10061901>
- [89] A. Konak, D. W. Coit, and A. E. Smith, "Multi-objective optimization using genetic algorithms: A tutorial," *Reliability Engineering & System Safety*, vol. 91, no. 9, pp. 992–1007, sep 2006. [Online]. Available: <http://dx.doi.org/10.1016/j.ress.2005.11.018>
- [90] N. Srinivas and K. Deb, "Multiobjective optimization using nondominated sorting in genetic algorithms," *Evolutionary Computation*, vol. 2, pp. 221–248, 1994.
- [91] K. Deb, A. Pratap, S. Agarwal, and T. Meyarivan, "A fast and elitist multiobjective genetic algorithm: NSGA-II," *IEEE Transactions on Evolutionary Computation*, vol. 6, no. 2, pp. 182–197, apr 2002. [Online]. Available: <http://dx.doi.org/10.1109/4235.996017>
- [92] *User's Guide - High Frequency Structure Simulator*, Ansoft HFSS, Pittsburgh, USA, Jun. 2005.
- [93] T. A. Weil and M. Skolnik, "The radar transmitter," in *Radar Handbook*, 3rd ed., M. I. Skolnik, Ed. McGraw-Hill, 2008, ch. 10.
- [94] W. Q. Lohmeyer, R. J. Aniceto, and K. L. Cahoy, "Communication satellite power amplifiers: current and future SSPA and TWTA technologies," *International Journal of Satellite Communications and Networking*, pp. n/a–n/a, mar 2015. [Online]. Available: <http://dx.doi.org/10.1002/sat.1098>
- [95] M. T. Borkowski, "Solid-state transmitters," in *Radar Handbook*, 3rd ed., M. I. Skolnik, Ed. McGraw-Hill, 2008, ch. 11.
- [96] N. V. Bijeev, A. Malhotra, V. Kumar, S. Singh, K. S. Dasgupta, R. N. Motta, B. Venugopal, Sandhyarani, O. K. Jinan, and B. K. Jayakumar, "Design and realization challenges of power supplies for space TWT," in *2011 IEEE International Vacuum Electronics Conference (IVEC)*, feb 2011. [Online]. Available: <http://dx.doi.org/10.1109/IVEC.2011.5747060>

- [97] J. M. Weekley and B. J. Mangus, "TWTA versus SSPA: A comparison of on-orbit reliability data," *IEEE Transactions on Electron Devices*, vol. 52, no. 5, pp. 650–652, 2005.
- [98] E. F. Nicol, B. J. Mangus, J. R. Grebliunas, K. Woolrich, and J. R. Schirmer, "TWTA versus SSPA: A comparison update of the Boeing satellite fleet on-orbit reliability," in *Vacuum Electronics Conference (IVEC), 2013 IEEE 14th International*. IEEE, 2013, pp. 1–2.
- [99] D. M. Pozar, *Microwave Engineering*, 4th ed. Wiley, 2011.
- [100] R. Ernst, R. Camisa, and A. Presser, "Graceful degradation properties of matched n-port power amplifier combiners," in *MTT-S International Microwave Symposium Digest*. Institute of Electrical & Electronics Engineers (IEEE), 1977. [Online]. Available: <http://dx.doi.org/10.1109/MWSYM.1977.1124396>
- [101] W. Read, "A proposed high-frequency, negative-resistance diode," *Bell System Technical Journal*, vol. 37, no. 2, pp. 401–446, 1958.
- [102] C. Mead, "Schottky barrier gate field effect transistor," *Proceedings of the IEEE*, vol. 54, no. 2, pp. 307–308, 1966.
- [103] T. Mimura, "The early history of the high electron mobility transistor (HEMT)," *IEEE Transactions on Microwave Theory and Techniques*, vol. 50, no. 3, pp. 780–782, 2002.
- [104] K. Chang and C. Sun, "Millimeter-wave power-combining techniques," *IEEE Transactions on Microwave Theory and Techniques*, vol. 31, pp. 91–107, 1983.
- [105] A. Afsahi and L. E. Larson, "Monolithic power-combining techniques for watt-level 2.4-ghz cmos power amplifiers for WLAN applications," *IEEE Transactions on Microwave Theory and Techniques*, vol. 61, no. 3, pp. 1247–1260, 2013.
- [106] M. Kim, J. J. Rosenberg, R. P. Smith, R. M. Weikle, J. B. Hacker, M. P. De Lizio, D. B. Rutledge *et al.*, "A grid amplifier," *IEEE Microwave and Guided Wave Letters*, vol. 1, no. 11, pp. 322–324, 1991.
- [107] K. J. Russell, "Microwave power combining techniques," *IEEE Transactions on Microwave Theory and Techniques*, vol. 27, no. 5, pp. 472–478, 1979.
- [108] K. Kurokawa and F. Magalhaes, "An X-band 10-watt multiple-IMPATT oscillator," *Proceedings of the IEEE*, vol. 59, no. 1, pp. 102–103, 1971. [Online]. Available: <http://dx.doi.org/10.1109/PROC.1971.8109>
- [109] E. Wilkinson, "An n-way hybrid power divider," *IEEE Transactions on Microwave Theory and Techniques*, vol. 8, no. 1, pp. 116–118, jan 1960. [Online]. Available: <http://dx.doi.org/10.1109/TMTT.1960.1124668>

- [110] J. Schellenberg and M. Cohn, "A wideband radial power combiner for FET amplifiers," in *1978 IEEE International Solid-State Circuits Conference. Digest of Technical Papers*, 1978. [Online]. Available: <http://dx.doi.org/10.1109/ISSCC.1978.1155840>
- [111] J. Schellenberg, "The evolution of power combining techniques: From the 60s to today," in *2015 IEEE MTT-S International Microwave Symposium*, may 2015. [Online]. Available: <http://dx.doi.org/10.1109/MWSYM.2015.7166749>
- [112] N.-S. Cheng, P. Jia, D. B. Rensch, R. York *et al.*, "A 120-W X-band spatially combined solid-state amplifier," *IEEE Transactions on Microwave Theory and Techniques*, vol. 47, no. 12, pp. 2557–2561, 1999.
- [113] H. Matsumura and H. Mizuno, "Design of microwave power combiner with circular TM_{0m0} mode cavity," *Electron. Comm. Jpn. Pt. II*, vol. 70, no. 9, pp. 1–11, 1987. [Online]. Available: <http://dx.doi.org/10.1002/ecjb.4420700901>
- [114] —, "Design of microwave combiner with waveguide ports," *Electron. Comm. Jpn. Pt. II*, vol. 71, no. 8, pp. 53–61, 1988. [Online]. Available: <http://dx.doi.org/10.1002/ecjb.4420710806>
- [115] M. Knox, R. Youmans, M. Kumar, L. Forker, H. Voigt, P. Brand, F. Marcotte, and A. Hughes, "400 W X-band GaAs MMIC CW amplifier," in *Proceedings of 1995 IEEE MTT-S International Microwave Symposium*, 1995. [Online]. Available: <http://dx.doi.org/10.1109/MWSYM.1995.406283>
- [116] K. Kanto, A. Satomi, Y. Asahi, Y. Kashiwabara, K. Matsushita, and K. Takagi, "An X-band 250w solid-state power amplifier using GaN power HEMTs," in *2008 IEEE Radio and Wireless Symposium*, jan 2008. [Online]. Available: <http://dx.doi.org/10.1109/RWS.2008.4463432>
- [117] M. Ghanadi, "A new compact broadband radial power combiner," Ph.D. dissertation, Technical University of Berlin, 2011.
- [118] N. Okubo, Y. Kaneko, T. Saito, and Y. Tokumitsu, "A 6-GHz 80-w GaAs FET amplifier with TM-mode cavity power combiner," in *MTT-S International Microwave Symposium Digest*, 1983. [Online]. Available: <http://dx.doi.org/10.1109/MWSYM.1983.1130883>
- [119] J. Coonrod, "Thermal design begins at the circuit board," <http://mwrf.com/materials/thermal-design-begins-circuit-board>, May 2011, accessed: 2015-10-22.
- [120] "Rt/duroid 6035htc high frequency laminate," Rogers Corporation, Chandler, Arizona, Tech. Rep. [Online]. Available: <https://www.rogerscorp.com/documents/1946/acm/RT-duroid-6035HTC-High-Frequency-Laminates.aspx>
- [121] T. K. Ishii, *Microwave engineering*. The Ronald Press Company, 1966.

List of related publications

- Ravindra, V., Saito, H., Hirokawa, J., " Optimal power coupling coefficient distribution determination for dual feed leaky waveguide array using multi objective genetic algorithm," 8th European Conference on Antennas and Propagation (EuCAP), pp.1507,1511, 6-11 April 2014.
- Ravindra, V., Saito, H., Hirokawa, J., Zhang, M.," Cylindrical cavity microwave power combiner with microstrip line inputs and rectangular waveguide output," International Microwave Symposium, IEEE MTT-S, 17-22 May 2015.
- Ravindra, V., Akbar, P., Saito, H., J., Zhang M. and Hirokawa, J.," A Parallel Plate Slot-Pair Array Dual Polarization Antenna for Small Satellite SAR"," International Symposium on Antennas and Propagation, IEEE, 9-12 Nov 2015.
- Ravindra, V., Saito, H., Akbar, P, J., Zhang M. and Hirokawa, J.," Optimal Cross Range Pattern Synthesis Using Multi-Objective Genetic Algorithm for a Passive Antenna in Small Satellite SAR"," International Symposium on Antennas and Propagation (ISAP), IEEE, 9-12 Nov 2015.
- Saito, H., Akbar, P., Ravindra, V., Watanabe, H., Tomiki, A., Hirokawa, J., Zhang, M. and Shirasaka, S.," Compact X-band Synthetic Aperture Radar with Deployable Plane Antenna-Project of a 100kg-Class SAR Satellite," 4S Symposium, 30 May-3 Jun 2016.
- Ravindra, V., Akbar, P., Zhang, M., Hirokawa, J., Saito, H., Oyama, A., "A Dual Polarization X-band Traveling-Wave Antenna Panel for Small Satellite Synthetic Aperture Radar," in IEEE Transactions on Antennas and Propagation, in press.